



저작자표시-비영리-변경금지 2.0 대한민국

이용자는 아래의 조건을 따르는 경우에 한하여 자유롭게

- 이 저작물을 복제, 배포, 전송, 전시, 공연 및 방송할 수 있습니다.

다음과 같은 조건을 따라야 합니다:



저작자표시. 귀하는 원저작자를 표시하여야 합니다.



비영리. 귀하는 이 저작물을 영리 목적으로 이용할 수 없습니다.



변경금지. 귀하는 이 저작물을 개작, 변형 또는 가공할 수 없습니다.

- 귀하는, 이 저작물의 재이용이나 배포의 경우, 이 저작물에 적용된 이용허락조건을 명확하게 나타내어야 합니다.
- 저작권자로부터 별도의 허가를 받으면 이러한 조건들은 적용되지 않습니다.

저작권법에 따른 이용자의 권리는 위의 내용에 의하여 영향을 받지 않습니다.

이것은 [이용허락규약\(Legal Code\)](#)을 이해하기 쉽게 요약한 것입니다.

[Disclaimer](#)

공학박사 학위논문

근적외선 레이저 후면 식각공정에서  
인산을 활용한 유리 미세구조물 가공

Glass microstructuring with near-infrared laser  
induced backside wet etching using phosphoric acid

2021 년 2 월

서울대학교 대학원

기계항공공학부

권 귀 감

**GLASS MICROSTRUCTURING WITH  
NEAR-INFRARED LASER INDUCED  
BACKSIDE WET ETCHING USING  
PHOSPHORIC ACID**

**DISSERTATION**

**SUBMITTED TO THE SCHOOL OF MECHANICAL AND  
AEROSPACE ENGINEERING AND THE COMMITTEE ON  
GRADUATE STUDIES OF SEOUL NATIONAL UNIVERSITY  
IN PARTIAL FULFILLMENT OF THE REQUIREMENTS  
FOR THE DEGREE OF DOCTOR OF PHILOSOPHY**

**Kui-kam Kwon**

**February 2021**

# 근적외선 레이저 후면 식각공정에서 인산을 활용한 유리 미세구조물 가공

Glass microstructuring with near-infrared laser  
induced backside wet etching using phosphoric acid

지도교수 안 성 훈

이 논문을 공학박사 학위논문으로 제출함

2020 년 10 월






서울대학교 대학원

기계항공공학부

권 귀 감

권귀감의 공학박사 학위논문을 인준함

2020 년 12 월

위원장 :	차 석 원	(서명)	
부위원장 :	안 성 훈	(서명)	
위원 :	조 규 진	(서명)	
위원 :	이 윤 석	(서명)	
위원 :	송 기 영	(서명)	



*In memories of the late Prof. Chong Nam Chu*

# Abstract

Kui-Kam Kwon

School of Mechanical and Aerospace Engineering

The Graduate School

Seoul National University

This dissertation examined the laser-induced backside wet etching process that used a phosphoric acid-added absorbent. Glass materials have high strength, corrosion resistance, non-conductivity, and bio compatibility properties that are difficult to find in other transparent materials; however, these material properties make glass a hard-to-cut material in terms of processing.

Various attempts have been made to increase the utilization of glass through industrial-friendly processing techniques such as mechanical cutting—conventional processing method—chemical etching, and carbon dioxide laser micromachining. Nevertheless, industry-friendly techniques still have target shape limitations due to process characteristics and glass's

material properties. To solve these problems, various processes, such as femtosecond pulse laser machining, electrochemical discharge machining, and deep reactive ion etching, have been widely studied and applied. Such processes can be used to manufacture various glass microstructure geometries. Research into glass processing has studied various techniques, but only a few studies have examined industrial techniques for processing complex shapes.

In this dissertation, the processable geometry of glass produced through an industry-friendly process was extended using a LIBWE process and a near-infrared laser. Previous studies of laser-induced backside wet etching using near-infrared lasers found that fracturing occurred due to excessive heat absorption. This crack generation could be suppressed by the passive layer created by the reaction between phosphoric acid and glass. By suppressing the breakage of the glass, it was possible to process high-aspect-ratio glass microstructures with no tapering. Also, a scan path optimization method for laser-induced backside wet etching was developed to process not only one-dimensional channel shapes, but also a variety of glass microstructures that were difficult to manufacture using conventional laser-induced backside wet etching and industrial-friendly techniques. Based on this crack suppression and scan path optimization method, glass microstructures for various glass applications, such as microfluidic devices, UV-imprint molds, and glass

components, were machined to validate the proposed techniques for actual glass applications.

**Keyword:** Laser-induced backside wet etching; Glass micromachining; Laser beam machining; Laser scan path optimization

# Contents

<b>Abstract</b> .....	i
<b>Contents</b> .....	iv
<b>List of Figures</b> .....	vii
<b>List of Tables</b> .....	xv
<b>Chapter 1 Introduction</b> .....	- 1 -
<b>1.1. Research Background</b> .....	- 1 -
<b>1.2. Research Objective</b> .....	- 9 -
<b>1.3. Dissertation Overview</b> .....	- 10 -
<b>Chapter 2 The LIBWE process</b> .....	- 13 -
<b>2.1. LIBWE</b> .....	- 13 -
<b>2.2. Reactions between Glass and Phosphoric acid</b> .....	- 18 -
<b>2.3. Interaction between a Laser Beam and Liquid Absorbent</b> ..	- 21 -
<b>2.4. Experimental Procedure</b> .....	- 25 -

<b>Chapter 3 LIBWE using Phosphoric Acid-Added Absorbent.....</b>	<b>- 32 -</b>
<b>3.1. Crack Generation in Near-Infrared LIBWE Process.....</b>	<b>- 33 -</b>
<b>3.2. Phosphate Protective Layer Generation .....</b>	<b>- 40 -</b>
<b>Chapter 4 Machining Characteristics of LIBWE using a Phosphoric Acid-Added Absorbent.....</b>	<b>- 52 -</b>
<b>4.1. Effect of Phosphoric Acid Concentration .....</b>	<b>- 53 -</b>
<b>4.1.1. Maximum aspect ratio .....</b>	<b>- 53 -</b>
<b>4.1.2. Sidewall roughness .....</b>	<b>- 59 -</b>
<b>4.1.3. Fabrication speed .....</b>	<b>- 62 -</b>
<b>4.2. Effect of Parameters except Phosphoric Acid Concentration-</b>	<b>64 -</b>
<b>4.2.1. Fabrication speed .....</b>	<b>- 64 -</b>
<b>4.2.2. Machinability .....</b>	<b>- 67 -</b>
<b>4.2.3. Depth of a channel.....</b>	<b>- 69 -</b>
<b>4.2.4. Various shapes of microchannels .....</b>	<b>- 72 -</b>
<b>Chapter 5 Fabrication of 3D Microstructures .....</b>	<b>- 74 -</b>

<b>5.1. Conventional Scan Paths</b> .....	- 75 -
<b>5.2. Randomly Distributed Scan Path</b> .....	- 84 -
<b>5.2.1. Random-point scan path</b> .....	- 86 -
<b>5.2.2. Random-line scan path</b> .....	- 93 -
<b>5.3. Effects of Random-Line Scan Path Generation Parameters</b> -	107 -
<b>5.3.1. Number of sample points</b> .....	- 111 -
<b>5.3.2. Minimum length of a scan line</b> .....	- 116 -
<b>5.3.3. Scoring filter width</b> .....	- 118 -
<b>5.4. Degree of Precision in Complicated Structure Fabrication</b> -	119 -
<b>Chapter 6 Feasible Applications</b> .....	- 122 -
<b>Chapter 7 Conclusion</b> .....	- 129 -
<b>Reference</b> .....	- 133 -
<b>국문 초록</b> .....	- 138 -

# List of Figures

- Figure 1.1 Glass material processing techniques classified as ease of technique and versatility of processable geometry.
- Figure 1.2 Crack suppressed LIBWE process with phosphoric acid added absorbent.
- Figure 2.1 The LIBWE machining process with a copper sulfate absorbent.
- Figure 2.2 Equilibrium between copper (II) oxide and copper (I) oxide corresponding to the oxygen concentration and temperature.
- Figure 2.3 Equation for the chemical reaction between phosphoric acid and silicon dioxide: (a) dehydration of orthophosphoric acid and (b) reaction between pyrophosphoric acid and silicon dioxide.
- Figure 2.4 Diagram of the reaction between phosphoric acid and glass: (a) under 200 °C and (b) over 200 °C.
- Figure 2.5 (a) Laser power density profile of a single pulse and (b) laser irradiating area in milling process with single scan direction.
- Figure 2.6 (a) Schematic diagram of the LIBWE system. (b) picture of the experimental setup.
- Figure 2.7 Schematic diagram of the laser source and scanner control system with generated scan path data.



- Figure 3.1 Crack generation during the LIBWE process with copper sulfate solution absorbent.
- Figure 3.2 Diagrams and *in situ* observation of the LIBWE milling process in copper sulfate absorbent: (a) initial state, (b) bubble generation state, and (c) crack generation state.
- Figure 3.3 SEM image and elemental analysis of sidewall machined in copper sulfate absorbent: (a) initial state, (b) bubble generation state, and (c) crack generation state. Red dots are detected copper element.
- Figure 3.4 Diagram of heat accumulation positive feedback inside a bubble.
- Figure 3.5 Excessively deposited copper oxide on the machined channel. (a) channel overview (b) enlarged image of excessively deposited copper oxide.
- Figure 3.6 High aspect ratio channel fabricated in absorbent with added phosphoric acid (60 wt%). (a) overall cross-section of a channel (b) magnified view at the top (c) 320  $\mu\text{m}$  from top (d) 640  $\mu\text{m}$  from top.
- Figure 3.7 Diagrams and *in situ* observations of the LIBWE milling process in absorbent with added phosphoric acid: (a) initial state, (b) vapor layer generation state, and (c) crack generation state.
- Figure 3.8 SEM image and elemental analysis of a sidewall machined in absorbent with added phosphoric acid: (a) initial state, (b) vapor layer generation state, and (c) crack generation state. Red dots are detected copper element and green dots are

detected phosphorus element.

- Figure 3.9 Glass surface reactions during the LIBWE process: (a) in copper sulfate solution and (b) in solution with added phosphoric acid.
- Figure 3.10 XPS data of phosphorus and copper on machined surface in different absorbent.
- Figure 3.11 Vapor and absorbent states after the fabrication process was completed.
- Figure 3.12 Dimples machined with non-contact liquid absorbent. (a) machining diagram, (b) dimple machined with copper sulfate absorbent, (c) dimple machined with phosphoric acid added absorbent.
- Figure 4.1 Maximum fabricable depth according to changes in the following phosphoric acid concentration.
- Figure 4.2 Fabricated channel with different phosphoric acid concentrations: (a) maximum fabricable depth and (b) crack generation.
- Figure 4.3 Duration of vapor layer until crack generation due to phosphoric acid change from 0 wt% to 40 wt%.
- Figure 4.4 Maximum depth as the parameter changes: (a) copper sulfate concentration, (b) laser power, and (c) scan speed.
- Figure 4.5 Average surface roughness (Ra) changes according to the phosphoric acid concentration.
- Figure 4.6 Average surface roughness (Ra) changes according to the phosphoric acid concentration (a) the overall shape of the

sidewall, and (b) magnified images of the sidewalls.

- Figure 4.7 Fabrication speed according to phosphoric acid concentration change.
- Figure 4.8 Sidewall image and elemental distribution compared to the phosphoric acid concentration.
- Figure 4.9 Fabrication speed according to parameters change: (a) copper sulfate concentration, (b) laser power, and (c) laser scan speed.
- Figure 4.10 Absorbed energy density at a single point according to parameter changes. Absorbed energy density and processability are compared: (a) copper sulfate concentration, (b) laser power, and (c) laser scan speed.
- Figure 4.11 Schematic of laser beam and depth of focus.
- Figure 4.12 Machined channel depth compared to the number of scans in different phosphoric acid concentration (a) 0 wt%, (b) 10 wt%, (c) 20 wt%, (d) 30 wt%, (e) 40 wt%.
- Figure 4.13 Diagram and SEM images of channels with various shapes: (a) circular channel with increasing radius and (b) ladder-shaped multiple channels.
- Figure 5.1 Conventional scan paths for comparison: (a) raster, (b) reciprocating, (c) spiral, and (d) random.
- Figure 5.2 SEM images and profiles of machined glass micro pockets fabricated with (a) raster path (b) reciprocating path (c) spiral path (d) random path. Profiles of (a), (b), and (d) were results observed from micropockets machined every 500 seconds, and profiles of (c) were results observed every 250 seconds.

- Figure 5.3 Diagrams and in situ observations for the micropocket machining process with bubble accumulation: (a) diagrams and (b) in situ observations.
- Figure 5.4 Additional machining during the LIBWE process, due to the additional laser irradiation and heat accumulation inside a bubble.
- Figure 5.5 Number of scans distribution with random scan path.
- Figure 5.6 The idea of scan paths in this study. (a) conventional raster scan path, (b) random point scan path, and (c) random line scan path.
- Figure 5.7 Sequence of random-point scan path generation (a) target area setting, (b) point sequence setting, and (c) the sequence of points mixing.
- Figure 5.8 Square pocket fabricated with a random-point scan path: (a) SEM image and (b) 3D surface profile data.
- Figure 5.9 SEM image of pockets fabricated with a random-point scan path: (a) square pocket, (b) cross-shaped pocket, (c) triangular pocket, and (d) circular pillar.
- Figure 5.10 Random-point scan path generation for pyramid structure.
- Figure 5.11 Glass pyramid structure fabricated with a random-point scan path: (a) SEM image and 3D surface profile of a pyramid fabricated with 20 W laser power and ten layer scans and (b) twenty layer scans; (c) a pyramid treated with additional laser scans.
- Figure 5.12 Basic design of generating random line scan path.

- Figure 5.13 Diagram of scan-number maps for two random-line scan paths.
- Figure 5.14 Scan-number maps inside a square area: (a) vertical view and (b) isometric view.
- Figure 5.15 Diagram of generating initial and final point sets from a predefined probability density function.
- Figure 5.16 Scoring filter for a sample line taken from randomly generated sample lines: (a) notations and area of the scoring filter, (b) a generated scoring filter from a sample line, and (c) filter shape for transverse direction profile 1.
- Figure 5.17 An example scan-line scoring process: (a) one-dimensional scan-number distribution, (b) scan-number distribution profile in the X direction, and (c) normalized scores from a ridge filter, gradient filter, and average filter.
- Figure 5.18 Generated scan-number distributions using various scoring filters: (a) 3D profile, (b) 2D profile at  $Y = 0$  with a ridge filter, (c) 3D profile, (d) 2D profile at  $Y = 0$  with an average filter, (e) 3D profile, and (f) 2D profile at  $Y = 0$  with a gradient filter.
- Figure 5.19 Difference map calculation diagram: (a) current scan-number distribution, (b) target scan-number distribution, and (c) generated difference map.
- Figure 5.20 Score calculation for a sample scan line with a difference map and scoring filter.
- Figure 5.21 Square pocket fabricated with a random-point scan path:

(a) SEM image, (b) 3D surface profile data, and (c) machined depth compared to the process time.

Figure 5.22 SEM image of a pocket fabricated with a random-line scan path: (a) square pocket, (b) cross-shaped pocket, (c) triangular pocket, and (d) rectangular pillar.

Figure 5.23 Negative scan-number map and SEM images for (a) pyramid structures and (b) structures with peaks and valleys fabricated with a random -ne scan path.

Figure 5.24 Machining characteristics corresponding to parameter changes: (a) number of sample points, (b) minimum length, and (c) scoring filter width.

Figure 5.25 Diagram of the control parameters of the interface board and corresponding laser irradiation

Figure 5.26 Machining characteristics corresponding to parameter changes: (a) number of sample points, (b) minimum length, and (c) scoring filter width.

Figure 5.27 SEM images of square micropockets machined with different scan path generation parameters: (a) basic condition (6 sample points, 30 % minimum length, and 12  $\mu\text{m}$  filter width); (b) 2 sample points and (c) 70 % of width at minimum length.

Figure 5.28 Scan distributions with different scan path generation parameters: (a) basic condition (6 sample points, 30% minimum length, and 12  $\mu\text{m}$  filter width); (b) 2 sample points; and (c) 70% of width at minimum length.

- Figure 5.29 Reversed 3D data of (a) target structure and (b) simulated results in different perspectives.
- Figure 5.30 Fabricated glass structure with random line scan path (a) SEM image, (b) 3D surface profile.
- Figure 5.31 Comparison between simulation data and actual machined profile (a) position of comparison, (b) comparison results  $Y = 500 \mu\text{m}$ , (c) comparison results through  $X = 620 \mu\text{m}$ .
- Figure 6.1 Diagram of fabricated channel and experimental condition
- Figure 6.2 SEM images of sidewall of the fabricated channel (a) normal image (b) enlarged image
- Figure 6.3 Experimental images of capillary driven flow (a) glass microchannel and dyed solution (b) propagation of the dyed solution inside the fabricated glass microchannel
- Figure 6.4 Diagram of fabricated glass mold and experimental condition
- Figure 6.5 SEM images of glass molds
- Figure 6.6 Diagram of UV curing system and experimental setup
- Figure 6.7 SEM images of replicated polymer structures
- Figure 6.8 Diagram of fabricated glass mold and experimental condition
- Figure 6.9 Fabricated glass stand-alone structure (a) SEM image (b) magnified image
- Figure 7.1 MRR and surface roughness vs. aspect ratio for different glass processing technologies

# List of Tables

Table 1.1	Qualitative comparison of glass micromachining technologies
Table 2.1	Material properties of soda-lime glass
Table 2.2	Absorption coefficient corresponding to the copper sulfate absorbent.
Table 2.3	Absorption coefficient corresponding to the copper sulfate absorbent.
Table 5.1	Experimental condition for square micro pocket machining
Table 5.2	Machining condition for square micro pocket machining with random-point scan path
Table 5.3	Laser micromachining conditions for the study of the random-line scan path generation parameters.
Table 5.4	Path generation conditions



# Chapter 1

## Introduction

### 1.1. Research Background

Glass is a promising material that is widely used in micro total analysis systems ( $\mu$ -TASs), microelectromechanical systems (MEMS), display devices, and microfluidics due to its unique properties, such as biocompatibility, chemical stability, and mechanical hardness. Since these applications are mainly associated with geometries of tens of micrometers, glass micromachining is a necessary technique for creating specific structures for above mentioned applications. Glass microchannels for microfluidics are commonly studied for use in industry, and channel widths of tens of micrometers to a hundred micrometers are fabricated mainly for such applications [1-2]. High-aspect-ratio glass microchannels have particular advantages for specific applications relating to microfluidics, such as cell separation [3], microneedles [4], and capillary-driven flow generation [5]. Additionally, for microfluidic applications, glass materials have been widely

studied in relation to cell culturing owing to their biocompatibility and suitability for optical devices.

The unique properties of glass make the material promising; however, other aspects of glass, such as its brittleness and amorphous microstructure, limit associated material processing technologies, making it difficult to process glass materials with specific target geometries. As shown in Table 1.1, it is difficult to process glass using conventional or even nontraditional manufacturing processes.

To overcome the hard-to-machine characteristics of glass, different processing methods can be applied to fabricate various glass microstructure geometries, and mechanical cutting and chemical etching are widely used methods for processing glass materials. Ductile regime machining was investigated for mechanical cutting purposes due to its precise processing ability. Glass channels of hundreds of micrometers in width were fabricated with polycrystalline diamond tools or diamond coated tools [6–8], and precise glass cutting was made possible by ductile regime machining; however, the process needs shallow-depth cuts of around a hundred nanometers, in turn requiring sophisticated tool control technology and machine tools with high stiffness.

**Table 1.1**  
**Qualitative comparison of glass micromachining techniques**

Process	Ease of technique	Precision	Aspect ratio	Shape change
Mechanical cutting	○	◎	×	○
Chemical etching	○	△	×	×
CO <sub>2</sub> laser beam micromachining	◎	×	△	◎
Hot embossing	△	○	△	×
Electrochemical Discharge machining	△	△	○	○
Deep reactive ion etching	×	○	○	×
Femtosecond laser beam micromachining	×	○	◎	◎

(◎ = excellent, ○ = good, △ = poor, × = bad)

Chemical etching of glass has also been widely studied for industrial applications due to its suitability for mass production. Various studies have focused on fabricating glass with a low cracking tendency and high aspect ratio [9-10]; however, due to the amorphous microstructures of glass materials, it is difficult to fabricate stiff structures and specific target geometries with chemical etching. Fabricating high-aspect-ratio structures with scales of several tens of micrometers is even more challenging. Most industry-friendly processes are limited to aspect ratios of around 2.0, which restricts the use of glass materials. Complicated experimental setups are needed to fabricate glass microstructures with high aspect ratios.

Owing to their ease of system setup and diverse industrial applications, industry-friendly unconventional processes such as CO<sub>2</sub> laser micromachining, electrochemical discharge machining (ECDM), and hot embossing have been widely used to fabricate high-aspect-ratio structures. For CO<sub>2</sub> laser micromachining, a process that eliminated crack generation was studied to fabricate channel arrays and cell patterns on glass [11]. To fabricate microchannels on Pyrex glass with high aspect ratios, without introducing defects, the polydimethylsiloxane(PDMS) layer was used as a protective layer [12]. Although CO<sub>2</sub> laser micromachining is widely used in industry, high-aspect-ratio fabrication of complex shapes remains difficult:

directly absorbed heat energy leads to fabricated structures that taper, as with other laser micromachining processes. Via holes, channels, and vertical structures were drilled on Pyrex glass using ECDM [13]. The researchers proposed that microholes of 60  $\mu\text{m}$  diameter and 150  $\mu\text{m}$  depth could be machined. The hot embossing method was also examined using a glassy carbon mold to fabricate acute-angle high-aspect-ratio glass patterns [14].

Because these techniques employ tools and molds, precise control capability and tool-wear problems need to be solved. Overall, although industry-friendly techniques have some advantages, they limit the aspect ratio.

Femtosecond laser micromachining and deep reactive ion etching are two well-known methods of fabricating high-aspect-ratio and highly versatile microstructures with fabricable geometries. One study fabricated microchannels with an aspect ratio of 26 [15]. It showed that this technique for machining transparent material from the back could produce deeper channels. Due to the characteristics of the femtosecond laser, transparent materials such as glass could be machined internally by setting the focus inside the material. Various complex three-dimensional structures with a size of a few hundred micrometers were fabricated inside glass materials [16-17]. With deep reactive ion etching (DRIE), High-aspect-ratio structures can be fabricated with deep reactive ion etching because of its anisotropic etching

characteristics. Straight trenches on fused silica and borosilicate glass with aspect ratios of seven and eight, respectively, were fabricated using a DRIE process [18]. Such processes can produce high-aspect-ratio structures from glass, but their low material-removal rates and complex manufacturing environments, such as their need for a vacuum, complex optical systems, and low environmental vibrations, make them inappropriate for industrial applications.

Several material processing techniques can handle glass materials, but they are unsuitable for achieving both highly versatile geometries and easy processing, as depicted in Fig. 1.1. An industry-friendly technique for achieving versatile glass geometries could broaden the potential applications of glass materials.

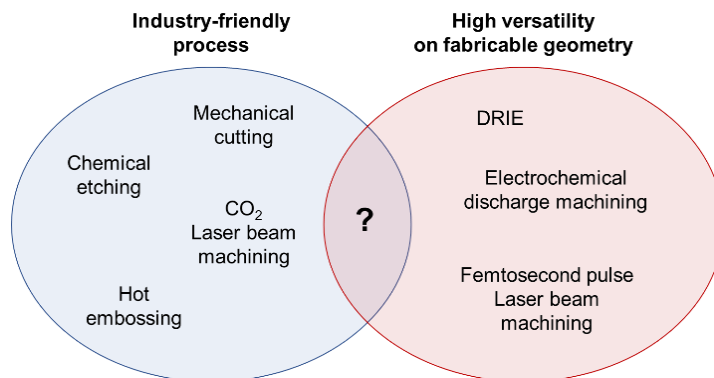


**Fig. 1.1 Glass material processing techniques classified according to ease of technique and versatility of processable geometry.**

The laser-induced backside wet etching (LIBWE) is a widely studied process for overcoming the limitations of industry-friendly techniques for machining glass materials. In the LIBWE process, the laser indirectly processes a transparent material by heating a liquid absorbent that is in contact with the substrate. Compared to previous glass micromachining processes, the LIBWE process has the advantages of technical ease and shape flexibility. Various microstructures can be processed using simple setups without additional closed loop controls or focus adjustments. High shape flexibility can also be achieved by using a scanner. Owing to its advantages over other glass micromachining processes, the LIBWE process has been studied as a method for processing various transparent materials. The main mechanism of material removal through high-energy-absorption LIBWE processes has been studied. Using silver nanoparticles obtained from silver nitrate ( $\text{AgNO}_3$ ) precursors during a LIBWE process, with a 527 nm wavelength laser, additional heat was absorbed at the laser irradiation spot and created localized high temperature and pressure, enabling the glass to be processed [19]. Using a copper sulfate absorbent and an Nd: YVO<sub>4</sub> laser, the copper oxide generated and deposited during the process absorbed the heat energy and facilitated a LIBWE process with a higher machining speed [20]. Based on such machining principles, various microstructures have been fabricated for

different applications. Micropockets and high-aspect-ratio slanted and bent microchannels on fused silica were fabricated by moving the substrate with stationary laser irradiation [21-22]. Ridges and channels with sub-millimeter width for wettability control were fabricated using a near-infrared laser and an aqueous nickel sulfate solution [23]. Also, various studies of surface treatment and the utilization of such treated surfaces have been conducted using chemical reactions during the LIBWE process. A submicron-scale amorphous sapphire layer with embedded silver nanoparticles was fabricated from crystalline sapphire [24]. Not only silver, but embedded copper wires inside glass microchannels using adsorbed copper oxide, could be produced during the LIBWE process [25]. Although extensive research on the LIBWE process has been conducted, manufacturable geometries have remained simple due to the geometric errors and cracks caused by the interaction of the laser and the generated bubbles.



## 1.2. Research Objective

This study fabricated various shapes of structures on glass surfaces, including high-aspect-ratio channels, simple micropockets, and complicated structures for certain applications, using the near-infrared (NIR) LIBWE process with a phosphoric acid-added copper sulfate solution (Fig. 1.2) [26]. The reasons for the limited processable depth of the NIR LIBWE process using a copper sulfate absorbent were investigated based on *in situ* observations of the fabrication process and elemental analysis. The benefits of phosphoric acid for crack suppression were explored by comparing the results for the copper sulfate solution with and without added phosphoric acid. The study also investigated the effects of phosphoric acid and other process parameters on maximum processable depth, sidewall roughness, fabrication speed, and machinability, based on experimental results and relevant theories. Finally, a new scan path generation strategy for fabricating various three-dimensional structures was proposed, and its feasibility was experimentally investigated by fabricating various structures and examining the characteristics of the scan path generation.

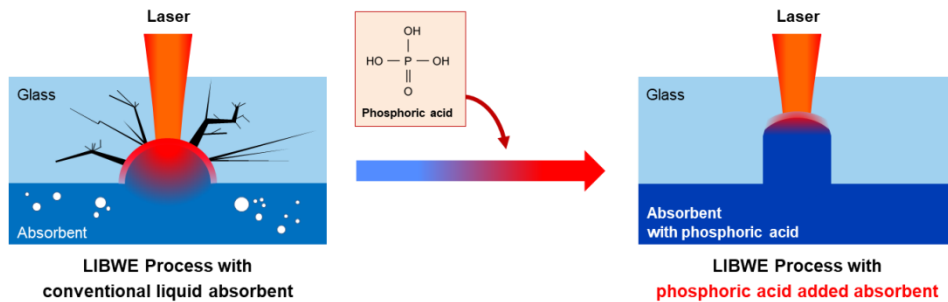


**Fig.1.2 Crack-suppressing LIBWE process with a phosphoric acid added absorbent.**

### 1.3. Dissertation Overview

Chapter 1 has so far introduced the main issues regarding the fabrication of glass microstructures using established processes, highlighting the importance of micromachining glass materials and the limits of various previous processes. This section introduces the research background, the necessity of researching industry-friendly glass micromachining techniques, and the research objective.

Chapter 2 presents the background theory of LIBWE. The relevant background theory regarding LIBWE using a phosphoric acid-added absorbent is also explained, such as the reaction between phosphoric acid and silicon dioxide, and the laser absorption in a liquid phase absorbent. The experimental setup and procedures are also presented in this section.

Chapter 3 describes the investigation of the machining mechanism of LIBWE with a phosphoric acid-added absorbent. The LIBWE processes with and without added phosphoric acid were observed using *in situ* process images and measurement of the chemical composition maps of machined walls. The section explains the effect of the silicon phosphate layer based on a comparison of crack generation behavior and crack suppression inside a channel.

Chapter 4 describes the investigation of the machining characteristics of LIBWE with the phosphoric acid-added absorbent. The researchers conducted parametric studies of the phosphoric acid concentration, copper sulfate concentration, laser power, laser scanning speed, and number of scans, and the results are explained based on their effects on maximum aspect ratio, sidewall roughness, fabrication speed, and machinability.

Chapter 5 explains the fabrication of various microstructures from a glass material using LIBWE with a phosphoric acid-added absorbent to evaluate processability. A new scan path generation strategy for achieving fewer geometry errors was tested by fabricating various glass microstructures with the proposed scan paths. Proposed scan path generation strategies were compared to determine the material-removal rate, normalized depth deviation,

and average surface roughness. Based on the results, a complicated structure was fabricated to evaluate the degree of precision of the generated scan path.

Chapter 6 describes the fabrication and feasibility testing of glass structures for certain applications: high-aspect-ratio microchannels for capillary-driven flow, glass molds for UV reverse contact imprints, and a standalone glass feature for glass components.

Chapter 7 presents the conclusion and discussion of the study.

# Chapter 2

## The LIBWE process

### 2.1. LIBWE

The LIBWE process is a machining process that uses a laser beam and a laser-absorbing liquid to indirectly machine transparent materials. Because of the machining proceeds at the rear side and the cooling effect of a liquid absorbent, transparent materials can be machined with fewer negative effects than by direct laser beam machining, such as recast layers, tapered shapes, and thermal effects.

Heating and explosion of the liquid absorbent are the two main mechanisms of the LIBWE process, as shown in Fig. 2.1 [27]. A laser beam that is irradiated from the top of the glass penetrates the workpiece and is absorbed at the interface between the glass and the liquid absorbent (Fig. 2.1a). The absorption of laser energy by the liquid absorbent causes the absorbent to heat up, evaporate, and explode (Fig. 2.1b). Intensive heat absorption in a thin liquid layer causes a dramatic temperature rise, which can melt the glass

substrate [27]. The local high temperature transforms the glass into a glassy state, and the explosion of the vapor helps to remove the molten glass from the substrate. One study measured the transient pressure caused by laser irradiation of the absorbent and the subsequent explosion of the evaporated vapor, showing that the vapor pressure was sufficient to remove the molten glass, thus contributing to the fabrication process [28].

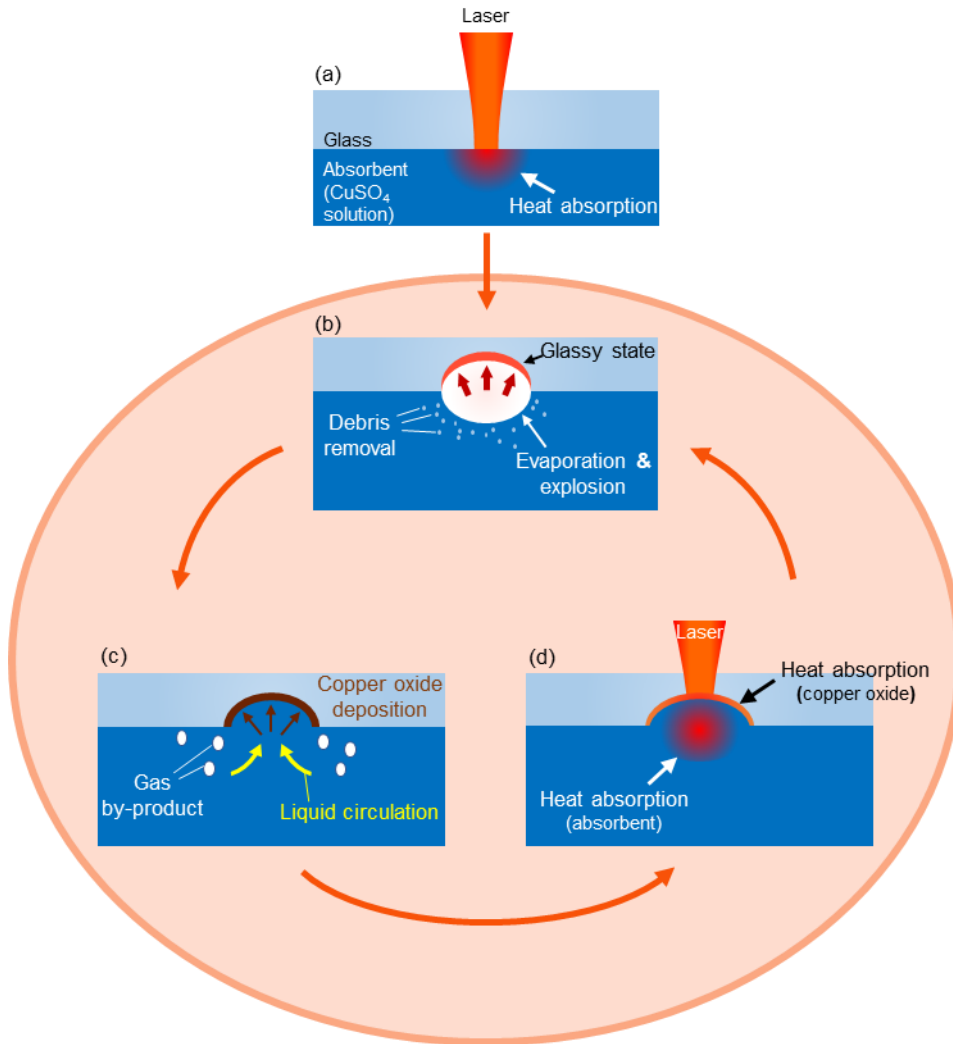
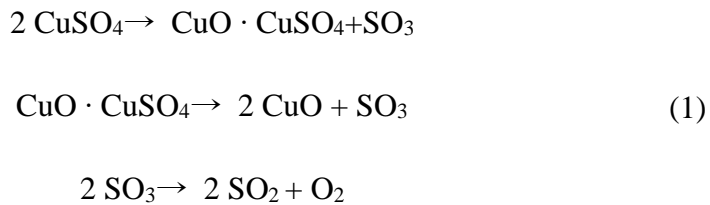
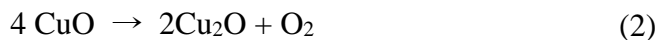


**Fig. 2.1 The LIBWE machining process with a copper sulfate absorbent.**

In the LIBWE process employing an NIR laser, with the copper sulfate aqueous solution mainly used as an absorbent, thermal decomposition of the copper sulfate provides additional energy absorption. Evaporation owing to laser irradiation causes the copper sulfate to precipitate and produces thermal decomposition of the copper sulfate into copper oxide and gas-phase sulfur oxide (Fig. 2.1c) [29]. Because the decomposition temperature (600°C) is lower than the softening point of soda-lime glass (726°C), under conditions that make glass processing possible, thermal decomposition of copper sulfate occurs. The chemical equation for the copper sulfate thermal decomposition is as follows:



Additionally, copper (I) oxide can be produced from generated copper (II) oxide in a low-oxygen and high-temperature environment, as shown in Fig. 2.2 [30]. The chemical equation for the reaction is shown below:





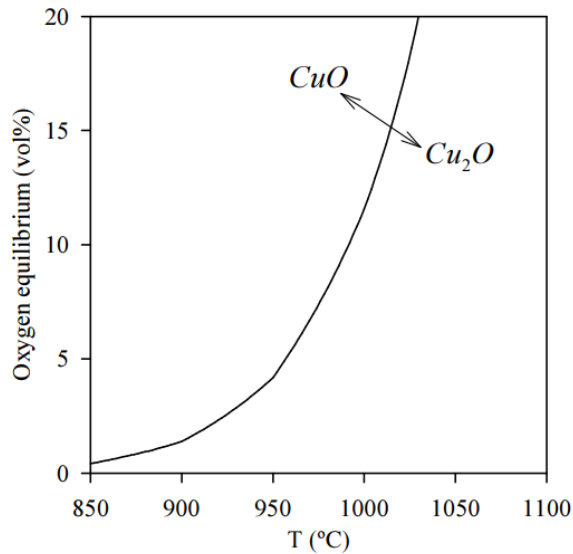


**Fig. 2.2 Equilibrium between copper (II) oxide and copper (I) oxide corresponding to the oxygen concentration and temperature [30].**

Copper oxide generated during a LIBWE process is adsorbed onto the processed surface (Fig. 2.1c). Researchers measured the heat absorption coefficient of the copper oxide layer and found that the adsorbed copper oxide layer improved the heat absorption [31] (Fig. 2.1d). Following the mechanical and chemical processes, because the absorbent was in a liquid state, the absorbent could recirculate inside the hollow region. As a result, the LIBWE process could continuously remove the glass. The decomposition and adsorption process also proceeded continuously until the liquid absorbent circulated inside the channel.

## 2.2. Reactions between Glass and Phosphoric acid

The chemical reaction between phosphoric acid and silicon dioxide (Fig 2.3) also occurs when an absorbent with added phosphoric acid is used. It is known that pure orthophosphoric acid ( $\text{H}_3\text{PO}_4$ ) (Fig. 2.3a) does not react with silicon dioxide; however, pyrophosphoric acid ( $\text{H}_4\text{P}_2\text{O}_7$ ), produced by dehydration and condensation of orthophosphoric acids, reacts with silicon dioxide. The reaction between phosphoric acid and glass is depicted in Fig. 2.4. Experimental results showed that orthophosphoric acid reacts with glass when the temperature of the acid is higher than  $200^\circ\text{C}$ , because condensation of orthophosphoric acid into pyrophosphoric acid proceeds aggressively above  $200^\circ\text{C}$  and the etching speed increases rapidly above the threshold temperature ( $200^\circ\text{C}$ ) [32]. The reaction between glass and phosphoric acid proceeds as a P–O bond in pyrophosphoric acid, which is interchanged with the Si–O bond in the glass, thus generating P–O–Si bonds on the surface (Fig 2.3). This silicon phosphate layer on the surface can act as a protective layer. The chemical reaction on the phosphoric acid-treated glass surface is inhibited owing to the silicon phosphate coating on the glass surface [33]. The chemical resistivity of this phosphate layer was proved by chemical etching

with fluoric acid, showing that the protective layer remained despite other pure glass materials being dissolved.

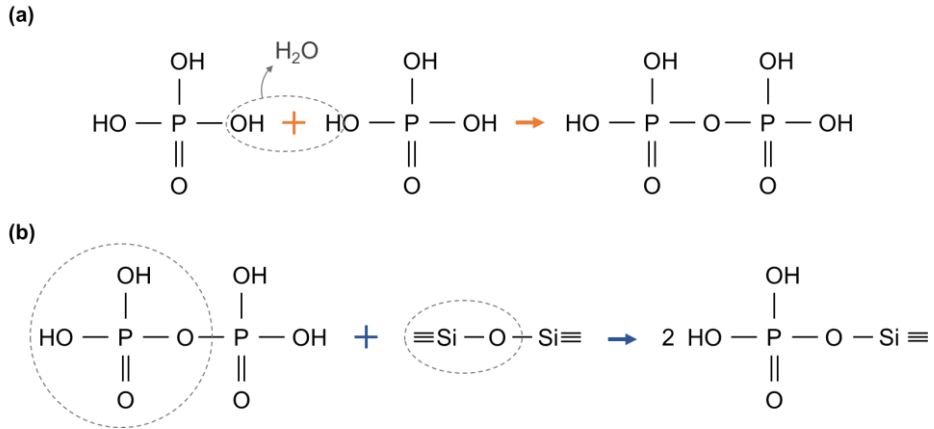


**Fig. 2.3 Equation for the chemical reaction between phosphoric acid and silicon dioxide: (a) dehydration of orthophosphoric acid and (b) reaction between pyrophosphoric acid and silicon dioxide.**

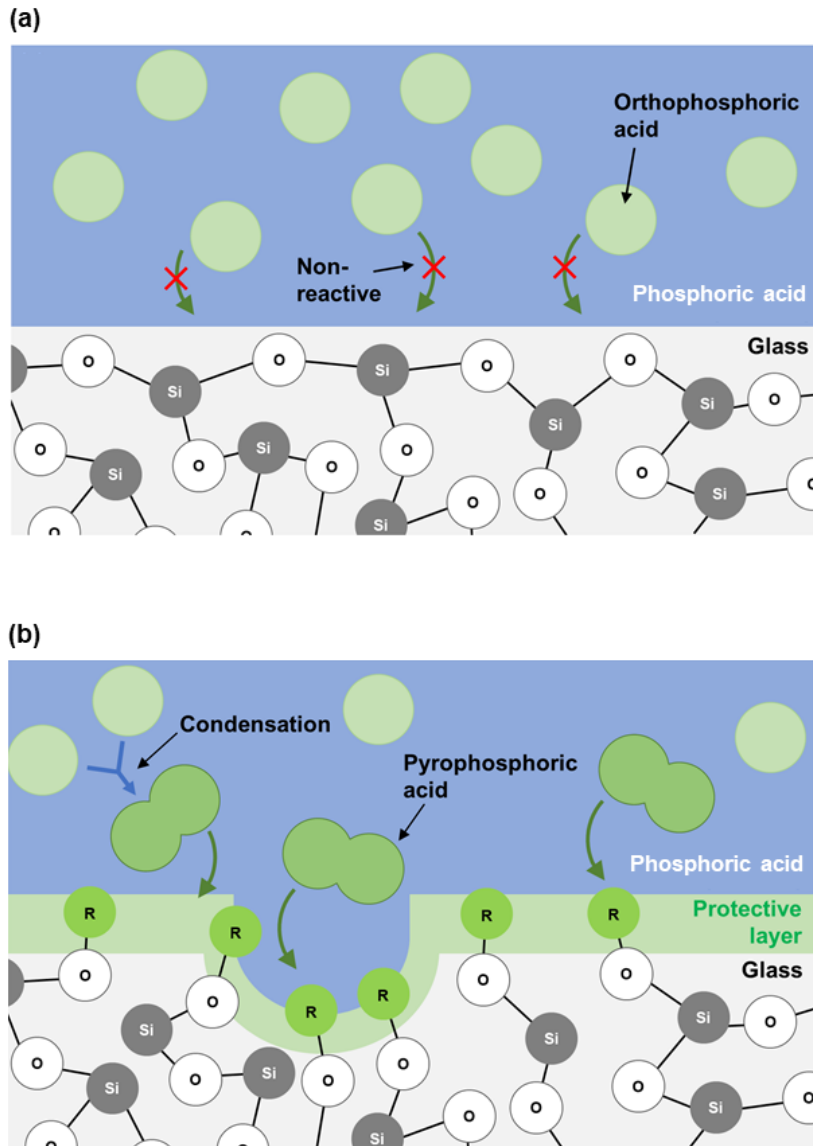


**Fig. 2.4 Diagram of the reaction between phosphoric acid and glass: (a) under 200°C and (b) over 200°C.**

## 2.3. Interaction between a Laser Beam and Liquid Absorbent

Energy absorption aspects also have a great influence on fabrication characteristics. Laser power and distance between each pulse are important factors to control in the process with a pulsed laser. Also, because the laser energy is absorbed in the liquid absorbent, absorbance of the liquid solution affects the process characteristics. In this study, laser power and scan speed were adjusted to control the laser characteristics, and copper sulfate concentration was adjusted to control absorbance. Absorbed pulse power density ( $I$ ) in the liquid absorbent showed Gaussian distribution as depicted in Fig. 2.5a. The equation of absorbed pulse power density profile can be written as follows:

$$I(x, y) = \frac{2\alpha P}{\pi R^2} \exp\left(-\frac{2(x^2 + y^2)}{R^2}\right) \quad (3)$$

where  $P$  is the peak pulse power,  $R$  is the beam radius, and  $\alpha$  is the absorption coefficient of the absorbent.

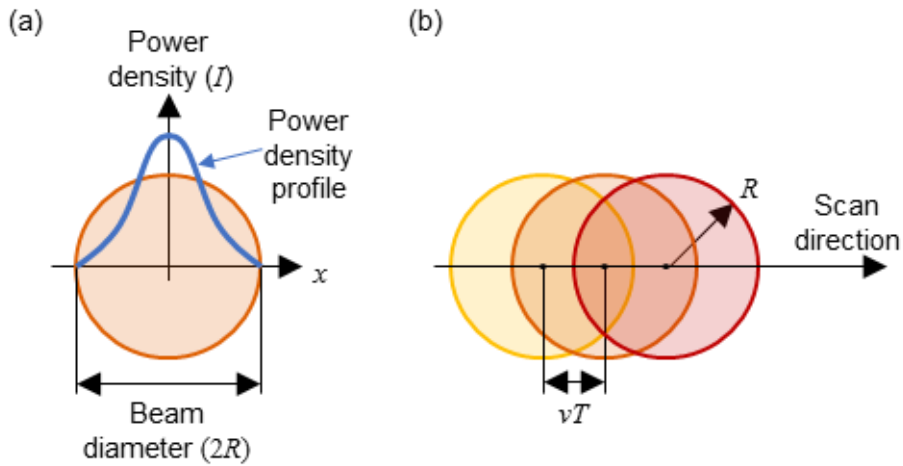


**Fig. 2.5 (a) Laser power density profile of a single pulse and (b) laser irradiating area in milling process with single scan direction.**

Based on the pulse power density profile, it was possible to determine the absorbed energy density formula. In laser direct machining, because most of the laser energy is absorbed on the surface, laser fluence is an important factor for determining the process threshold. In LIBWE, because the laser can penetrate the liquid absorbent and be absorbed into its volume, absorbed energy density has become an important factor for determining processability. Because absorbed laser energy at a certain point is proportional to the energy at the center of the beam, it was possible to assume that the power and energy density absorbed at the center could represent the overall value; thus, we only concerned ourselves with the energy density along the scan path ( $y = 0$ ). Pulse

duration (100 ns) was much shorter than the period between two pulses (20  $\mu$ s), so it was reasonable to assume that a single laser pulse irradiated a single spot without moving. For the pulsed laser, the power and scan rate (number of laser pulses per unit length) were important for the machining characteristics. The idea of implanting the scan rate was studied, showing its critical effect on the laser micromachining of glass [33]. To apply the scan rate effect, the total value of overlapped pulse energy was calculated for the energy density. Based on these assumptions, absorbed energy density ( $q$ ) on a single spot in a single scan can be derived as below:

$$q = \sum_{i=-n}^n \tau I(i) = \frac{2\alpha P\tau}{\pi R^2} \sum_{i=-n}^n \exp\left(-\frac{2(vT)^2}{R^2} i^2\right), \quad (n = \left\lceil \frac{R}{vT} \right\rceil) \quad (4)$$

where  $v$  is the laser scanning speed,  $n$  is the number of pulses overlapped in the beam radius,  $s$  is the pulse duration, and  $T$  is the period between two pulses. The pulse irradiation area during the process is depicted in Fig. 2.5b.

Average absorbed power density during the whole fabrication process could also be derived. When the number of scans was large enough, the irradiation point did not match with the previous positions, so the laser energy absorbed at a single spot could be explained, not with a discrete form of

energy input, but with an average form. The average power density of a single pulse in the scan direction ( $I_{avg,x}$ ) can be written as follows:

$$I_{avg,x} = \frac{1}{2R} \int_{-R}^R I(x) dx \quad (5)$$

Based on the  $I_{avg,x}$  and given experimental data, average absorbed power density ( $I_{avg}$ ) can be derived as follows:

$$\begin{aligned} I_{avg} &= I_{avg,x} \times (\text{net irradiation time}) \\ &\quad \times (\text{scan count per unit time}) \\ &= I_{avg,x} \times \frac{L}{vT} \tau \times \frac{v}{L} \\ &= \frac{\alpha P \tau}{\pi R^3 T} \int_{-R}^R \exp\left(-\frac{2x^2}{R^2}\right) dx \\ &= 1.196 \left(\frac{\tau}{\pi R^3 T}\right) \alpha P \end{aligned} \quad (6)$$



## 2.4. Experimental Procedure

Micrometer-scale channels were fabricated on a glass substrate with the system depicted in Fig. 2.6. The X and Y axes moved the workpiece and reservoir to the correct spot for the laser to irradiate the workpiece. A galvanometer scanner (SCANcube<sup>®</sup> 10, Scanlab, Germany) was installed on the Z axis so that the laser focus could be set.

An ytterbium-doped fiber laser (IPG, YLP-C-1-100-20-20, Germany) with a wavelength of 1,064 nm, a pulse duration of 100 ns, and a spot diameter of 40  $\mu\text{m}$  was used for the LIBWE process. The laser beam power could be set up to 20 W, and the laser path was controlled with a galvanometer scanner.

The glass substrate was positioned on a support and pressed with a holder to suppress the overflow of liquid absorbent above the substrate. Polymethyl methacrylate (PMMA) was used for the absorbent reservoir, support, and holder to avoid any chemical reaction between the acidic absorbent and the surrounding equipment. Soda-lime glass (JMC Glass, Korea) with a size of  $15 \times 15 \times 1.9 \text{ mm}^3$  was used as a substrate. Detailed properties of the substrate glass are listed in Table 2.1.

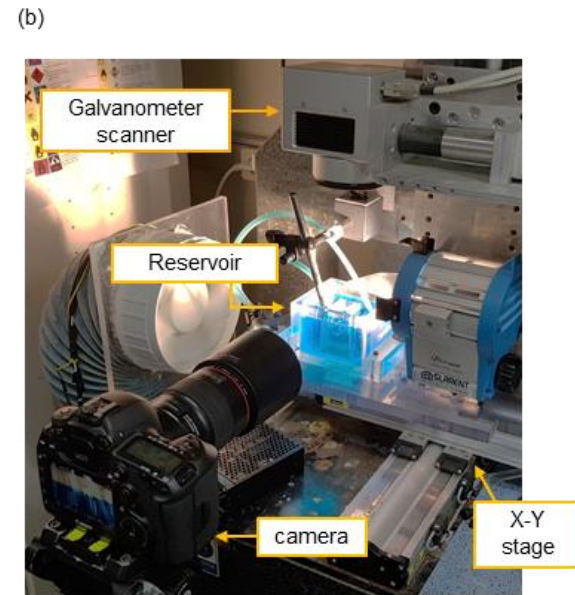
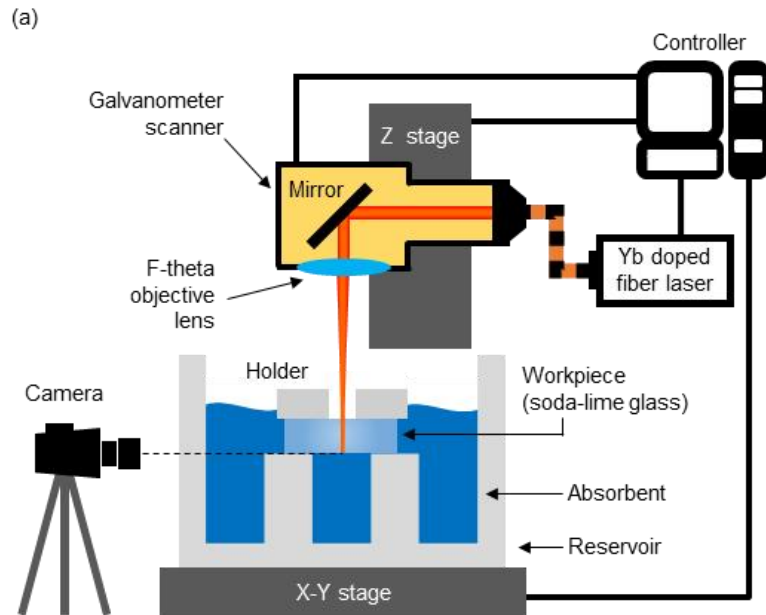


**Fig. 2.6 (a) Schematic diagram of the LIBWE system, (b) picture of the experimental setup.**

**Table 2.1**  
**Material properties of soda-lime glass**

Property	Value
Modulus of elasticity	7.2 kPa
Modulus of rigidity	3.0 kPa
Poisson's ratio	0.23
Density	2,530 kg/m <sup>3</sup>
Coefficient of thermal stress	0.62 mPa/°C
Thermal conductivity	0.937 W m/m <sup>2</sup> °C
Specific heat	0.21
Softening point	726°C
Annealing point	546°C

*In situ* observations were performed to determine the effects of phosphoric acid on the LIBWE process. Changes in the liquid flow, bubbling, vapor layer, channel shape, and corresponding time were observed using a digital single-lens reflex camera (EOS 5D, Canon, Japan) and a magnification lens. By using a short focal depth and setting the focal plane on the channel, it was possible to obtain images of the machining procedure inside the glass channel.

For the elemental analysis of the machined surface, energy-dispersive X-ray spectroscopy (EDS) analysis was conducted. The processed channel wall surface was prepared by cutting the workpiece along the fabricated channel and polishing the outside of the fabricated channel wall. EDS mapping (MERLIN Compact, Zeiss, Germany) was performed to characterize the chemical composition of the channel sidewall and compare it with the *in situ* observation results. A cross-section of the channel was prepared by cutting and polishing the middle of the channel, then observing it with a scanning electron microscope (SEM) (JSM-6360, JEOL, Japan) to observe the channel shape. The absorption coefficients of the absorbents were measured using ultraviolet–visible (UV-VIS) spectroscopy (JASCO V-770, JASCO, USA), and the results corresponding to the concentrations of copper sulfate are listed in Table 2.2. The average surface roughness of the sidewalls was measured with a 3D surface profiler ( $\mu$ Surf, Nanofocus, Germany).

The phosphoric acid concentration, copper sulfate concentration, laser power, and laser scanning speed were adjusted as the machining parameters, and the experimental parameters for the studies are listed in Table 2.3. The basic process condition was set as 112 g/L of copper sulfate, 20 wt% of phosphoric acid, 18 W laser power, and 150 mm/s scanning speed, and those conditions were labeled as shown in Table 2.3. When a parameter was

changed, other parameters were fixed at the base value. Three channels were fabricated and evaluated for each machining condition to insure the reliability of the results and determine the range of possible variations.

**Table 2.2**

Absorption coefficient corresponding to the copper sulfate absorbent.

Copper (II) sulfate concentration [g/L]	Absorption coefficient [cm <sup>-1</sup> ]
64	0.23
88	0.32
112	0.39
136	0.43
160	0.44

**Table 2.3**

Absorption coefficient corresponding to the copper sulfate absorbent.

Variable	Value
Copper (II) sulfate concentration [g/L]	64, 88, <b>112</b> , 136, 160
Phosphoric acid concentration [wt%]	0, 10, <b>20</b> , 30, 40
Laser power [W]	14, 16, <b>18</b> , 20
Scan speed [mm/s]	75, 100, 125, <b>150</b> , 175, 200
Repetition rate of pulsed laser [kHz]	50
Scan length for milling process [mm]	1.2

Automatic or manually generated scan paths for the machining system became necessary as the scan path and machining conditions became more complex. To solve this problem, a scan path generation and data implementation system, directly controlled by the controller board, was designed and installed, as depicted in Fig. 2.7. Scan paths, both manually derived ones and others generated automatically by MATLAB, were written as text files for transfer to the controller. To control the laser directly, an interface board (RTC4, Scanlab, Germany) was used. Through the control system and interface board, laser power and frequency data were transferred to the laser source as bitwise data, and scan path parameters (position, scanning speed, and laser delay) were transferred to the scanner.

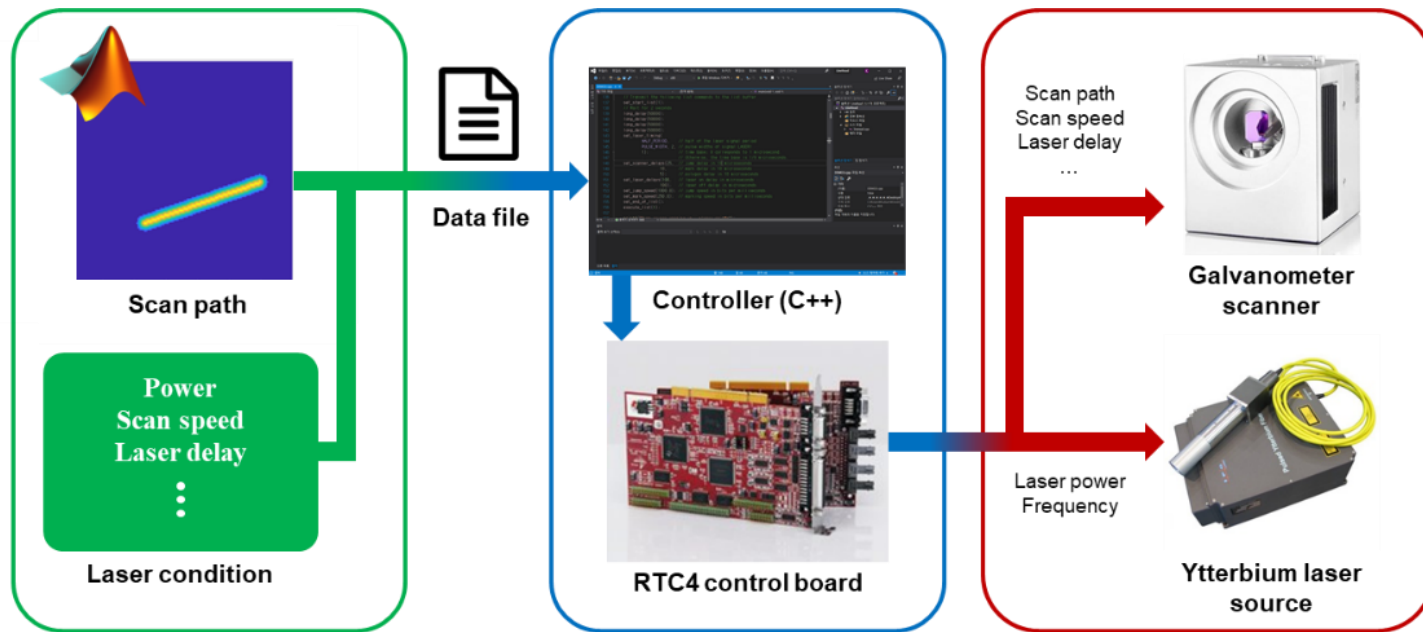


**Fig. 2.7 Schematic diagram of the laser source and scanner control system with generated scan path data.**

# Chapter 3

## LIBWE using Phosphoric Acid-Added Absorbent

This chapter explains how LIBWE processes using a copper sulfate absorbent and a phosphoric acid-added absorbent, respectively, were compared to determine the underpinning principle of crack suppression and the expansion of the manufacturable aspect ratio by using a phosphoric acid-added absorbent. To investigate the machining principle, *in situ* visual observations and chemical element mapping were conducted for each process. Important process characteristics such as bubble generation, vapor layer, and chemical element adsorptions were explained by the interaction between laser irradiation and heat-induced chemical reactions. As a result, the principles of crack generation and crack suppression, respectively, for the phosphoric acid-added absorbent were explained.



### **3.1. Crack Generation in Near-Infrared LIBWE Process**

The fabrication process with the copper sulfate absorbent and the mechanism of crack generation will be discussed in this section. As depicted in Fig. 3.1, crack generation during LIBWE processes with copper sulfate solution absorbent was already known to generate bubbles, and this phenomenon was assumed to be the major cause of crack generation. Diagrams and *in situ* observations of the channel fabrication process with the copper sulfate absorbent are described in Fig. 3.1, and the corresponding elemental analysis is depicted in Fig. 3.2. Overall, the copper sulfate absorbent process could be separated into three steps based on the elemental analysis and the *in situ* observations: initial state, bubble generation state, and crack generation state.

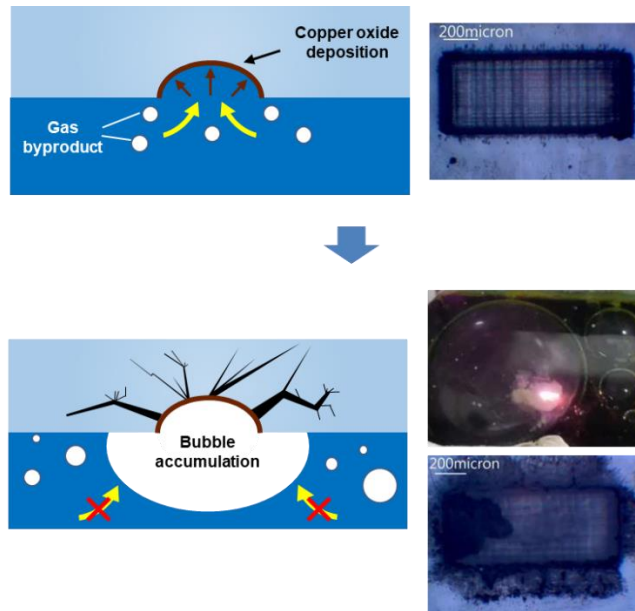


**Fig. 3.1 Crack generation during the LIBWE process with copper sulfate solution absorbent [34].**

In the initial state, the channel depth was shallow and the laser irradiation point was barely detectable (Fig. 3.2a). An expanded bubble immediately collapsed and was separated. Separated bubbles were flushed away and the liquid absorbent circulated inside the channel. Some bubbles remained under the glass surface because the thermal decomposition of copper sulfate produced sulfur oxide gas; however, little copper was detected when the channel depth was low, and bubbles were not detected (Fig. 3.3a).

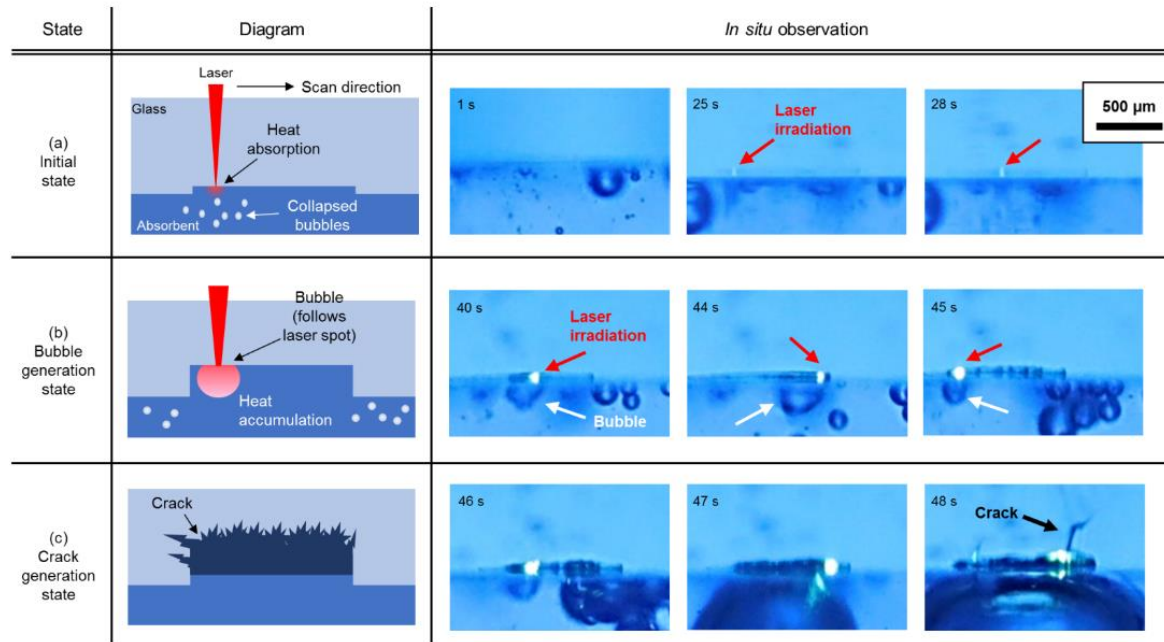


**Fig. 3.2** Diagrams and *in situ* observation of the LIBWE milling process in copper sulfate absorbent: (a) initial state, (b) bubble generation state, and (c) crack generation state.

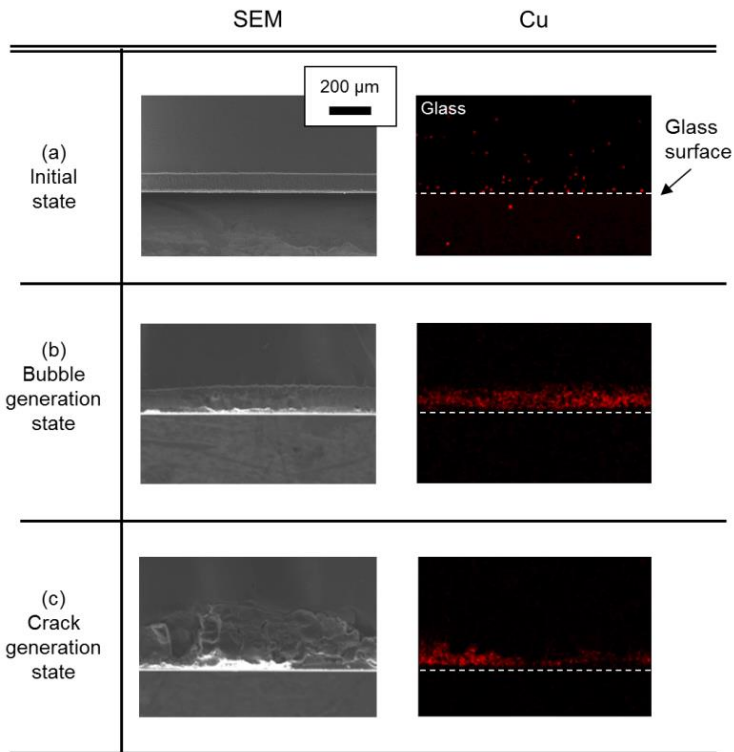


**Fig. 3.3 SEM image and elemental analysis of sidewall machined in copper sulfate absorbent: (a) initial state, (b) bubble generation state, and (c) crack generation state. Red dots are detected copper element.**

In the bubble generation state, an expanded bubble began to attach at the laser irradiation point as the channel depth increased (Fig. 3.2b). The copper element was detected on the processed site after the bubble was created below the irradiation spot (Fig. 3.3b). This excessive copper oxide adhesion could be explained by the positive feedback of the heat energy supply, thermal decomposition, and gas by-product generation, which are depicted in Fig. 3.4. When the liquid absorbent circulated properly inside the channel, the absorbed energy was dispersed from the laser-irradiated area, so heat did not accumulate. Excessive heat accumulation was explained by a simulation showing that the temperature inside the bubble created by a 1,064 nm laser could reach over 1,800 K, while the outer liquid's temperature changed little [35]. When the intact bubble prevented the circulation of liquid, the cooling effect of the liquid was disrupted, and heat energy started to accumulate. The accumulation of heat enhanced the thermal decomposition of the copper sulfate, which produced gas-phase by-products and enlarged the bubble. This copper oxide adhesion enhancement due to the bubble was identified through the elemental analysis results. The increase in gas by-products made it difficult for the liquid absorbent to come into contact with the irradiation spot. As a result, once the bubble started to attach to the laser-irradiation point, the

bubble generation and copper oxide adhesion phenomenon continued the positive feedback process until crack generation occurred.

The increase in the laser irradiation counts resulted in a crack generation state, as shown in Fig. 3.2c. Adsorbed copper oxide continuously raised the energy absorption rate and created more gas by-products, which resulted in the bubble's size increasing. When the enlarged bubble blocked the whole irradiation area, no liquid phase absorbent could come into contact with the channel, which caused rapid heat accumulation at the irradiation point. This cooling interruption caused excessive thermal stress on the substrate and generated cracks on the channel. Based on the elemental analysis of the crack-generated surface (Fig. 3.3c), the crack tore off the sidewall of the channel and propagated throughout the internal substrates; thus, no copper was detected at the cracked part of the channel. This superfluous copper oxide adhesion was observed visually after the machining process, as depicted in Fig. 3.5.

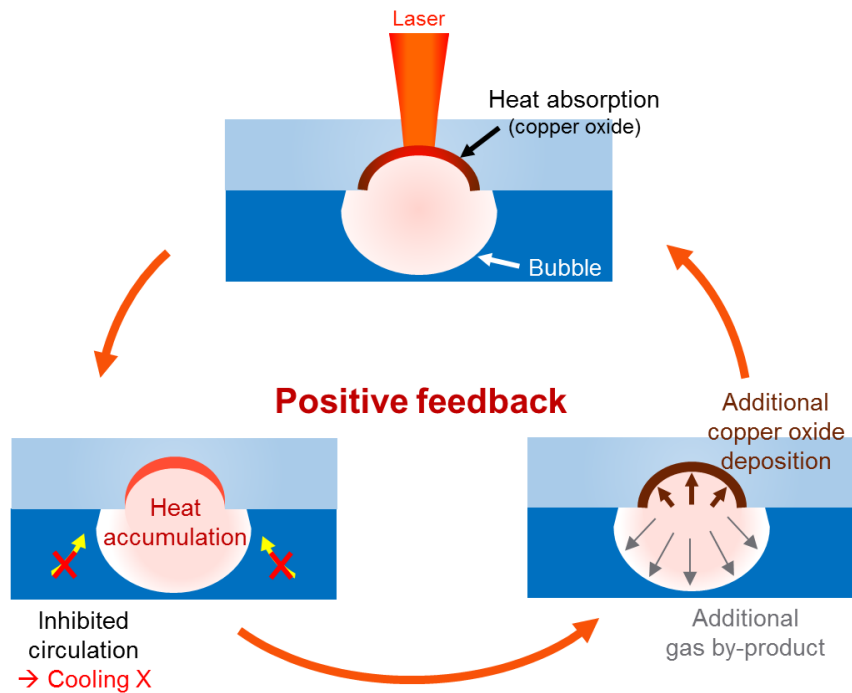


**Fig. 3.4 Diagram of heat accumulation positive feedback inside a bubble.**

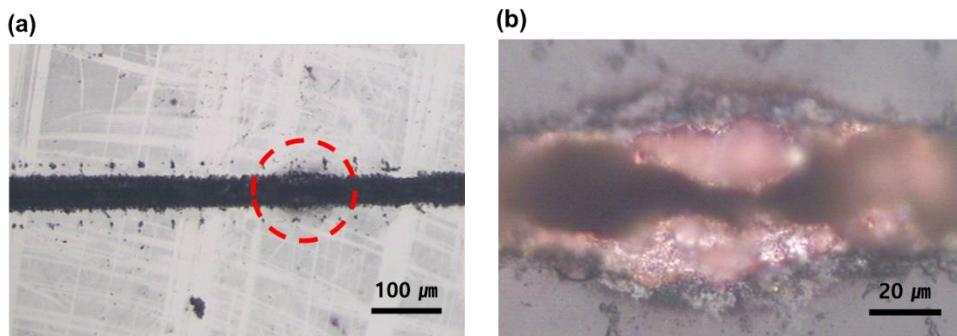


**Fig. 3.5 Excessively deposited copper oxide on the machined channel. (a) channel overview (b) enlarged image of excessively deposited copper oxide.**

## 3.2. Phosphate Protective Layer Generation

In this section, the fabrication process using the absorbent with added phosphoric acid will be described and compared with the process using the copper sulfate absorbent. Compared to the LIBWE process using the copper sulfate absorbent, crack generation was suppressed by the absorbent with phosphoric acid. The cracking was delayed so that the fabricable channel depth could be increased. Fig. 3.6 shows the cross-section of the fabricated high-aspect-ratio channel fabricated using the absorbent with phosphoric acid (40 wt%). The depth of the channel in Fig. 3.6 is 640  $\mu\text{m}$ , with an average width of 21  $\mu\text{m}$ , which was impossible to produce using the copper sulfate absorbent without phosphoric acid. Fig. 3.7 shows the diagrams and *in situ* observations for the channel fabrication process using the absorbent with phosphoric acid. The corresponding elemental analysis results are depicted in Fig. 3.8.



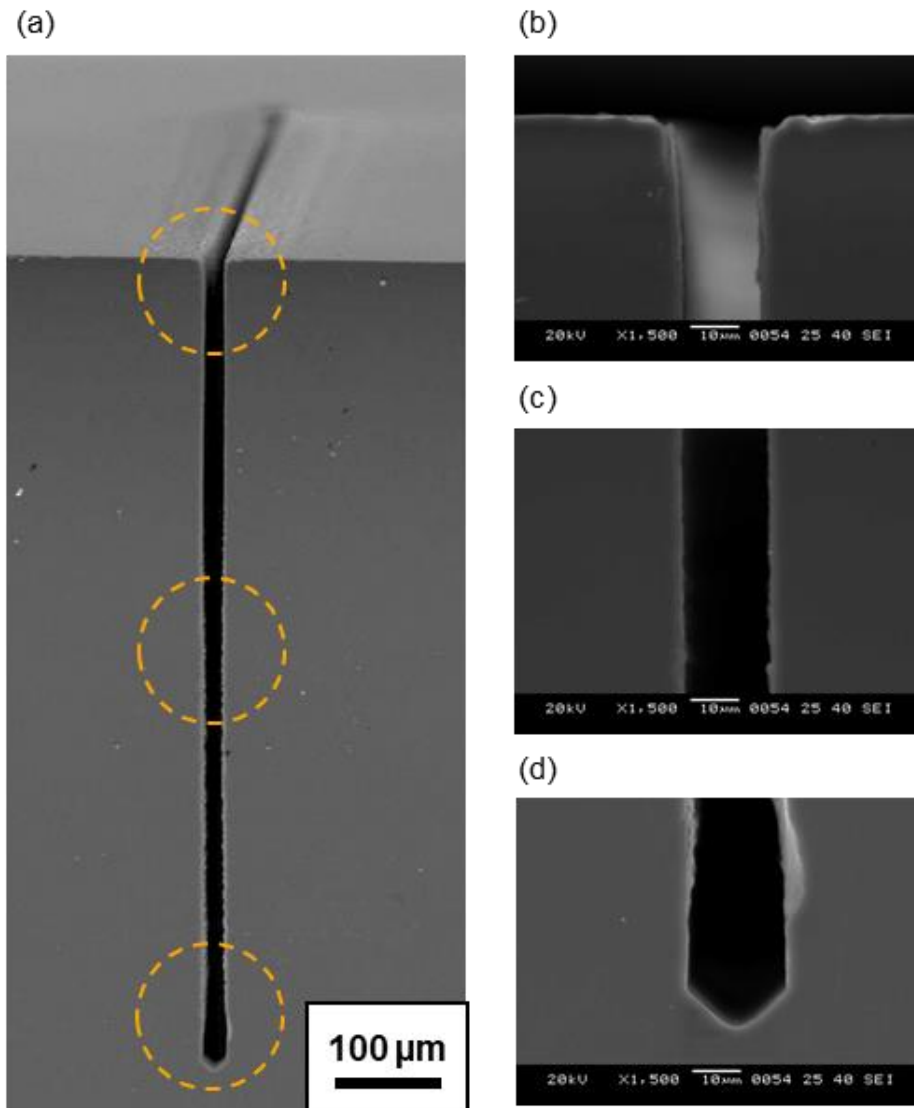


**Fig. 3.6 High aspect ratio channel fabricated in absorbent with added phosphoric acid (60 wt%). (a) overall cross-section of a channel (b) magnified view at the top (c) 320 μm from top (d) 640 μm from top.**

As with the process using the copper sulfate absorbent, the fabrication process using the absorbent with phosphoric acid could be separated into three steps: initial state, vapor-layer generation state, and crack generation state. In the first moment of the initial state (Fig. 3.7a-1), bubbles were generated at the laser irradiation point and collapsed, as in the initial state of the process using the copper sulfur absorbent. This initial state continued, although bubbles were generated inside the channel (Fig. 3.7a-2). Unlike the case for the copper sulfate absorbent, laser irradiation of the remaining bubble did not initiate aggressive copper oxide adhesion and flash. As a result, the process could be continued without generating cracks. According to the elemental analysis results (Fig. 3.8a), copper was not detected on the processed surface, although the laser irradiated the bubbles.

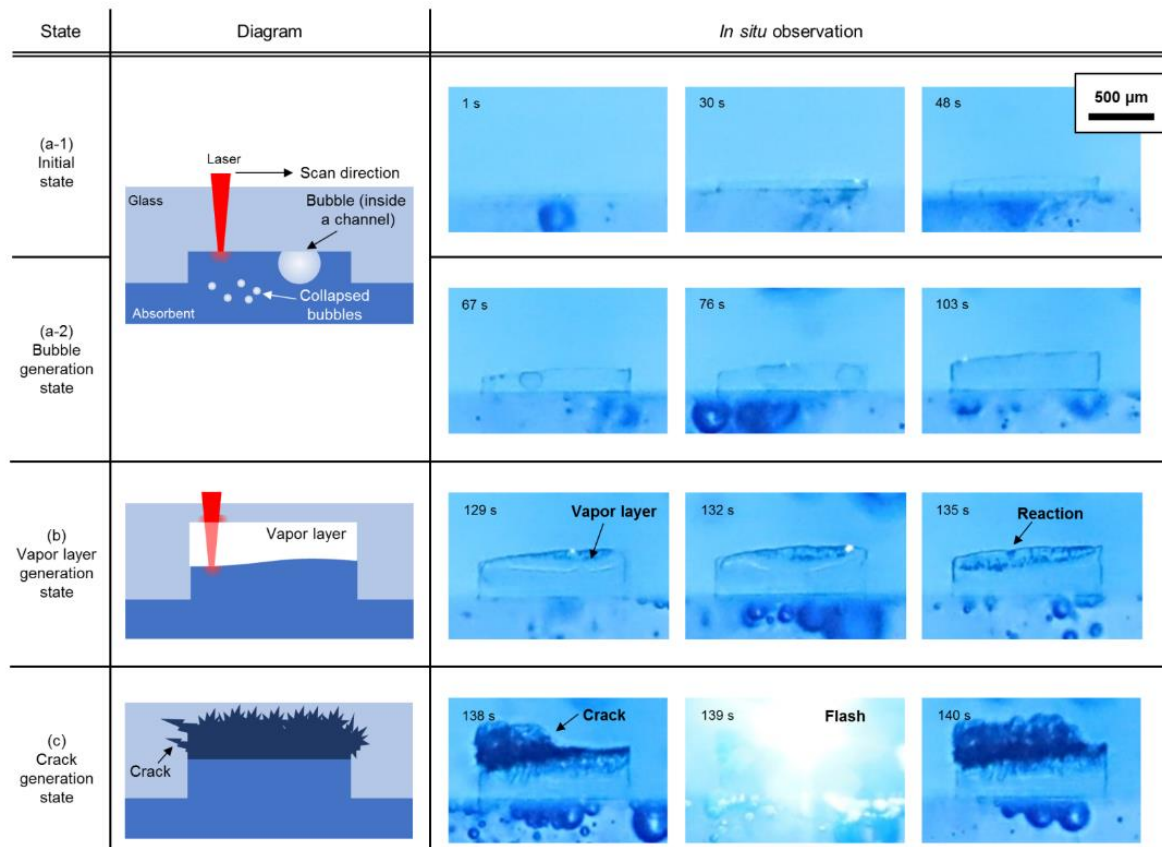


**Fig. 3.7** Diagrams and *in situ* observations of the LIBWE milling process in absorbent with added phosphoric acid: (a) initial state, (b) vapor layer generation state, and (c) crack generation state.

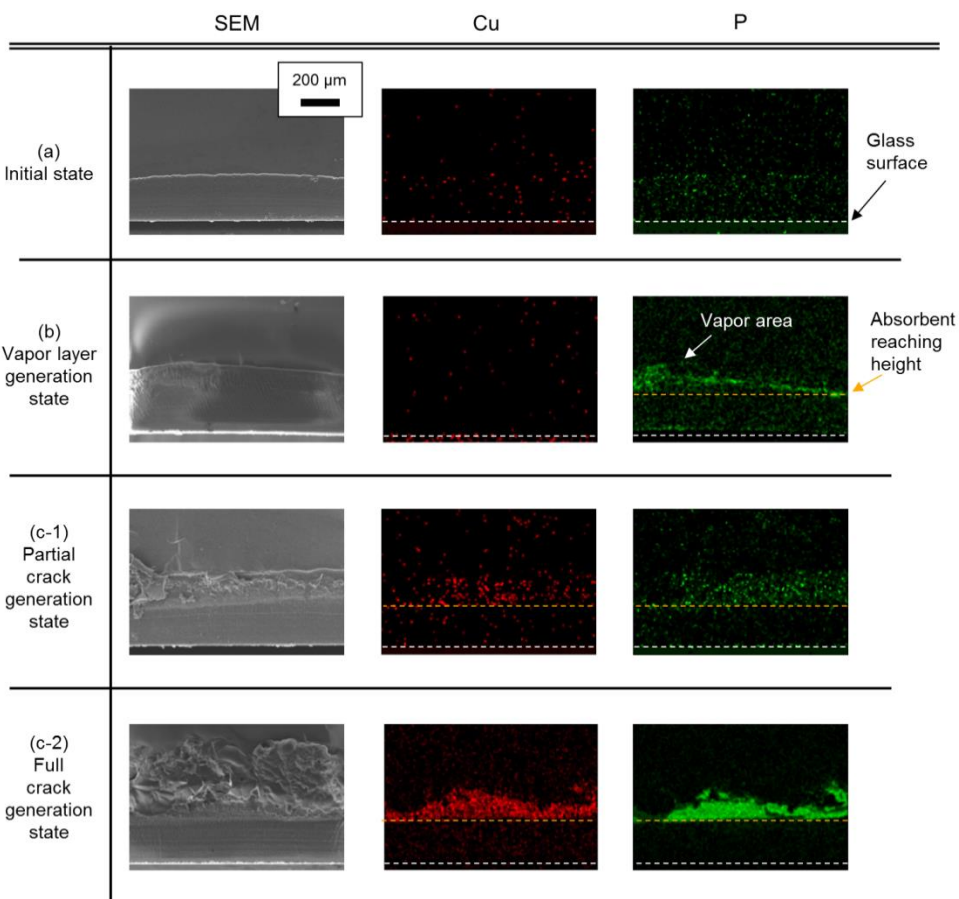


**Fig. 3.8 SEM image and elemental analysis of a sidewall machined in absorbent with added phosphoric acid: (a) initial state, (b) vapor layer generation state, and (c) crack generation state. Red dots are detected copper element and green dots are detected phosphorus element.**

In the LIBWE process using the absorbent with phosphoric acid, although the laser was irradiated a bubble or a vapor layer, aggressive copper oxide adhesion did not occur rapidly. This was due to the suppression of copper oxide adhesion by the silicon phosphate layer on the phosphoric acid-treated surface, which is depicted in Fig. 3.9. A surface coating on glass can hinder the adhesion of copper because the coating gives copper no opportunity to bond with surface molecules during the LIBWE process, thus affecting the fabrication process [36].

Because the phosphoric acid reaction temperature (200°C) was lower than the thermal decomposition temperature (600°C), generation of the silicon phosphate layer was initiated prior to the copper oxide adhesion. This adhesion sequence could also be explained by X-ray photoelectron spectroscopy (XPS) of machined surfaces fabricated using different absorbents, as depicted in Fig. 3.10. Using the data for the copper sulfate absorbent, deposition of copper (II) oxide could be investigated with the satellite at a binding energy of around 940 eV to 945 eV. Based on previous studies this satellite only appeared when a compound of  $\text{Cu}^{2+}$  existed. Also, the peak around 932 eV was separated into two peaks, and the peak with the lower binding energy had a higher value. From this result, the existence of  $\text{Cu}^+$  was identified, generated from copper (I) oxide. Signal intensity from a

copper compound weakened when the surface was machined using the phosphoric acid-added absorbent compared to signal intensity when using the copper sulfate absorbent. The existence of phosphate materials was identified from the XPS results at a binding energy of around 135 eV [37]. This signal did not appear in the results for the copper sulfate. From these results, it was possible to establish that copper oxide deposition was hindered when the LIBWE process included phosphoric acid-added absorbent.

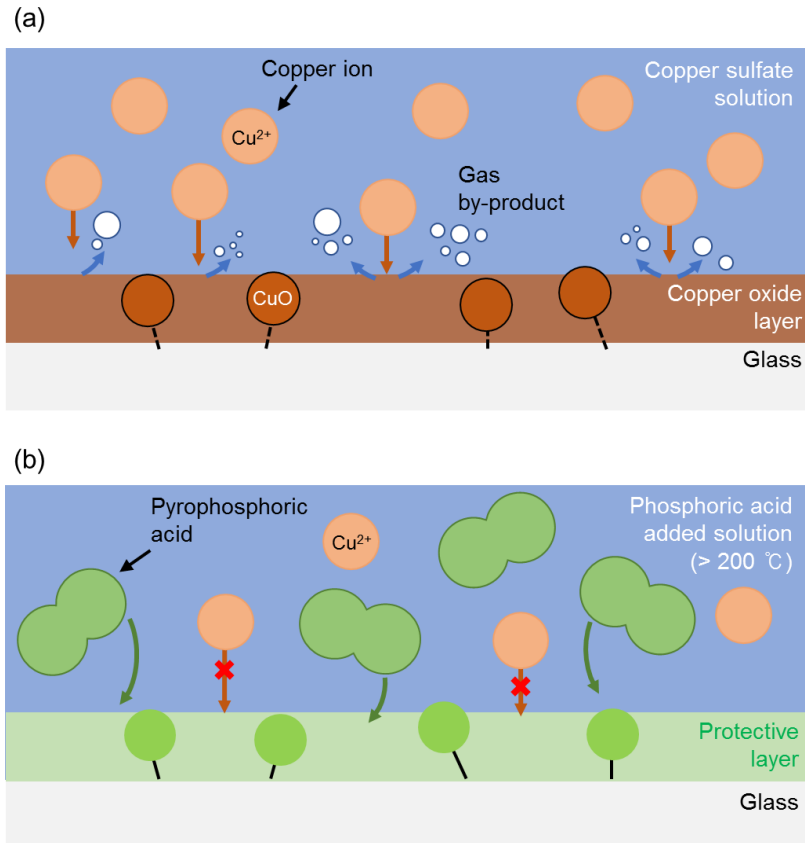


**Fig. 3.9 Glass surface reactions during the LIBWE process: (a) in copper sulfate solution and (b) in solution with added phosphoric acid.**

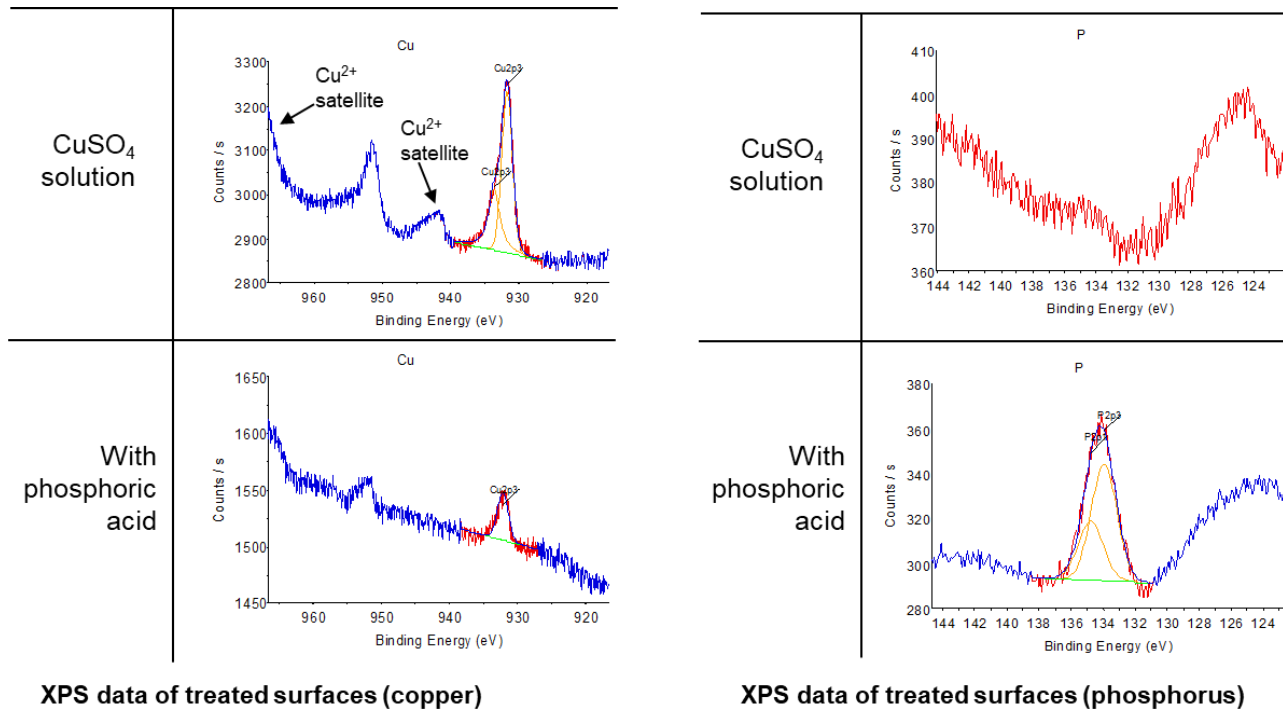
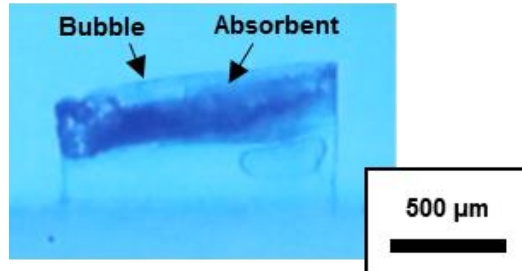


Fig. 3.10 XPS data of phosphorus and copper on machined surface in different absorbent



In the next step, a vapor layer was trapped in the channel and remained until crack generation (Fig. 3.7b). Since the liquid absorbent could not pass through the vapor layer, the cooling effect of the liquid absorbent was inhibited. This cooling-inhibited environment made the thermal decomposition of the copper sulfate and the etching of the phosphoric acid easier to initiate. The elemental analysis results for the vapor-layer generation state (Fig. 3.8b) showed that the silicon phosphate generation was aggressively activated inside the vapor layer. Because the reaction between phosphoric acid and glass can be activated in a high-temperature environment, the silicon phosphate generation process did not actively proceed when the temperature was rapidly reduced by the liquid absorbent.

A vapor layer was created because gas by-products produced by thermal decomposition could not escape from the deep channel. This vapor-layer generation principle was supported by the vapor and liquid absorbent state after the laser irradiation ended. As depicted in Fig. 3.11, the liquid absorbent reached the top of the channel by capillary action without any external force. The existing vapor layer shrank due to the temperature decrease, but was not eliminated. This showed that the vapor layer was created not only by evaporation and thermal expansion, but also by the additional gas by-products.



**Fig. 3.11 Vapor and absorbent states after the fabrication process was completed.**

The LIBWE process could also proceed in the vapor layer, although the liquid absorbent was not in contact with the machined spot. The mechanism of the non-contact LIBWE process was explained by laser irradiation on the glass and absorbent which were not in contact. Fig. 3.12 depicts glass surfaces drilled using the non-contact LIBWE process. The process could proceed because the liquid absorbent still evaporated and exploded at the laser irradiation spot. This explosion caused the liquid absorbent to splash, and if the gap between the absorbent and glass was close enough, it stained the glass. This staining liquid acted as an absorbent, so the process could proceed. Additionally, certain characteristics of the liquid absorbent were still effective, although the amount of staining liquid was small. Dimples machined using the copper sulfate absorbent showed initial cracks, but no initial cracks appeared in dimples machined using the phosphoric acid absorbent.

Aggressive copper oxide adhesion and crack generation were initiated following the silicon phosphate protective-layer generation process (Fig. 3.8c-1). After a partial crack was generated, the crack propagated with a bright flash created by the laser irradiation of the copper oxide (Fig. 3.7c). Continuous heat absorption caused heat accumulation in the vapor layer, which resulted in thermal decomposition of the copper sulfate, not only at the laser irradiation site but in all the vapor areas. Deposited copper oxide excessively absorbed the laser energy and imposed thermal stress on the processing area. As the irradiation proceeded, other cracks propagated from the first crack. In the cracked area, few or no phosphorus and copper elements were detected in the elemental analysis results (Fig. 3.8c-2). Because the excessive heat absorption around the copper oxide generated high thermal stress, the explosion tore off the glass substrate with copper oxide and silicon phosphate.

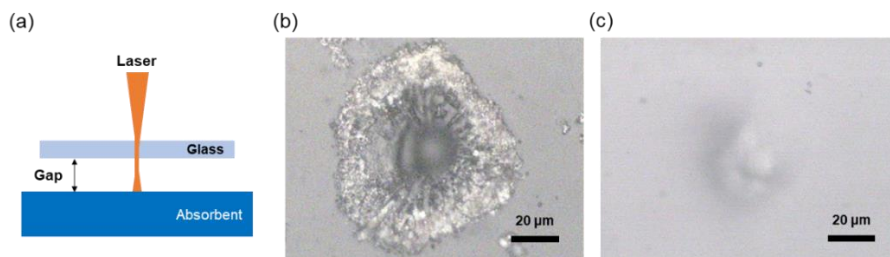


**Fig. 3.12. Dimples machined with non-contact liquid absorbent. (a) machining diagram, (b) dimple machined with copper sulfate absorbent, (c) dimple machined with phosphoric acid added absorbent**

# **Chapter 4**

## **Machining Characteristics of LIBWE using a Phosphoric Acid-Added Absorbent**

This chapter explains the machining characteristics of LIBWE using the phosphoric acid-added absorbent, based on the experimental results and theoretical background. It first explains the major characteristics due to phosphoric acid concentration changes affecting the maximum aspect ratio, sidewall roughness, and fabrication speed. It then explains characteristics mainly influenced by conventional LIBWE parameters (copper sulfate concentrations, laser power, laser scanning speed, and number of scans) based on the absorbed energy indexes described in section 2.3.

## **4.1. Effect of Phosphoric Acid Concentration**

This section discusses the influence of phosphoric acid concentrations on the maximum depth, fabrication speed, and sidewall roughness of a channel, mainly explained by the protective layer and its effect.

### **4.1.1. Maximum aspect ratio**

The maximum fabricable depth due to phosphoric acid concentrations and other parameters is illustrated in Fig. 4.1. In all cases, the width of the channel remained between 20  $\mu\text{m}$  and 24  $\mu\text{m}$ , so the aspect ratio of the channel was mainly affected by the depth. Fig. 4.2 shows that the maximum fabricable depth of a channel varied according to changes in the phosphoric acid concentration. As the concentration of phosphoric acid increased, the processable depth (Fig. 4.2a) also increased from 103  $\mu\text{m}$  (0 *wt%*) to 530  $\mu\text{m}$  (40 *wt%*). Cracks were generated when the laser irradiated the channel after its processable depth was reached (Fig. 4.2b). The phosphoric acid concentration positively correlated with the amount of pyrophosphoric acid: the higher the amount of pyrophosphoric acid, the more phosphate layers were formed, which suppressed the adsorption of copper oxide. As a result,

excessive copper oxide deposition and crack generation were suppressed. The duration of the vapor layer state was measured with *in situ* observations to determine the vapor layer's ability to suppress excessive copper oxide adhesion (Fig. 4.3). The average duration of the vapor layer increased as the phosphoric acid concentration increased, because the protective layer that could support the expansion at the maximum fabricable depth built up through the suppression of excessive copper oxide deposition.

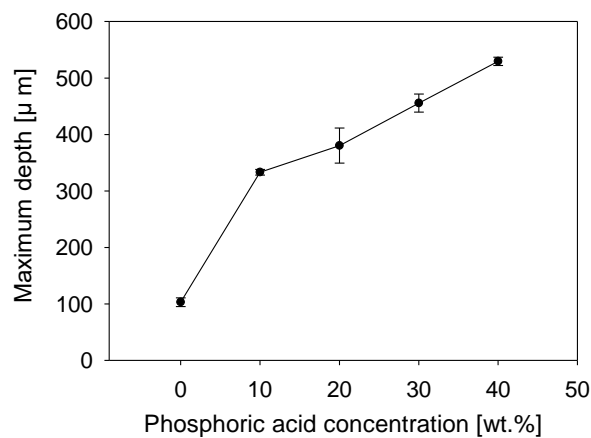


**Fig. 4.1 Maximum fabricable depth according to changes in the following phosphoric acid concentration.**

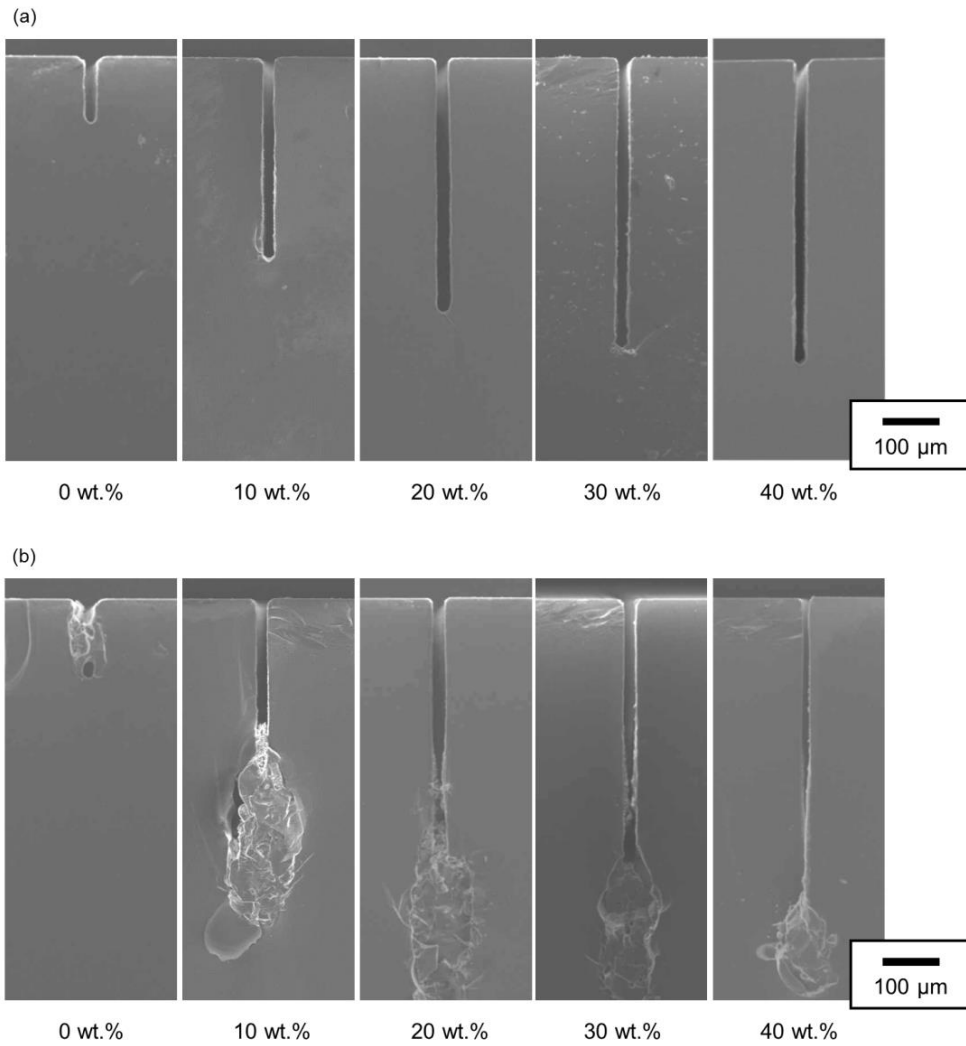


**Fig. 4.2 Fabricated channel with different phosphoric acid concentrations: (a) maximum fabricable depth and (b) crack generation.**

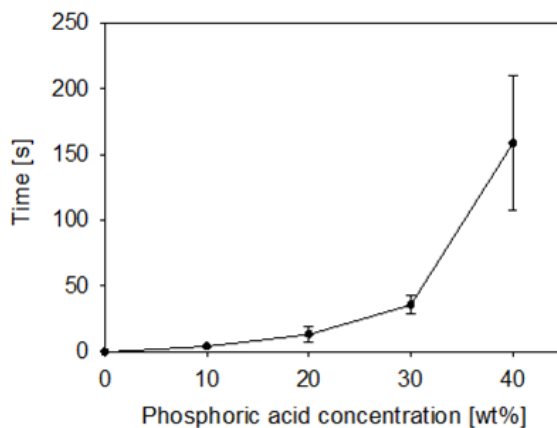


**Fig. 4.3 Duration of vapor layer until crack generation due to phosphoric acid change from 0 wt% to 40 wt%.**

The crack suppression mechanism owing to the reaction between phosphoric acid and glass was also supported by the results for other parameters. Changes in the copper ion concentration, laser power, and scanning speed had little effect on the generation of a silicon phosphate protective layer (Fig. 4.4). As a result, maximum depth showed little variation as a function of changes in the copper sulfate concentration, laser power, and scanning speed. The amount of copper sulfate did not affect the maximum fabricable depth because the reaction between phosphoric acid and the glass substrate occurred prior to the copper oxide adhesion process. Decomposed copper oxide was able to attach to the remaining surface, so the amount of silicon phosphate was more important for the crack generation delay. The



increase in laser power may have resulted in acceleration of heat accumulation, which was critical for excessive thermal decomposition and copper oxide adhesion. However, because the fabrication speed also increased, processable depth could be maintained even though the time until the crack occurred was reduced. Based on derived equations (3) and (5), scanning speed changes mainly affected the absorbed energy density at a single spot, which, in turn, mainly affected the environment at the laser irradiation site, rather than the whole energy absorption rate. The detected copper element across the entire vapor area showed that copper oxide adhesion did not occur mainly at the laser irradiation spot; hence, scanning speed changes had little or no effect on the chemical reaction that was critical to crack generation, so the maximum fabricable depth remained at a similar value.

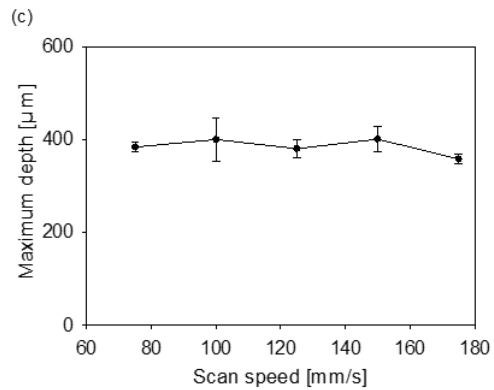
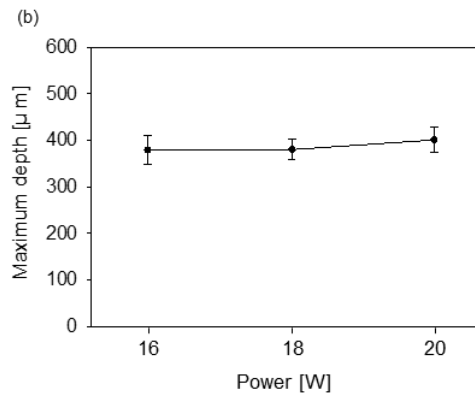
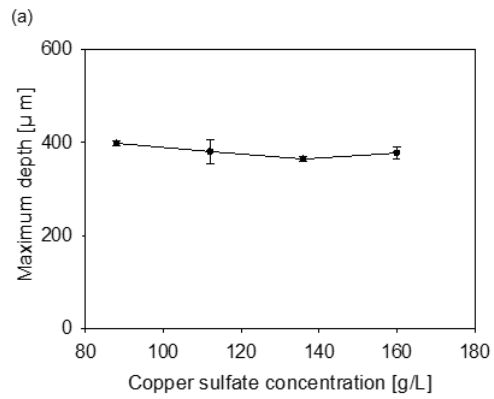


**Fig. 4.4 Maximum depth as the parameter changes:**  
**(a) copper sulfate concentration, (b) laser power, and (c) scan speed.**

## 4.1.2. Sidewall roughness

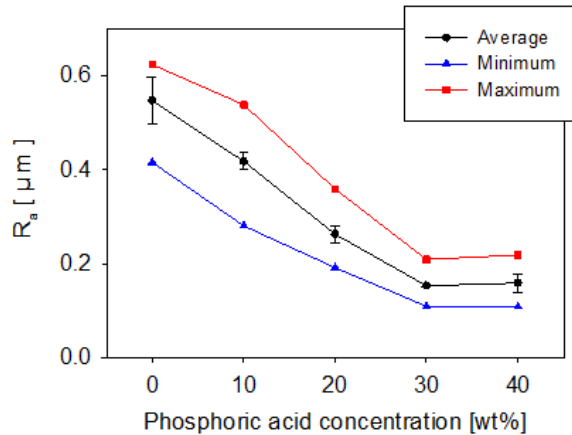


**Fig. 4.5 Average surface roughness ( $R_a$ ) changes according to the phosphoric acid concentration.**

Figures 4.5 and 4.6 show the average surface roughness ( $R_a$ ) of the channel's sidewall as the phosphoric acid concentration changed. The  $R_a$  decreased from  $0.55 \mu\text{m}$  ( $0 \text{ wt}\%$ ) to  $0.16 \mu\text{m}$  ( $30 \text{ wt}\%$ ) and maintained similar roughness, despite the phosphoric acid concentration being increased to  $40 \text{ wt}\%$ . As shown in Fig. 4.6a, an increase in phosphoric acid concentration resulted in a maximum depth increase, so the total area of the sidewall had to be widened.

As shown in Figures 4.5 and 4.6b, the sidewall roughness decreased as the phosphoric acid concentration increased. This  $R_a$  improvement could be explained by the silicon phosphate protective layer. It is known that a high energy input at a single point creates larger peaks and valleys, which result in high sidewall surface roughness [38]. The silicon phosphate protective layer decreases the amount of energy absorption and minimizes the peaks and valleys of the sidewall. This can be seen in the magnified sidewall images in Fig. 4.6b. Because of the high energy input, melted and resolidified shapes remained on the surface when phosphoric acid was not added. These resolidified shapes rarely existed on the sidewall machined with a 10 wt% phosphoric acid concentration, and were eliminated on the sidewall machined with a 40 wt% concentration, because of the increase of the generated silicon phosphate protective layer. The variation in surface roughness was supported by the existence of a bubble or vapor layer. Additional heat energy inside a bubble or a vapor layer caused the channel sidewall to be machined with intense power, resulting in an increase in surface roughness.

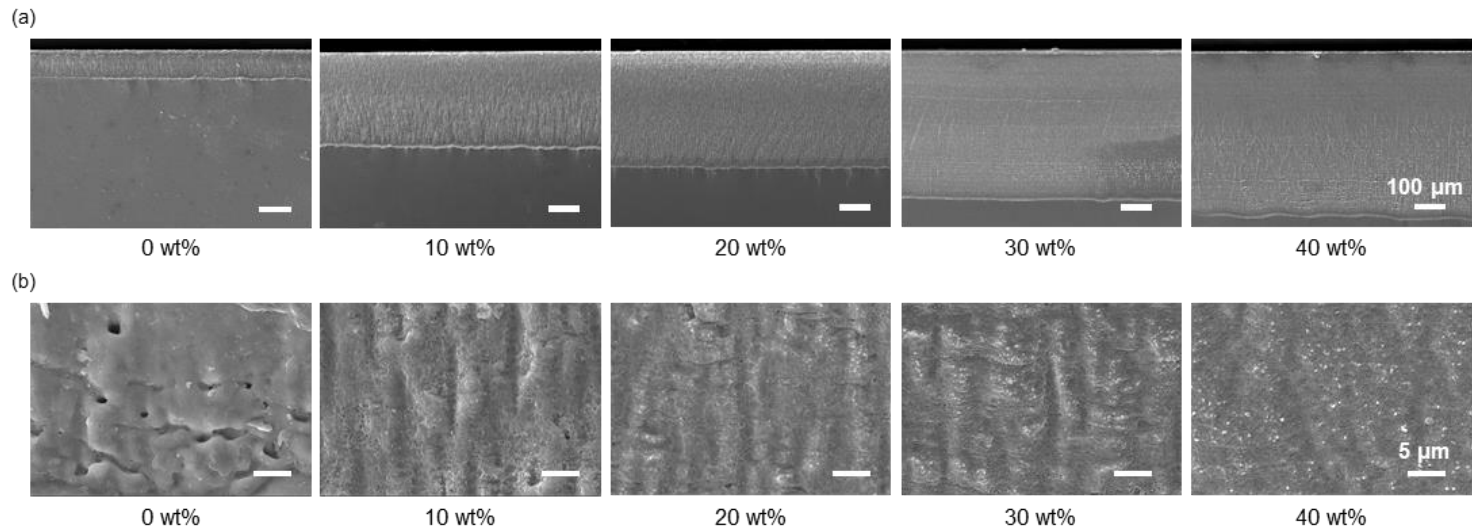


**Fig. 4.6 Average surface roughness ( $R_a$ ) changes according to the phosphoric acid concentration (a) the overall shape of the sidewall, and (b) magnified images of the sidewalls.**

### 4.1.3. Fabrication speed

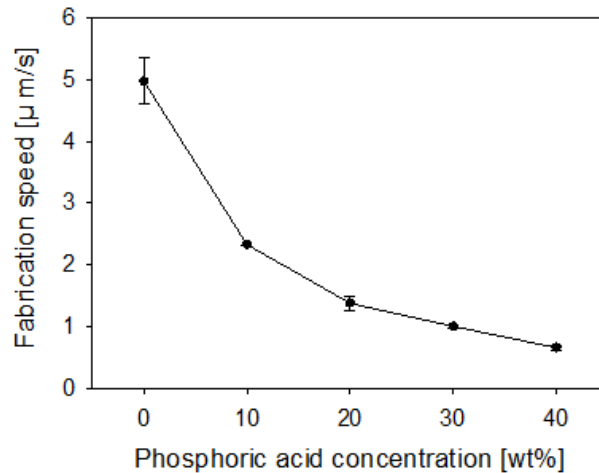


**Fig. 4.7 Fabrication speed according to phosphoric acid concentration change.**

Fig. 4.7 depicts fabrication speed changes due to changes in the phosphoric acid concentration. Fabrication speed decreased as the phosphoric acid concentration increased, which could be explained by the average absorbed power density. The increase in the phosphoric acid concentration provided more chance of a silicon phosphate protective layer being generated on the surface, which hindered the adhesion of copper oxide. As depicted in Fig. 4.8, the phosphorus-detected area enlarged as the concentration of the phosphoric acid increased. Decreases in adsorbed copper oxide due to the silicon phosphate layer resulted in a decrease in energy absorption efficiency on the

machining surface, which could also be explained by a decrease in the absorption coefficient in Equation (6). Consequently, the fabrication speed decreased as the phosphoric acid increased.

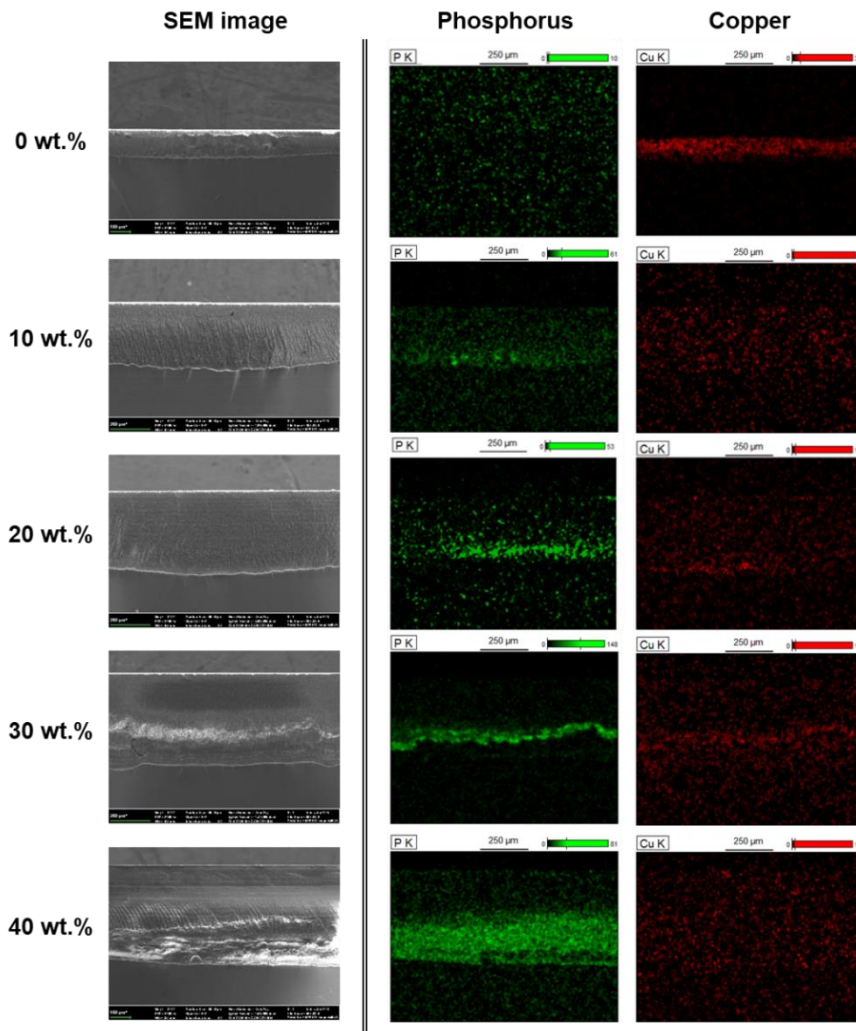


**Fig. 4.8 Sidewall image and elemental distribution compared to the phosphoric acid concentration.**

## **4.2. Effect of Parameters except Phosphoric Acid Concentration**

This section discusses the changes in machining characteristics corresponding to the major machining parameters except the phosphoric acid concentration (laser power, scanning speed, copper sulfate concentration, and number of scans) and explains them based on the derived equations in section 2.3 and previous studies. The fabrication speed and machinability of a glass substrate were mainly explained by the laser energy indexes (single point energy density and average absorbed power density), and channel depth change trends were compared with the number of scans for different phosphoric acid concentrations and laser powers.

### **4.2.1. Fabrication speed**

The fabrication speed as the machining parameters changed was measured and compared with the calculated absorbed power density. Overall, the fabrication speed for each experiment matched well with the average absorbed power density, as depicted in Fig. 4.9.



Based on Equation (6), the average absorbed power density was directly proportional to the peak pulse power ( $P$ ) and liquid absorption coefficient ( $\alpha$ ). As a result, the fabrication speed trend linearly increased as the laser power increased, also following the trend of the absorption coefficient. However, fabrication speed was not affected by scanning speed, either theoretically or experimentally (Fig. 4.9c). Based on equation (5), scanning speed did not affect the average power density. This was because the decrease in irradiation across a unit length as the scanning speed increased was canceled out by the increase in the net irradiation time. As a result, the fabrication speed was not affected by scanning speed changes and stayed at the same value.

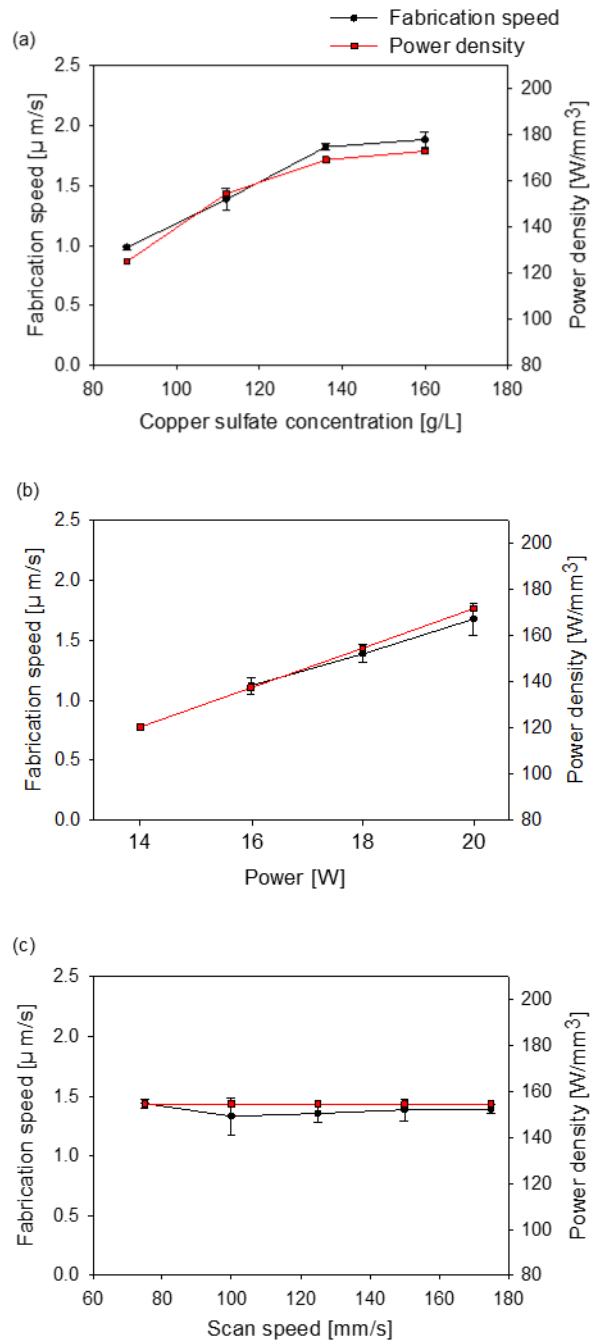


**Fig. 4.9 Fabrication speed according to parameters change: (a) copper sulfate concentration, (b) laser power, and (c) laser scan speed.**

## 4.2.2. Machinability

Based on the experiments, the machinability of a glass substrate was determined by the absorbed energy density at a single point. This could be explained by the temperature trend at a certain irradiated point. From the perspective of a single point, the net irradiation time was much shorter than the resting time. The temperature at the point increased rapidly during laser irradiation, but also decreased rapidly and remained at a low temperature [31]. Because the temperature at the point was determined by the absorbed energy in the irradiation moment, it was appropriate to explain the machinability according to the absorbed energy density at a single point.

The glass substrate could be machined when the absorbed energy density was greater than a certain value ( $1.4 \text{ J/mm}^3$ ), which was experimentally determined as the threshold energy density. This matched the result for the absorbed energy power at a copper sulfate concentration of  $64 \text{ g/L}$  ( $1.05 \text{ J/mm}^3$ ), a laser power of  $14 \text{ W}$  ( $1.38 \text{ J/mm}^3$ ), and a laser scanning speed of  $200 \text{ mm/s}$  ( $1.37 \text{ J/mm}^3$ ).

Also, when the absorbed energy density at a single point was too large, instant cracks occurred on the glass substrate. When the scanning speed was

slower than 50 mm/s, instant cracks occurred during laser irradiation due to a rapid increase in the absorbed energy density ( $5.39 \text{ J/mm}^3$ ).

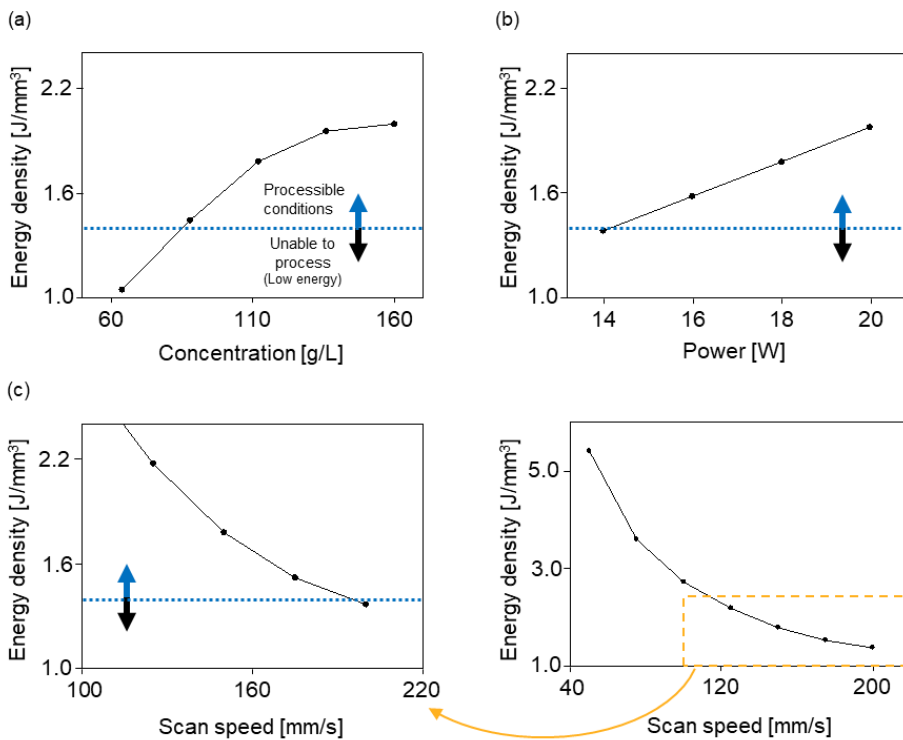


**Fig. 4.10 Absorbed energy density at a single point according to parameter changes. Absorbed energy density and processability are compared: (a) copper sulfate concentration, (b) laser power, and (c) laser scan speed.**

### 4.2.3. Depth of a channel

As with other laser beam machining processes, the number of scans greatly affects the final geometry of the workpiece. In LIBWE, the machined depth of a channel is linearly proportional to the number of scans [39]. As in previous studies, the machined depth of a channel linearly increased as the number of scans increased, as depicted in Fig. 4.12. This linearity was maintained until the machined depth reached 500  $\mu\text{m}$  for various phosphoric acid concentrations and laser intensities. This linearity could be explained by consistent laser intensity in the depth of the focus range and the liquid characteristics. In laser beam machining, the laser beam is supposed to be concentrated on a small spot, but because of limited beam concentration, the beam diameter remained almost constant when the distance from the focus was in the range of depth of focus (DOF), as depicted in Fig. 4.11 [40]. The DOF can be calculated as follows:

$$DOF = \left(\frac{8\lambda}{\pi}\right) \left(\frac{F}{D}\right)^2 \quad (7)$$

where  $\lambda$  is the wavelength of the laser beam, F is the focal length, and D is the input beam diameter. Based on Equation (7), because F was 160 mm and

D was 7.6 mm in our system, the depth of focus could be calculated as 1.2 mm. The actual possible deviation of focus could be half the DOF (600  $\mu\text{m}$ ). Based on this calculation, the machined channel depth was still in the DOF range, so the laser intensity remained constant.

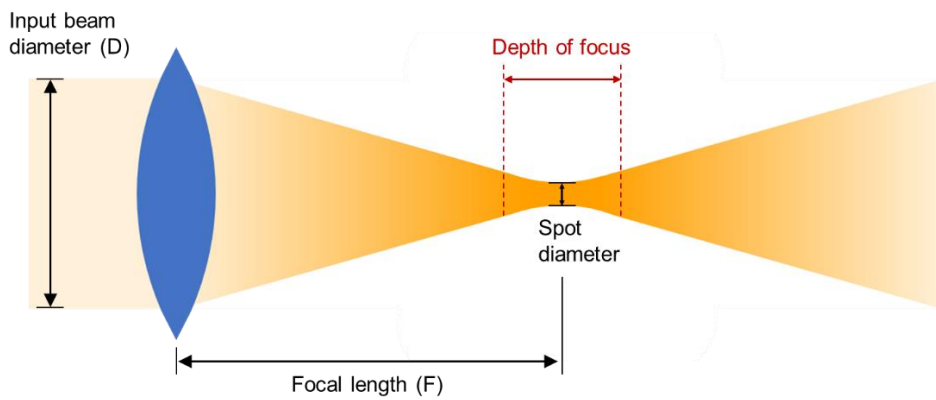


**Fig. 4.11 Schematic of laser beam and depth of focus.**

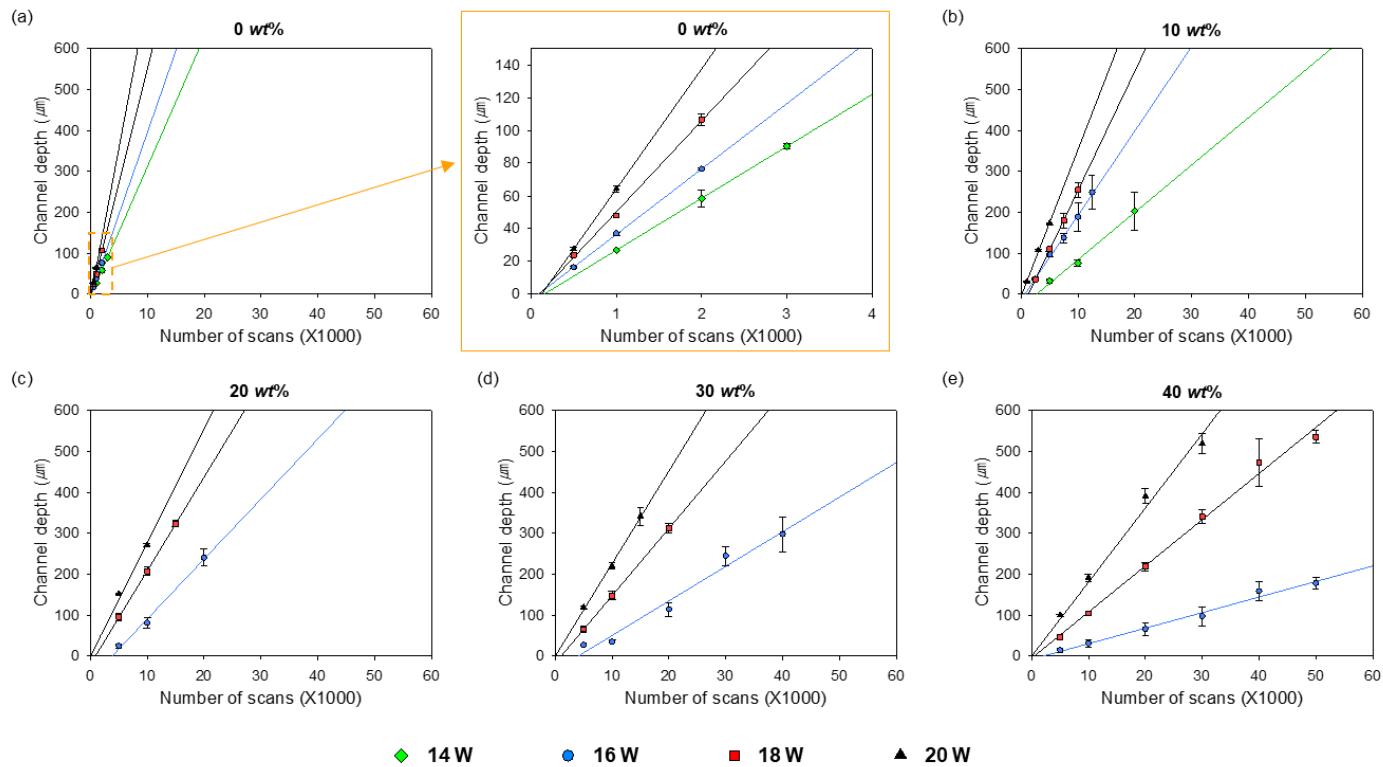


**Fig. 4.12 Machined channel depth compared to the number of scans in different phosphoric acid concentration (a) 0 wt%, (b) 10 wt%, (c) 20 wt%, (d) 30 wt%, (e) 40 wt%.**

#### **4.2.4. Various shapes of microchannels**

Various shapes of high-aspect-ratio microchannels were fabricated to determine the feasibility of the developed technique for industrial applications. First, a channel with increasing radius, from 0.4 mm to 2 mm, and multiple channels with ladder shapes were fabricated. Fig. 4.13 shows a diagram of the channels and the SEM images for the surface and the side section. In a channel with an increasing radius, it was possible to reach a depth of 471  $\mu\text{m}$  with low deviation (SD 8.6  $\mu\text{m}$ ) and 23  $\mu\text{m}$  width, like the single straight channel. Also, for ladder-shaped channels, high-aspect-ratio channels with 520  $\mu\text{m}$  depth (SD 4.2  $\mu\text{m}$ ) and 22  $\mu\text{m}$  width were fabricated. With these results, the processability of various radii of curvature channels, the uniformity of the channel for different scan lengths, and channel numbers were identified. These high-aspect-ratio glass microchannels could be utilized for specific applications such as cell separation and self-driven capillary flow generation.



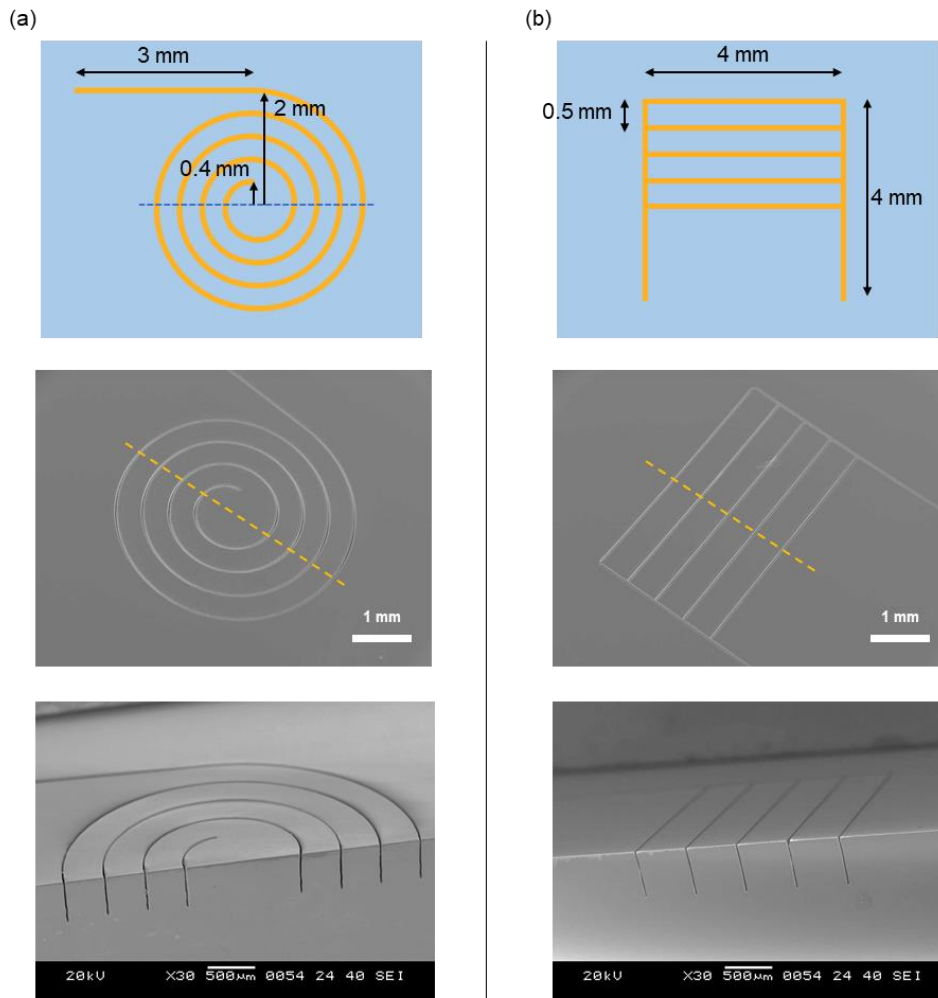


**Fig. 4.13 Diagram and SEM images of channels with various shapes: (a) circular channel with increasing radius and (b) ladder-shaped multiple channels.**

# Chapter 5

## Fabrication of 3D Microstructures

This chapter discusses a proposed scan path generation process for minimizing shape errors due to the LIBWE principle and explains its application to the machining of various glass microstructures. Shape errors that occurred using conventional scan paths were observed, and the causes were explained by LIBWE principles. To avoid these shape errors, a random-point scan path and a random-line scan path were proposed, and the characteristics of the proposed scan paths were investigated. Finally, various glass microstructures were machined using the proposed scan paths to validate their applicability to various structures, and the precision of the scan paths was observed by comparing the profiles of the generated scan distributions and machined pockets.

## 5.1. Conventional Scan Paths

Laser beam machining for fabricating 3D structures uses various scan paths, including raster scan paths, reciprocating scan paths, spiral scan paths, and random scan paths. These basic conventional scan paths were applied to fabricate a simple square glass micropocket. Square glass micropockets were fabricated using the LIBWE process and conventional scanning to observe the performance of conventional scan paths. The machining conditions are shown in Table 5.1, and basic scan paths are shown in Fig. 5.1. The machining results according to the number of scan changes were observed. The intervals between grids for positioning the initial and final points of each scan line were set at the same value as the resolution of the current laser scanning system, which was 2  $\mu\text{m}$ .

**Table 5.1**

**Experimental condition for square micro pocket machining**

Parameter	Value
Power	20 W
Frequency	50 kHz
Scan speed	150 mm/s
Absorbent	H <sub>3</sub> PO <sub>4</sub> 40 wt% + CuSO <sub>4</sub> 0.7M
Width & length	600 μm
Grid interval	2 μm
Machining time	500, 1000, 1500, 2000 s (raster, reciprocating, random) 250, 500, 750 (spiral)

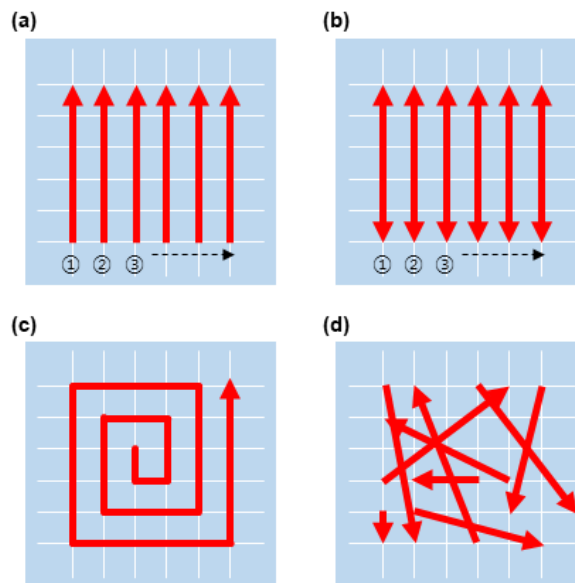


**Fig. 5.1 Conventional scan paths for comparison: (a) raster, (b) reciprocating, (c) spiral, and (d) random.**

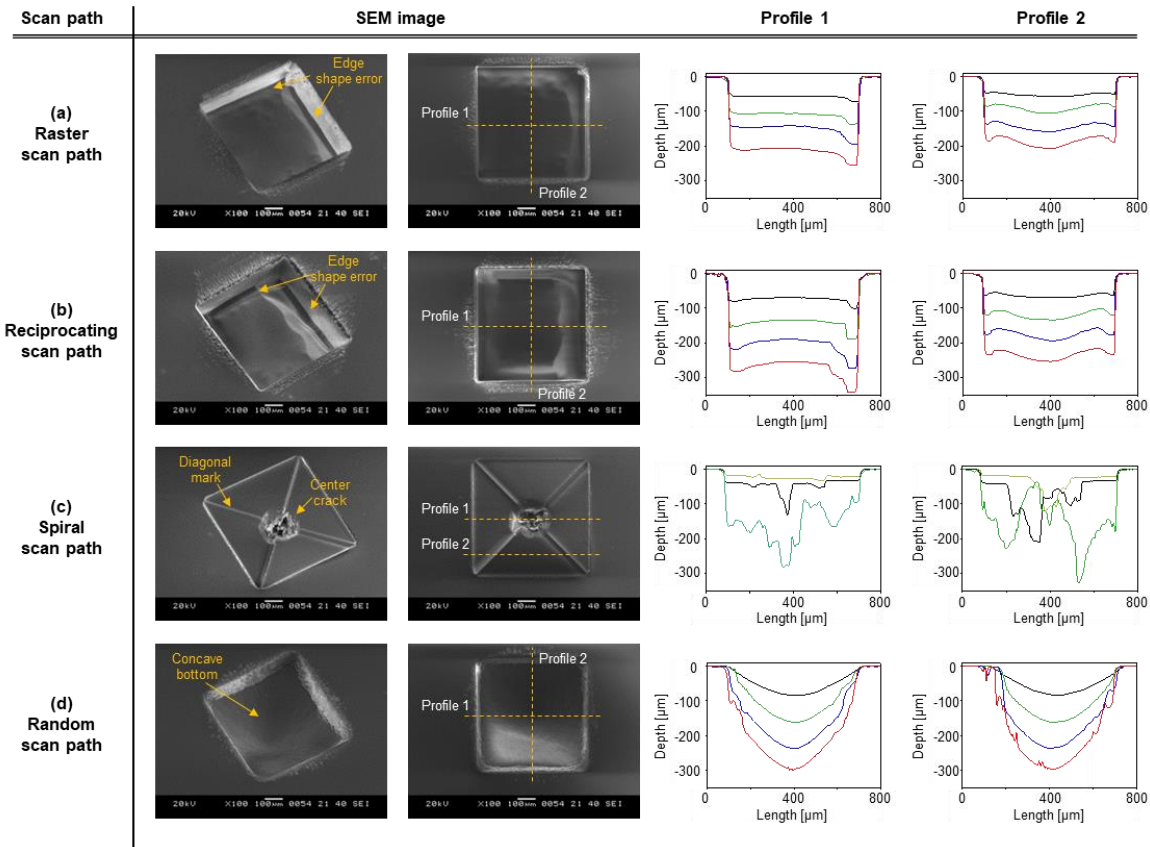


**Fig. 5.2 SEM images and profiles of machined glass micro pockets fabricated with (a) raster path (b) reciprocating path (c) spiral path (d) random path. Profiles of (a), (b), and (d) were results observed from micropockets machined every 500 seconds, and profiles of (c) were results observed every 250 seconds.**

As depicted in Fig. 5.2a, square micropockets were machined with a raster scan path, reciprocating scan path, spiral scan path, and random scan path, and the results were observed and compared. The raster scan path had a one-directional move of the laser scanning point, which resulted in numerous initial and final point overlaps and additional machining at the end of the scan path. This additional machining could be explained by the bubble accumulation in the machining process, which was observed *in situ* and is depicted in Fig. 5.3. As the laser scanned along a certain path, a bubble stuck to the laser irradiation point and moved simultaneously with the laser irradiation point. This bubble should have been flushed away by the turbulence inside the machining area; however, the bubble did not escape from the cavity when it was at the end of the machining area. This bubble caused additional heat accumulation inside the bubble because liquid absorbents that cool down the machining area cannot reach a inside the bubble during the process. This additional machining when the laser irradiated a bubble was reported and used to machine sapphire in a previous study, as depicted in Fig. 5.4 [41]. Additional machining at the end of the scan path occurred due to the heat accumulation inside the bubble. Because this additionally machined part was higher than the normal flat surface, bubbles started to accumulate continuously at the end of the scan path. As a result, the tip's depth and surface direction both increased, as shown in Fig. 5.3.

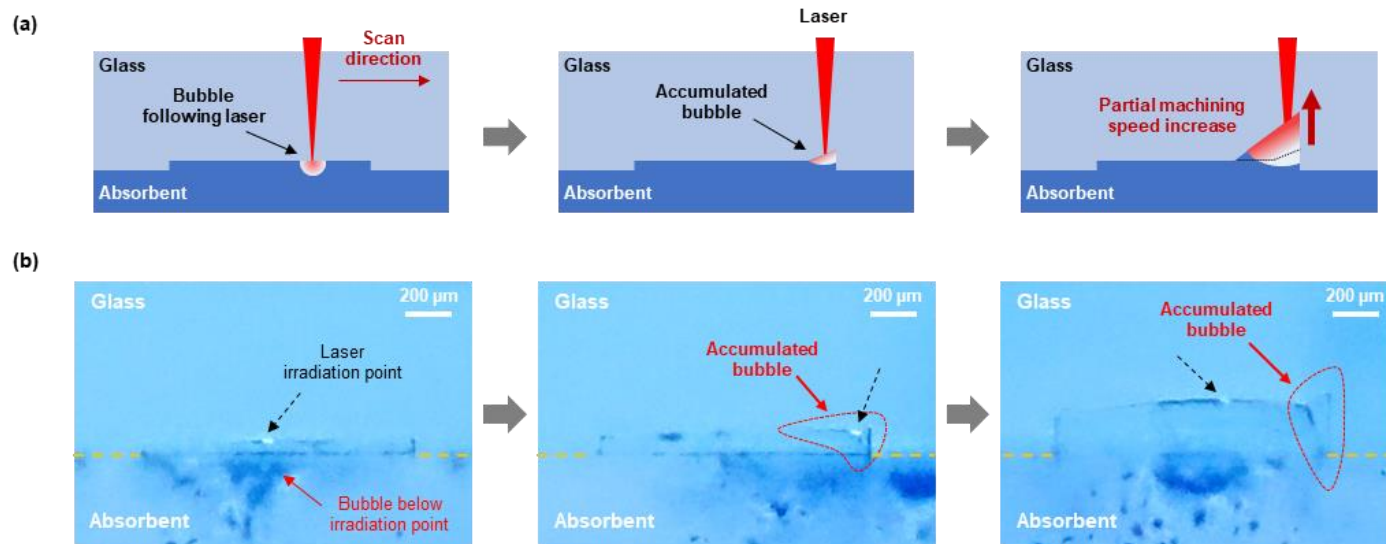


**Fig. 5.3** Diagrams and *in situ* observations for the micropocket machining process with bubble accumulation: (a) diagrams and (b) *in situ* observations.

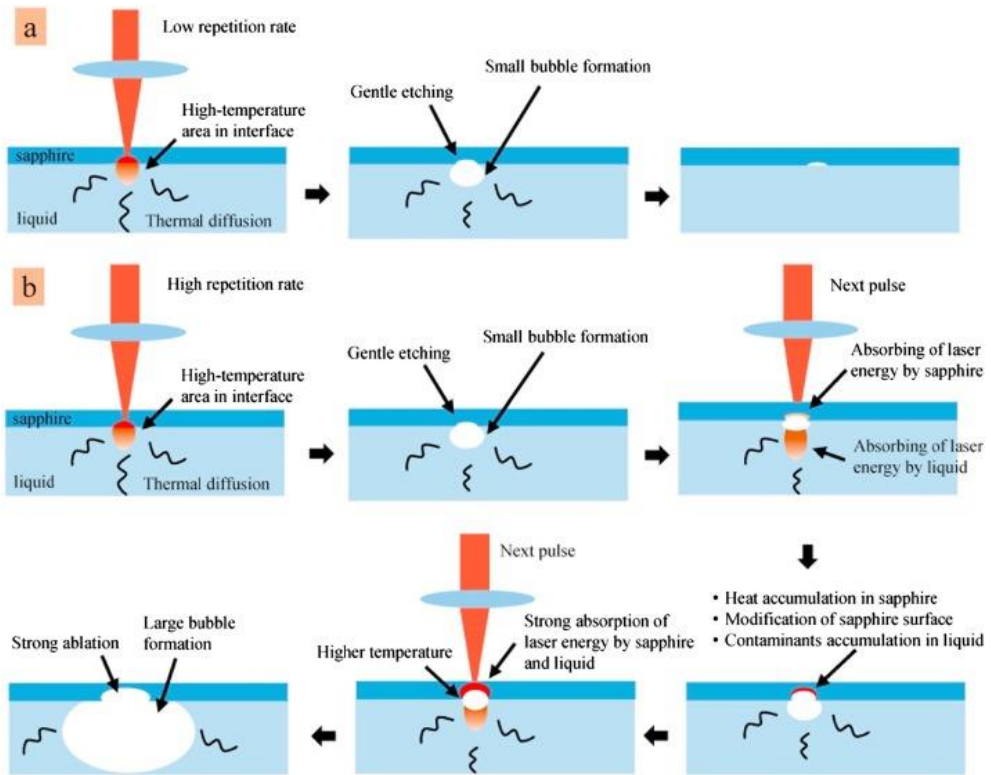


**Fig. 5.4. Additional machining during the LIBWE process, due to the additional laser irradiation and heat accumulation inside a bubble [41].**



Due to the additional heat absorption in the bubble, the square pocket formed by a raster scan path resulted in a shape error at the edge of the square (Fig. 5.2a). This shape error at the edge became deeper and wider as the machining time increased from 500 s to 2,000 s. Surface profile irregularities also appeared in a direction perpendicular to the scanning direction, as depicted in profile 2 of Fig. 5.2a. Due to the inertia of the galvanometer scanner, every change in the scanner's movement caused scanning speed changes. This shape error was created at the point where the characteristics of a constant scan path changed.

A reciprocating scan path has similar characteristics to a raster scan path, except that the scanning point returns to the starting point. As a result, the morphology of the square pocket fabricated with a reciprocating scan path showed similar results to the pocket using a raster scan path, such as further machining at the final point of the scan path, and surface profile irregularity in a direction perpendicular to the scanning direction (Fig. 5.2b). Due to the reduced scanning speed, additional machining also occurred on the edge where the scan path returned. This increased error made precision machining more difficult as the machining time increased.

Because a spiral path has only a single initial point and final point in the entire scan path, they overlap. Owing to this property, it was possible to

eliminate edge errors by preventing bubble accumulation at the final point (Fig. 5.2c). However, center cracks and shape errors in a diagonal direction occurred in the micropocket machined with a spiral path. Although the overall laser scan was evenly distributed, the partial laser irradiation density was irregular due to the difference in length of each scan line segment. The central area had excessive partial laser irradiation density due to the short duration between successive overlapping laser scans, which resulted in cracking. Additionally, a shape error occurred in a diagonal direction when the laser scanning point rotated vertically. This showed that the shape error occurred at the position where the speed decreased according to a change in the scanning direction.

As described in this section, if the scan path was constant, a geometry error occurred at a location where the scan path conditions (speed and direction) repeatedly changed. A pocket machined with a totally random scan path was also investigated to overcome the shape errors due to constant changes in scan path conditions. As shown in Fig. 5.2d, the subsequent machined pockets had no partial shape errors; however, the machined surface was concave. Since the number of lines passing by the point closest to the boundary was smaller than the number of lines passing by the point at the center, scan lines were less likely to reach the edges. The number of scans was concentrated in the

center and insufficient at the edges of the random scan paths (Fig. 5.5), resulting in a square pocket with a concave bottom. The curved shape remained when the machining time increased. To evenly distribute the laser irradiation, the scan lines needed to be further manipulated to eliminate shape errors.

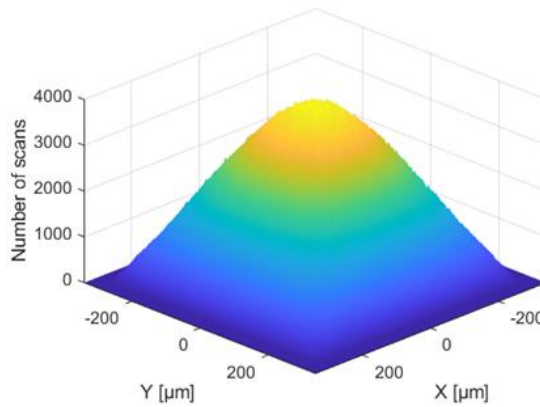


**Fig. 5.5 Number of scans distribution with random scan path**

## **5.2. Randomly Distributed Scan Path**

This section explains randomly distributed scan paths that were proposed for the LIBWE process to remove the shape errors in micropockets fabricated with conventional scan paths. Based on the results in section 5.1, scan paths, not only with the evenly distributed input energy, but also with random direction, were needed to remove the bubble-accumulation effect. Randomly distributed scan paths composed of points and lines (Fig. 5.6) were generated and their performance was experimentally tested. Random-point scan paths were first introduced, and various types of flat pockets and micropyramids were fabricated. Next, random-line scan paths were introduced, and possible strategies for developing appropriate scan paths were investigated through simulations and experiments. Finally, various structures that could be utilized for specific applications were fabricated.

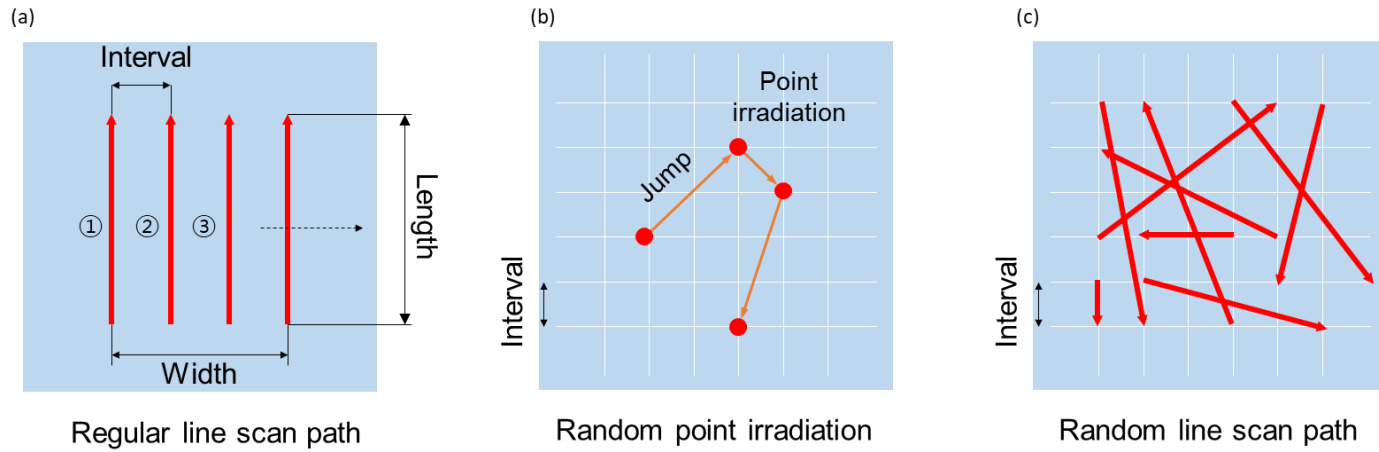


**Fig. 5.6 The idea of scan paths in this study.**  
**(a) conventional raster scan path, (b) random point scan path, and (c) random line scan path**

### **5.2.1. Random-point scan path**

A random-point scan path was used to fabricate a micropocket with less shape error. The random-point scan path-generation strategy could be separated into three steps, as depicted in Fig. 5.7: a target area setting, generation of points inside the target area, and mixing of point sequences. Because the laser control system set the position of the irradiation point as a discrete x–y coordinate, scan points needed to be in positions with discrete numbers; therefore, the target area was set on a discrete x–y plane, as depicted in Fig. 5.7a. Sequence numbers were then positioned for every point (Fig. 5.7b). If the scan path generation process stopped at this step, a point scan path with consecutive sequences was generated, which resulted in a pocket with additional shape errors. To prevent this problem, point sequences were shuffled to avoid directionality. The random-point scan path had some advantages because the scan path guaranteed the even distribution of laser energy and the directionless scanning area was well defined.

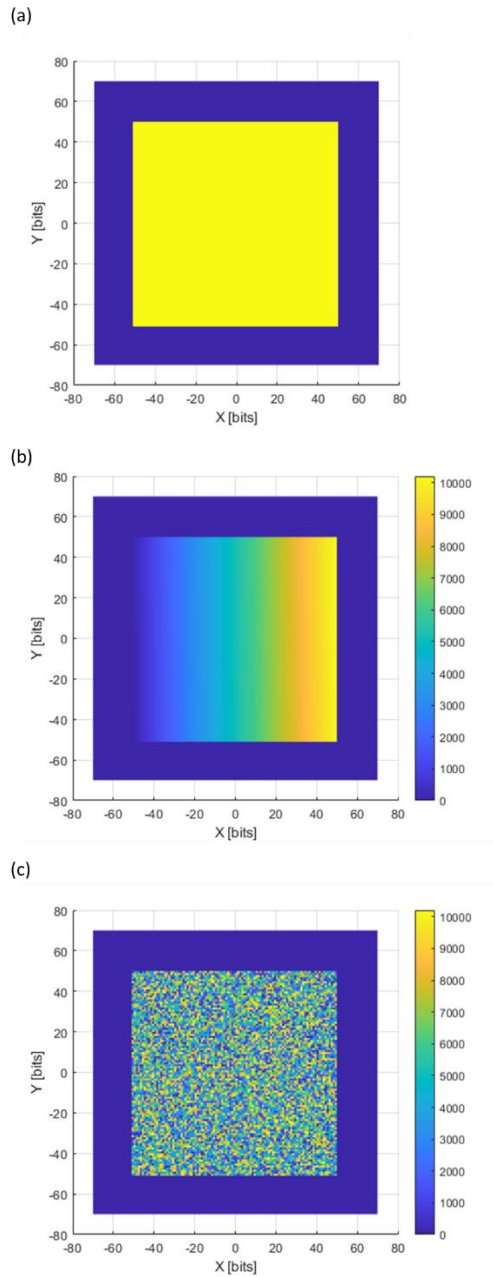


**Fig. 5.7** Sequence of random-point scan path generation (a) target area setting, (b) point sequence setting, and (c) the sequence of points mixing.

Based on the generated random-point scan path, machining of a square pocket proceeded with a different number of scans. The machining conditions are listed in Table 5.2. With the random-point scan path, because the scanner did not move during irradiation, the scanning speed was not a machining parameter, but the duration of laser irradiation acted as a major parameter. As depicted in Fig. 5.8, a square pocket with a flat bottom and untapered sidewall could be fabricated.

**Table. 5.2**  
**Machining condition for square micro pocket machining with random-point scan path**

Parameter	Value
Width & Height	200 $\mu\text{m}$
Point interval	5 $\mu\text{m}$
Power	20 W
Frequency	50 kHz
Duration of irradiation	200 $\mu\text{s}$
Absorbent	$\text{H}_3\text{PO}_4$ 40 wt% + $\text{CuSO}_4$ 0.7M
Process time	500 s



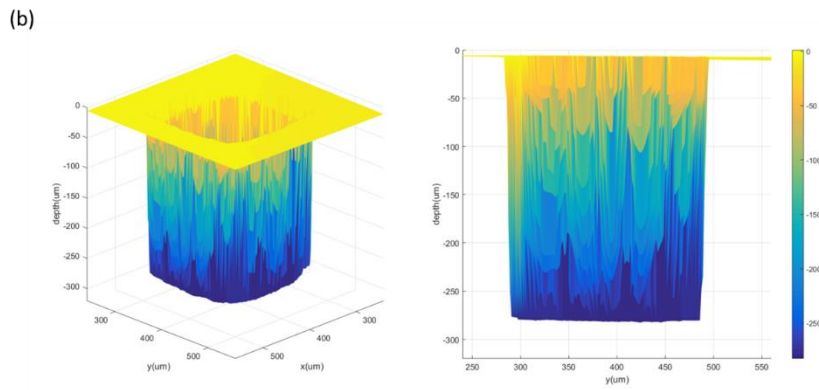
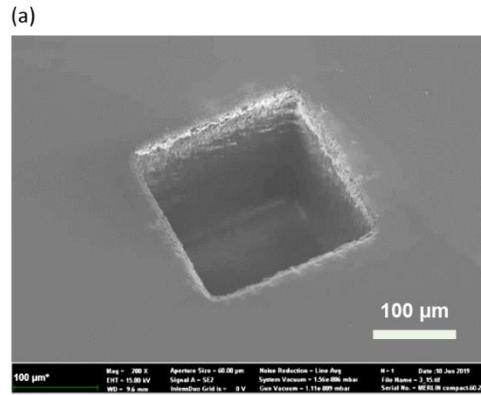
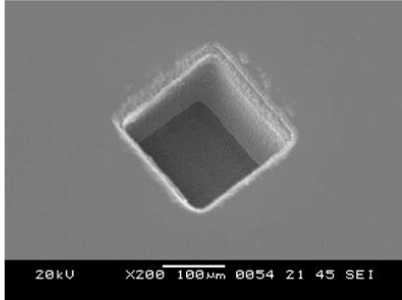


**Fig. 5.8 Square pocket fabricated with a random-point scan path:  
(a) SEM image and (b) 3D surface profile data.**

Various types of pockets could be generated with random-point scan paths. In this study, cross-shaped pockets, triangular-shaped pockets, and circular pillar depths of around 300  $\mu\text{m}$  were fabricated with these paths (Fig. 5.9). The scan path generation could be done only by changing the scanning area, which was the first step in the scan path generation.

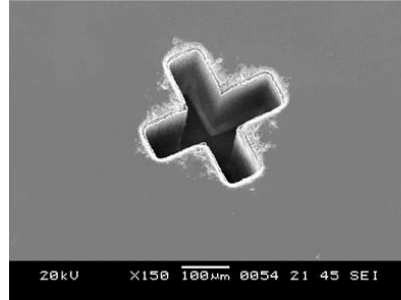
Not only vertical structures, but pyramid structures with slanted surfaces, could be fabricated by changing the scanning area (Figs. 5.10 and 5.11), since the machining depth was linearly proportional to the number of scans. By irradiating the area with a gradually increasing number of scans, a surface with a consistent angle could be fabricated. The depth and stiffness of the pyramid structure could be controlled by changing the number of scans (Fig. 5.11b); however, the tip of the pyramid structure broke more easily as the stiffness increased because of both the intensive heat accumulation of point irradiation and the absence of surrounding materials. Also, because the previously machined area was not further irradiated, layer marks remained on the surface, which increased the surface roughness. These layer marks could be smoothed by irradiating the same scan path with a smaller laser power (14 W), but this was not possible with the LIBWE process (Fig. 5.11c).

(a)



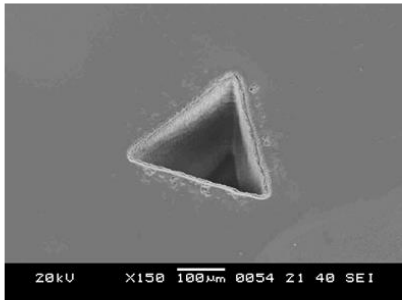
**Rectangular via hole**  
200  $\mu\text{m}$  length & depth,

(b)



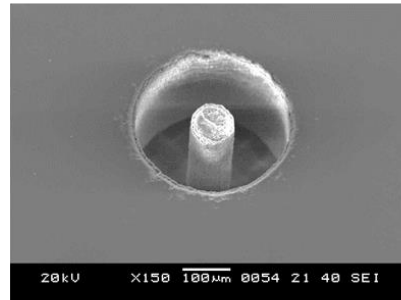
**Cross-shaped via hole**  
300  $\mu\text{m}$  length, 300  $\mu\text{m}$  depth

(c)



**Triangular via hole**  
200  $\mu\text{m}$  length, 350  $\mu\text{m}$  depth

(d)



**Circular pillar**  
80  $\mu\text{m}$  inner diameter, 300  $\mu\text{m}$  height

**Fig. 5.9 SEM image of pockets fabricated with a random-point scan path: (a) square pocket, (b) cross-shaped pocket, (c) triangular pocket, and (d) circular pillar.**

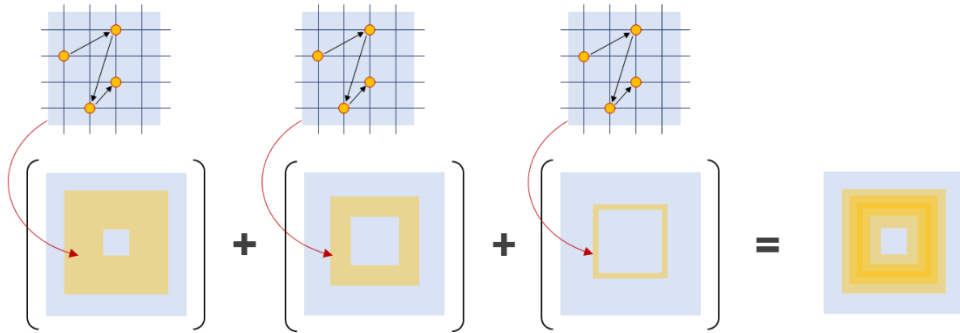
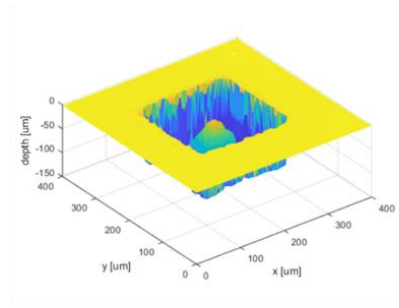
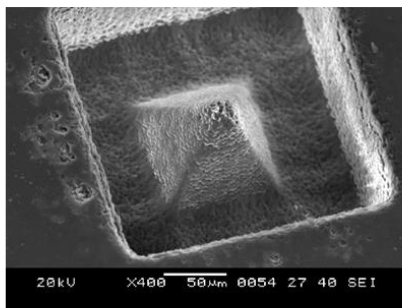
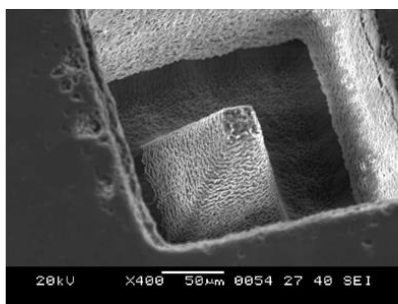


**Fig. 5.10 Random-point scan path generation for pyramid structure**

(a)



(b)



(c)

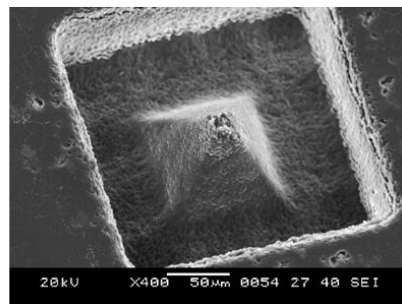


**Fig. 5.11 Glass pyramid structure fabricated with a random-point scan path: (a) SEM image and 3D surface profile of a pyramid fabricated with 20 W laser power and ten layer scans and (b) twenty layer scans; (c) a pyramid treated with additional laser scans.**

## 5.2.2. Random-line scan path

Although the random-point scan path had advantages for fabricating micropockets with minimal shape errors, it still had some disadvantages, such as a low material-removal rate due to the long resting time during the process and subsequent high surface roughness. Using random-line scan paths could help to mitigate those disadvantages owing to continuous laser irradiation. Generating a random-line scan path with an evenly distributed number of scans required a specific strategy. To achieve a randomly and evenly distributed scan path with minimal calculation, a specific algorithm was proposed [42]. Scan path generation started by selecting initial and final point sets, from which the most appropriate scan lines were determined based on a target number of scan-number maps and a score calculation filter. The overall scan path generation process is depicted in Fig. 5.12.

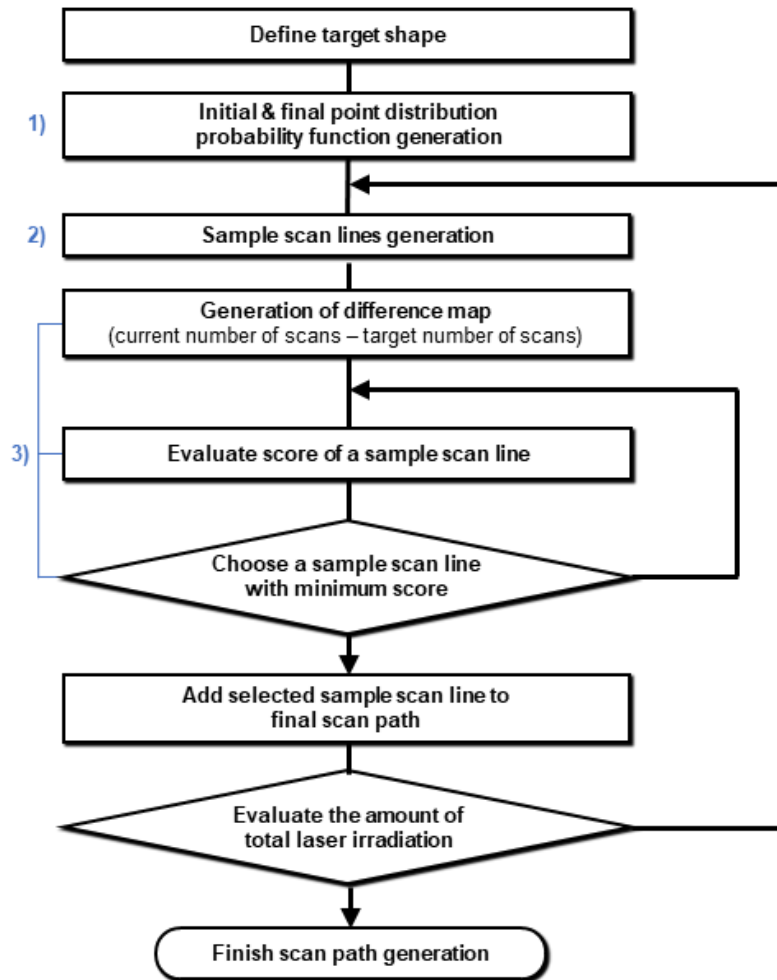


**Fig. 5.12 Basic design of generating random line scan path**

Some scan-number maps were utilized to simulate and visualize the number of scans across the machining area. When a scan path passed a certain grid, the number of scans of the grid increased by one. As depicted in Fig. 5.13, this number of scans increased as the scan path was piled on a certain grid. These scan-number maps could be compiled with different numbers of scans, and could be visualized to observe the uniformity of the laser scans (Fig. 5.14).

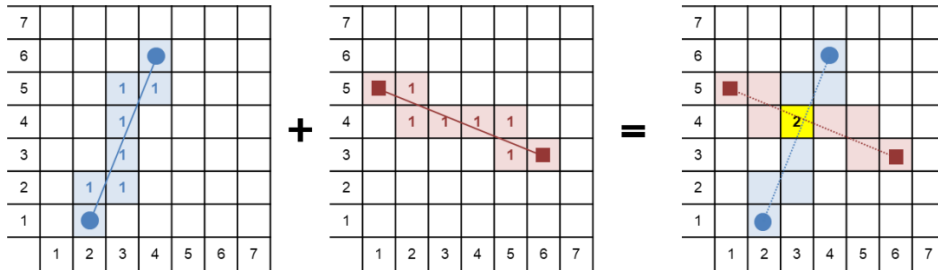


**Fig. 5.13** Diagram of scan-number maps for two random-line scan paths

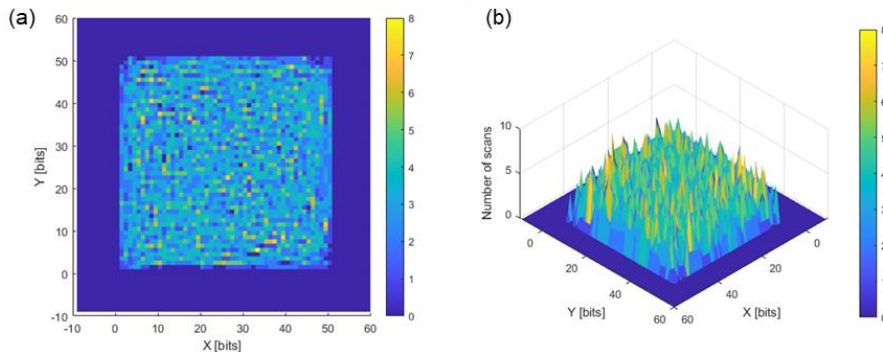


**Fig. 5.14. Scan-number maps inside a square area:**  
**(a) vertical view and (b) isometric view.**

Sample scan line generation and scan path score calculations were major factors in this scan path generation strategy. In the first step, sample lines were generated using a predefined point distribution probability function. Interaction between the laser beam and the bubble could have unintentional effects on the final geometry, resulting in significant shape errors, especially at the final points of laser scan lines, as depicted in Fig. 5.3. The initial and final points of a scan line needed to be distributed so that the effect of the bubble could be spread across the machining area and prevent shape errors. The point distribution probability function was defined according to the shape and distribution of the target number of scans (Fig. 5.15a).

Next, sample lines were randomly generated based on the point distribution probability function. When a scan path with a regular pattern is used, start, stop, and moving direction changes of the scan point are inevitable, and they overlap in the same area. As a result, changes in scanning speed create an unexpected pattern on the machined surface. To avoid an unexpected pattern, a scan path with irregular scan lines was created by connecting randomly generated initial and final points. The positions of the initial and final points were generated according to the point distribution probability function (Fig. 5.15b), so that the initial and final points of the scan lines were evenly distributed along the final scan path.



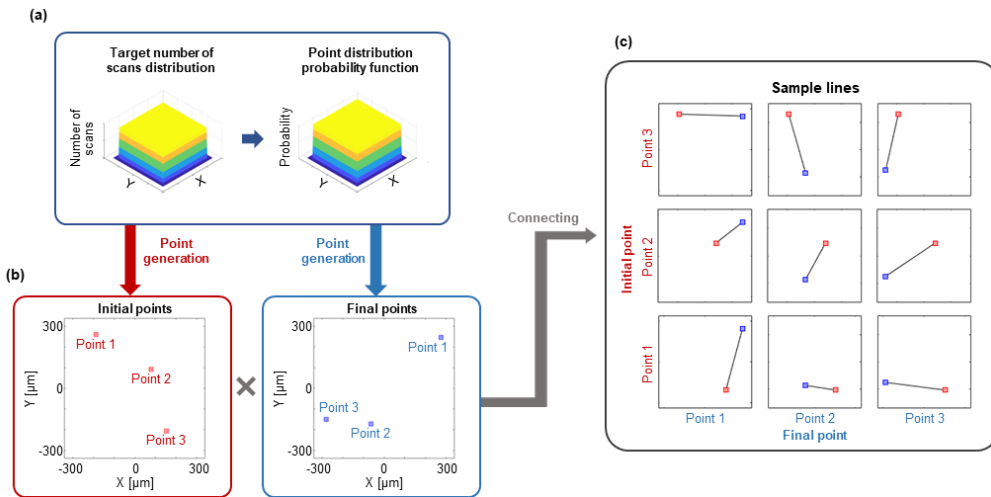


**Fig. 5.15 Diagram of generating initial and final point sets from a predefined probability density function.**

To match the laser irradiation distribution to the target shape, the most suitable scan line was selected from among the generated sample lines. First, predefined numbers of initial and final sample points were determined, and sample lines were generated by connecting all the initial and final sample points (Fig. 5.15c). At the end of the sample scan line generation process, sample lines shorter than the predefined minimum length were neglected to avoid unexpected effects of the point-wise laser scan and low material removal rate (MRR). Each sample line score was calculated based on the previously generated scan path and the scoring filter obtained from the sample line. The applied scoring filter from a sample line is depicted in Fig. 5.16 and Equation (8):

$$C_{xy} = \begin{cases} \frac{W - 2r_{xy}}{W}, & \text{if } d \leq \frac{W}{2} \\ 0, & \text{otherwise} \end{cases} \quad (8)$$

where  $C_{xy}$  is the filter value at a point  $(x, y)$ ,  $W$  is the scoring filter width, and  $r_{xy}$  is the minimum distance from the sample line to the point  $(x, y)$ .

The scoring filter was designed with a positive ridge shape that decreased as the distance from the line increased to identify both valley-shaped distributions and small numbers of scans. Points whose distance from the line is larger than  $W/2$  were given a zero filter value that did not affect the final score for the path. Of the various types of scoring filters, ridge filters performed more effectively than other types of filters, such as gradient filters and average filters.

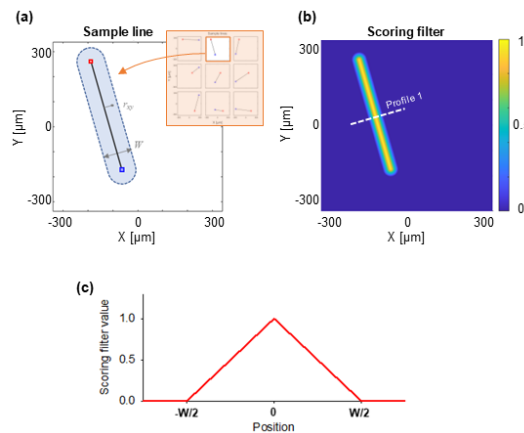


**Fig. 5.16 Scoring filter for a sample line taken from randomly generated sample lines: (a) notations and area of the scoring filter, (b) a generated scoring filter from a sample line, and (c) filter shape for transverse direction profile 1.**

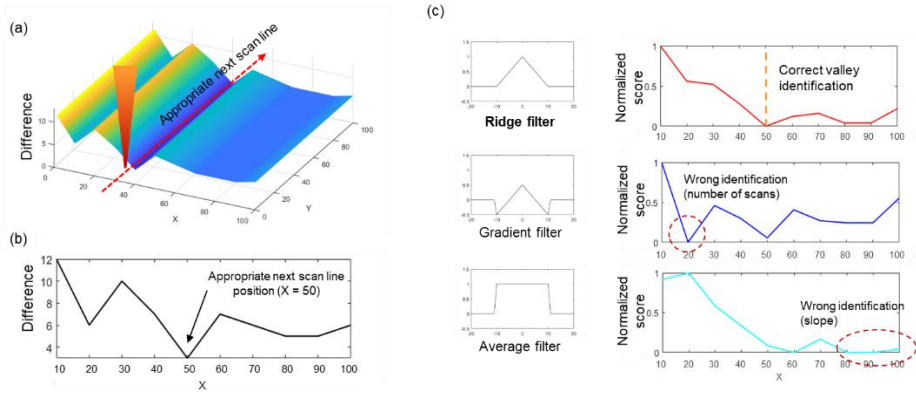


**Fig. 5.17** An example scan-line scoring process: (a) one-dimensional scan-number distribution, (b) scan-number distribution profile in the X direction, and (c) normalized scores from a ridge filter, gradient filter, and average filter.

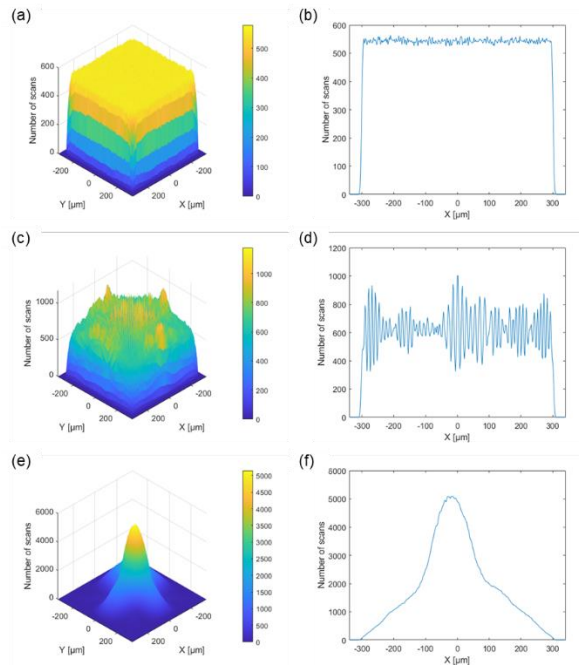


**Fig. 5.18** Generated scan-number distributions using various scoring filters: (a) 3D profile, (b) 2D profile at  $Y = 0$  with a ridge filter, (c) 3D profile, (d) 2D profile at  $Y = 0$  with an average filter, (e) 3D profile, and (f) 2D profile at  $Y = 0$  with a gradient filter.

Scores for each sample random-line scan path were calculated to find the most appropriate scan path among the samples. The gradient filter and average filter are the most widely applied filters to identify or smooth edges, and the performance of those filters for finding an appropriate line position was evaluated on a sample surface, as depicted in Fig. 5.17. In this case, the gradient filter could identify the valley with the largest slope regardless of the value of the valley. By contrast, the average filter could find the lowest point but could not identify the valley, which resulted in a rough scan-number map. As a result, valleys in the scan-number maps with the lowest numbers were targeted and identified by applying a mixed gradient and average filter. These trends could be observed from the scan distribution resulting from a scan path generated by each filter (Fig. 5.18). The scan distribution from the ridge filter could only generate a scan path with an even distribution.

A difference map for the current scan path (Fig. 5.19) was generated by subtracting the target scan-number distribution from the current scan-number distribution. The current scan-number distribution was generated by adding all the previously generated scan line scoring filters with a width of 2  $\mu\text{m}$ . The target scan-number distribution had the same total number of scans as the current distribution and followed the exact target shape.

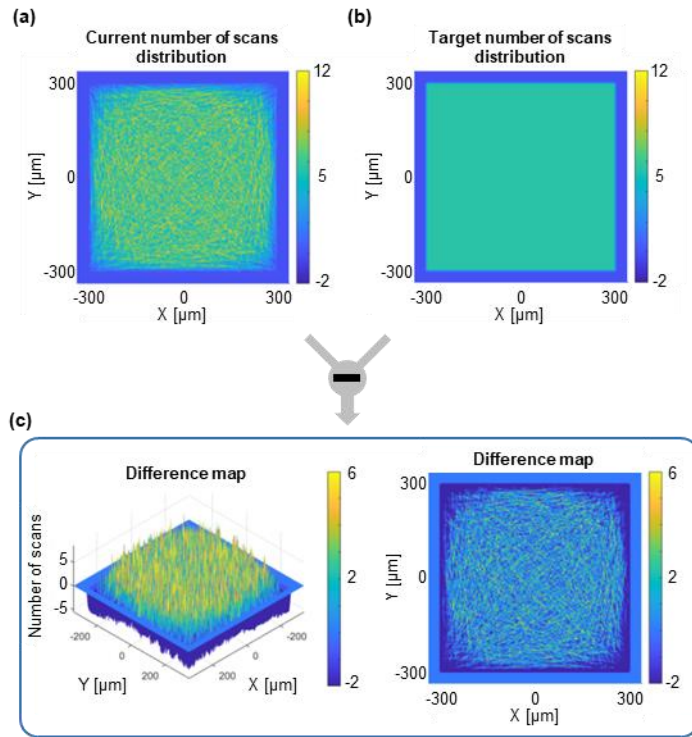


**Fig. 5.19** Difference map calculation diagram: (a) current scan-number distribution, (b) target scan-number distribution, and (c) generated difference map.

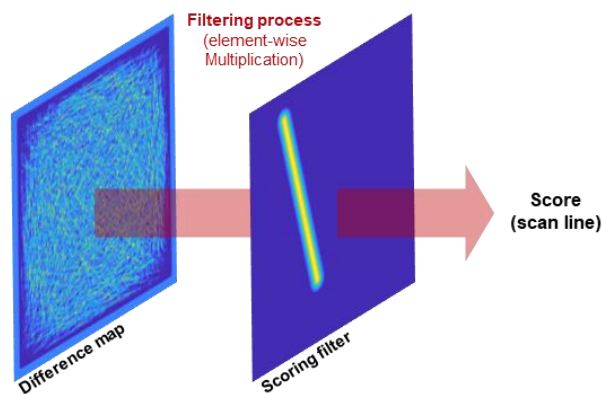


**Fig. 5.20** Score calculation for a sample scan line with a difference map and scoring filter.

The final score of a scan line was calculated by multiplying the scoring filter values and difference map values elementwise and then summing them as depicted in Fig. 5.20 and Equation (9):

$$S = \frac{1}{n_c} \sum_{(x,y) \in M} N_{xy} C_{xy} \quad (9)$$

where  $S$  is the calculated score of a line,  $n_c$  is the number of calculated points inside the target area,  $N_{xy}$  is the difference map value at a point  $(x, y)$ , and  $M$  is the group of points in the target scoring area.

Because the scoring filter was a positive ridge shape, the score for the scan line was small when the profile of the difference map at the scan line location had a small value and V-shape. As a result, it was possible to score all sample scan paths and add the scan path with the smallest score to the current scan path, resulting in a scan path with well-distributed laser irradiation. Points that were not inside the target area were excluded from the score calculation. Points outside the target area had a small or zero number of scans because no scan lines were located outside the target area. If these points were included in the scoring calculation, sample lines containing points outside the target area were scored lower than the intended value. Consequently, the sample lines near the edge of the target area were more likely to be selected, and a scan path with an uneven distribution of the

number of scans was created.

The feasibility of applying the proposed random-line scan path generation method was investigated by machining a square micropocket. As depicted in Fig. 5.21, a square micropocket without severe additional machining at the edge and unintended pattern could be fabricated under the same conditions listed in Table 5.2. Square pockets, cross-shaped pockets, triangular pockets, and rectangular pillars were fabricated with generated random-line scan paths, as for structures fabricated with random-point scan paths (Fig. 5.22). All structures were fabricated without cracks or breakage during the process, which proved that specific cracking did not occur during the LIBWE process with a randomly generated line scan path.

As in the case of random-point scan paths, pyramid structures with slanted surfaces could be fabricated by changing the scanning area (Fig. 5.23). The height of the pyramid structure increased as the duration of laser irradiation increased. The surface roughness of the slanted surface improved compared to the surfaces produced by the random-point scan path. Tip breakage occurred as the stiffness increased, as in the case of the random-point scan path. Not only pyramid structures, but also structures with peaks and valleys, could be fabricated. In this case, due to the material supply in one direction, tip breakage at the edge of the peaks was prevented.

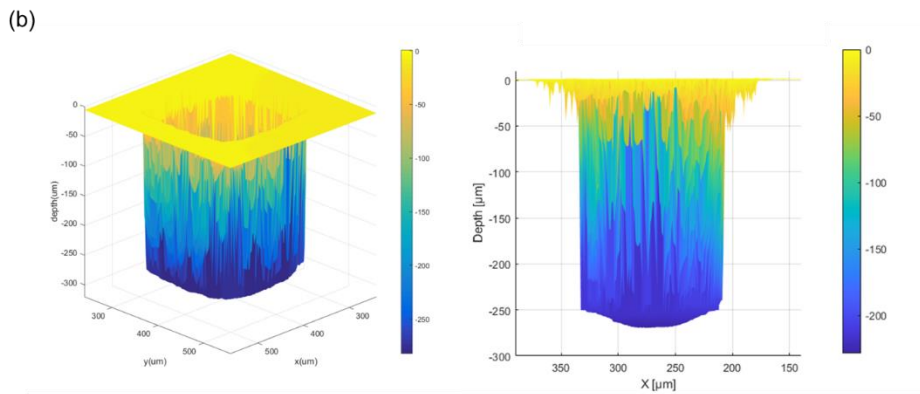
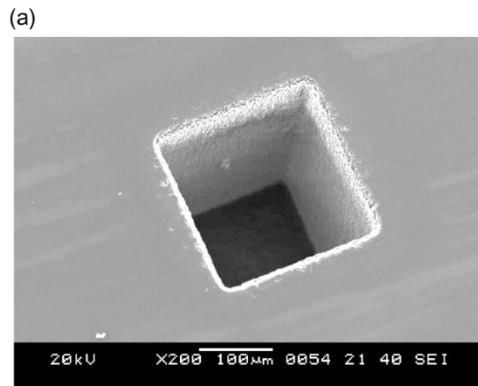


**Fig. 5.21 Square pocket fabricated with a random-point scan path:**  
**(a) SEM image, (b) 3D surface profile data, and (c) machined depth compared to the process time.**



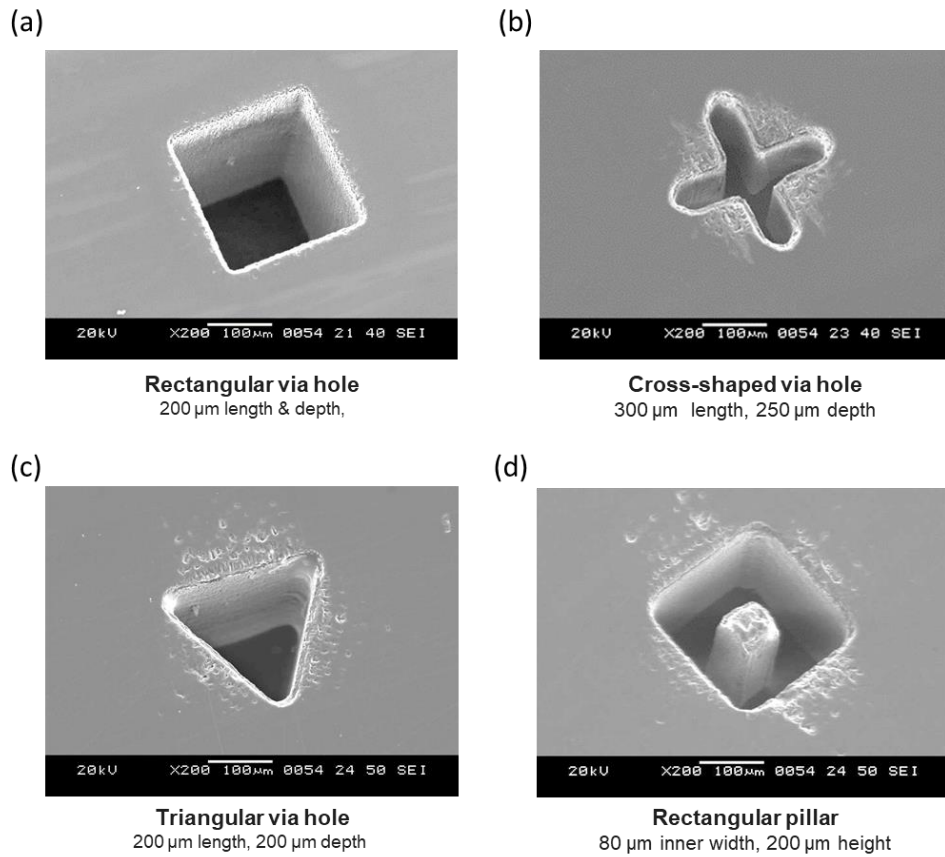


**Fig. 5.22 SEM image of a pocket fabricated with a random-line scan path: (a) square pocket, (b) cross-shaped pocket, (c) triangular pocket, and (d) rectangular pillar.**

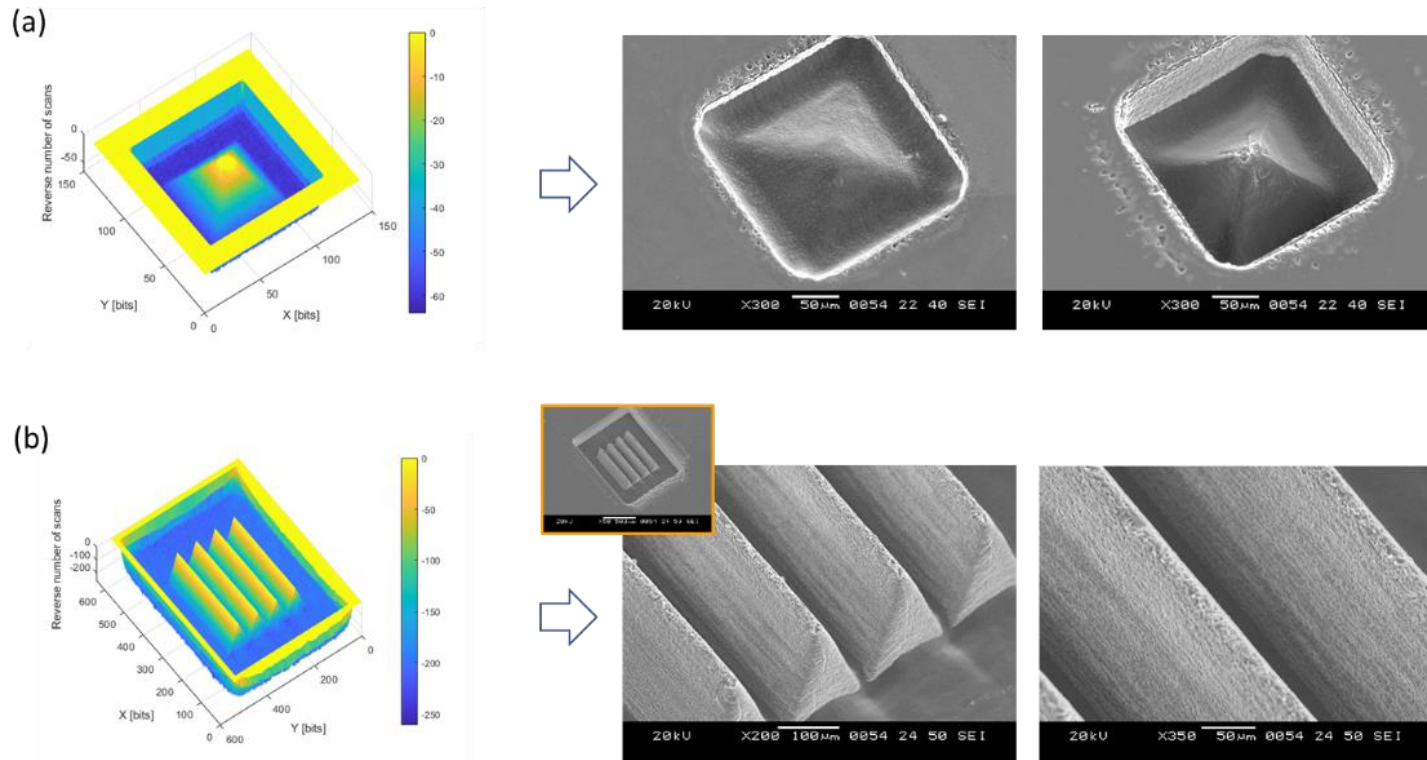


**Fig. 5.23 Negative scan-number map and SEM images for (a) pyramid structures and (b) structures with peaks and valleys fabricated with a random -ne scan path.**

## **5.3. Effects of Random-Line Scan Path Generation Parameters**

This section describes the investigation of the effects of the random-line scan path generation parameters on machining characteristics. The experimental laser conditions are listed in Table 5.3, and the scan path generation parameters are listed in Table 5.4. Major parameters for the random-line scan path generation, which affected the final scan distribution and the amount of computation, were determined to be as follows: number of sample points, minimum length, and scoring filter width. The number of sample points determined the number of possible sample lines to be observed, the minimum length directly affected the scan length distribution, and the scoring filter width affected the precision of choosing the most appropriate scan line. To minimize grooves on the surface due to the Gaussian laser beam, intervals between lines and points were set at 2  $\mu\text{m}$ , which was the resolution of the scan-point positioning system. During the parameter study, the other parameters were fixed as default values (6 sample points, 30% of the width as the minimum length, and a 12  $\mu\text{m}$  scoring filter width). The effects of the parameters on the actual machining characteristics (MRR, normalized depth deviation, and average roughness [ $R_a$ ]) were measured and explained by the

characteristics of the generated scan paths. Normalized depth deviation was calculated by dividing the standard deviation of depth by the average depth of the target area, as shown in Equation (10):

$$Z_n = \sqrt{\frac{1}{N-1} \sum_{i=1}^N |z_i - \bar{z}|^2} / \bar{z} \quad (10)$$

where  $Z_n$  is the normalized depth deviation,  $N$  is the number of points in the target area,  $z_i$  is the depth of the  $i$ th point, and  $\bar{z}$  is the average machined depth.

**Table 5.3**

**Laser micromachining conditions for the study of the random-line scan path generation parameters.**

<b>Parameter</b>	<b>Value</b>
Laser power	20 W
Frequency	65 kHz
Scanning speed	150 mm/s
Copper sulfate concentration	0.7 M
Phosphoric acid concentration	40 wt%
Machining time	< 2000 s

**Table 5.4**

**Path generation conditions**

<b>Parameter</b>	<b>Value</b>
Number of sample points	2, <b>6</b> , 10
Minimum length compared to width of a square [%]	10, <b>30</b> , 50, 70
Scoring filter width [ $\mu\text{m}$ ]	4, <b>12</b> , 20
Width and height of target square [ $\mu\text{m}$ ]	600
Grid interval [ $\mu\text{m}$ ]	2
Number of scan lines	500,000

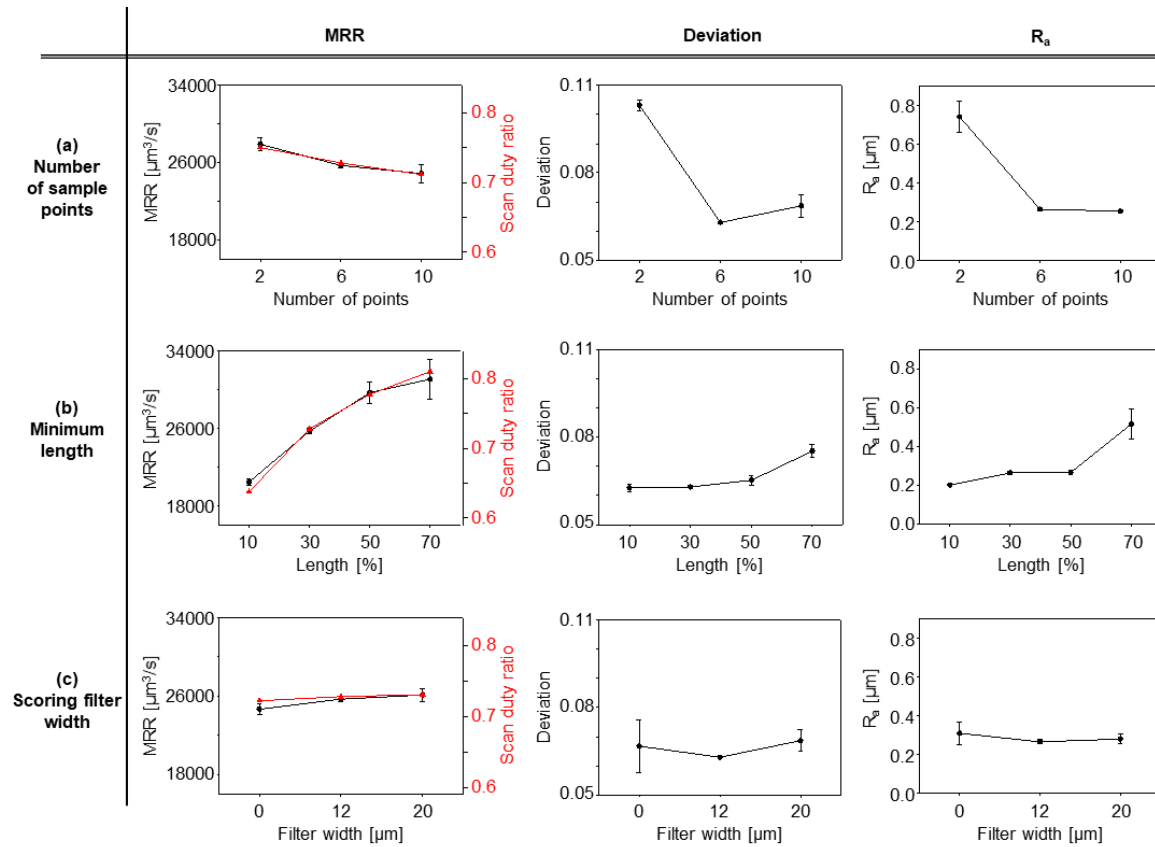


**Fig. 5.24. Machining characteristics corresponding to parameter changes: (a) number of sample points, (b) minimum length, and (c) scoring filter width.**

### 5.3.1. Number of sample points

The number of sample points determined the number of scan lines that needed to be explored. In this study, by setting identical numbers of initial and final points, the number of sample scan lines was determined to be the square of the number of points. A large number of sample scan lines increased the likelihood of choosing an appropriate scan path for effective laser irradiation distribution. The effects of changing the number of sample points on the machining characteristics are shown in Fig. 5.24a.

The MRR of scan paths generated with a small number of sample points (2 points) had a large value ( $27,900 \mu\text{m}^3/\text{s}$ ), while the MRR decreased as the number of sample points increased (10 points,  $24,900 \mu\text{m}^3/\text{s}$ ). An MRR change due to the number of sample points could be explained by scan path length, the scan duty ratio, and the laser scanning duration of the entire process time for each scan path (Fig. 5.25). The control phase of the galvanometer was divided into two steps: a mark state and a resting state. After the laser irradiated in the mark state, the laser turned off in the resting state and jumped to the next initial point. Also, to simplify the movement of the scanning point, several delays were applied in every scan and jump for the compensation of the galvanometer's vibration. These jump periods and

delays determined the laser-off period, which decreased the scan duty ratio. Because delays occurred at every scan and jump, scan paths with long average scan line lengths had larger scan duty ratios, and it was possible to irradiate with greater energy in the same machining time. This relationship between scan line length, scan duty ratio, and MRR was observed from various experimental results in this study.

Because the areas where the laser irradiation was insufficient were densely and irregularly distributed, scan lines with a short length were less likely to pass through the areas with many scans. As a result, scan lines with short lengths were more likely to be selected as the next scan line because they were more likely to have a small score than long scan lines. However, the smaller the number of sample points, the longer the distance between the sample points, and the easier it was for a particularly long scan line to be selected as the next scan path. This trend could be observed from the scan line length distribution depicted in Fig. 5.26a. Short scan lines were more likely to be chosen as scan paths created with 10 sample points, while long lines were often chosen as scan paths generated with 2 sample points.



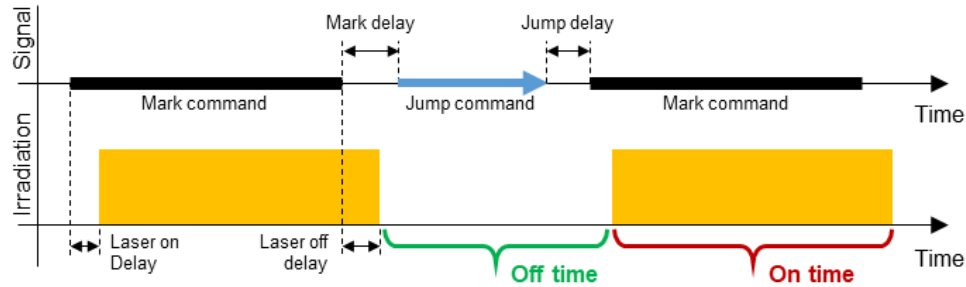


**Fig. 5.25** Diagram of the control parameters of the interface board and corresponding laser irradiation

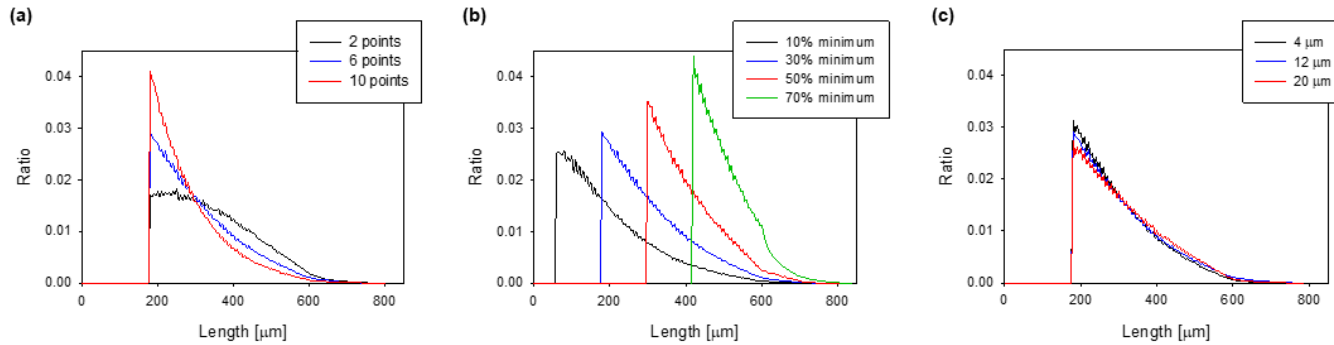


**Fig. 5.26** Machining characteristics corresponding to parameter changes: (a) number of sample points, (b) minimum length, and (c) scoring filter width.

Both normalized depth deviation and average surface roughness decreased from 0.10  $\mu\text{m}$  to 0.06  $\mu\text{m}$ , and 0.74  $\mu\text{m}$  to 0.26  $\mu\text{m}$ , respectively, as the number of sample points increased from 2 to 6. Surface quality did not alter significantly as the number of sample points increased from 6 to 10. Deterioration of the surface quality was observed on the processed surface compared to the surface machined under the basic conditions (Fig. 5.27), based on a few sample points. This could be explained by the uneven distribution of the laser irradiation (Fig. 5.28). As mentioned in the previous paragraph, an appropriate scan path was likely to be found with sufficient sample scan paths. If a small number of sample paths were provided, it was highly likely that no suitable path existed among the sample scan paths. As a result, it appeared to create an uneven distribution of laser irradiation along the final full scan path. This trend was observed from the scan-number distributions for different numbers of sample points in Figures 5.28a and 5.28b. Comparing the distribution of the number of scans (Fig. 5.28b) with the actual machined surface (Fig. 5.27b) showed that the machined surface morphology followed that distribution, resulting in increased depth deviation and surface roughness.

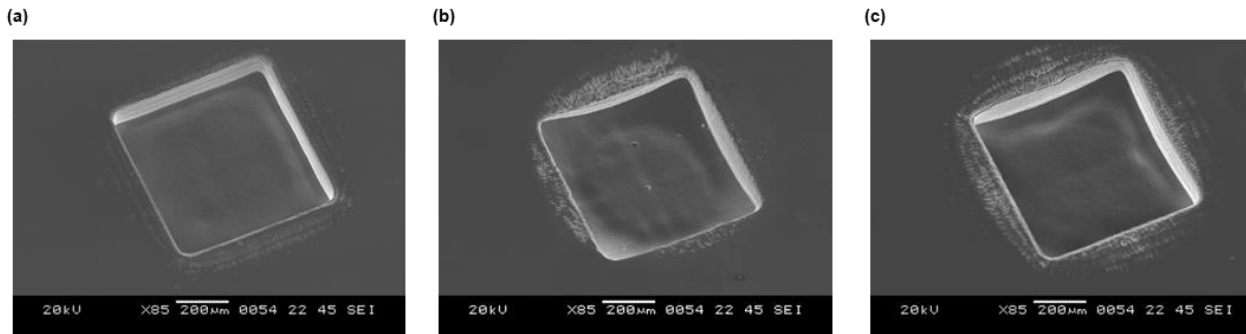


**Fig. 5.27 SEM images of square micropockets machined with different scan path generation parameters: (a) basic condition (6 sample points, 30% minimum length, and 12  $\mu\text{m}$  filter width); (b) 2 sample points and (c) 70% of width at minimum length.**

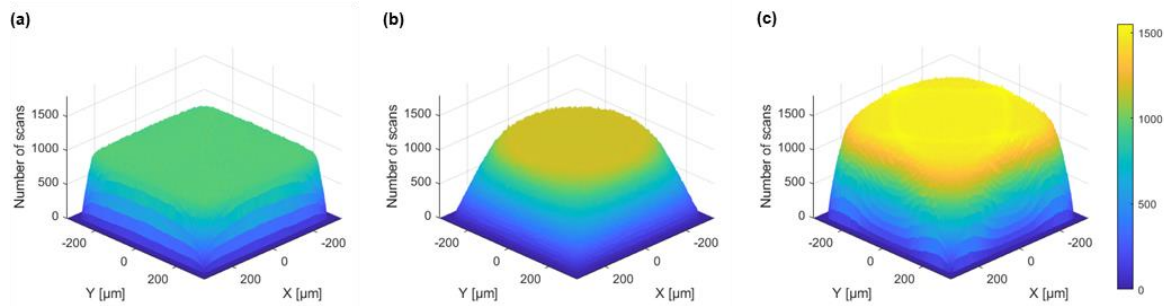


**Fig. 5.28 Scan distributions with different scan path generation parameters: (a) basic condition (6 sample points, 30% minimum length, and 12  $\mu\text{m}$  filter width); (b) 2 sample points; and (c) 70% of width at minimum length.**

### 5.3.2. Minimum length of a scan line

In the scan path generation algorithm, a minimum length of a single scan line was set to eliminate point-like scan paths and increase the material removal rate. Along with the number of sample points, the minimum length of the scan line also affected the machining characteristics of LIBWE, as depicted in Fig. 5.24b.

MRR increased as the minimum length increased. As mentioned in the previous section, scan lines with short lengths were likely to have small scores and be selected as the next scan path. Changing the minimum length altered the distribution of the scan lines' length. The minimum length increased, so the length distribution was concentrated in short to long length regions (Fig. 5.26b). This change in length distribution resulted in an increase in the scan duty ratio. As a result, the MRR increased from 20,450  $\mu\text{m}^3/\text{s}$  to 29,700  $\mu\text{m}^3/\text{s}$ , then to 31,100  $\mu\text{m}^3/\text{s}$ , as the minimum length increased from 10% to 50% to 70% of the width, respectively.

The normalized depth deviation and average surface roughness barely changed with increases in the minimum length up to 50% of the width. Although the possible range of the scan line length was limited by a long minimum length, appropriate scan paths for even irradiation could be

explored due to the sufficient number of sample scan lines until the minimum length was 50% of the width. By increasing the minimum length to 50% of the width, it was possible to increase the MRR with no deterioration in surface quality due to the even distribution of the number of scans. However, when the minimum length was 70% of the width, the depth deviation and surface roughness increased. Due to the long minimum length, the possible position of a sample line was more limited than for other scan lines with shorter minimum lengths. This position restriction made it difficult to evenly distribute long scan lines across the target area, and a scan path with an uneven scan distribution was thus created. As in the case with two sample points, a pattern of protrusions emerged from the distribution of the number of scans (Fig. 5.28c), and a similar pattern transferred to the actual machined surface (Fig. 5.27c). Based on these observations, when an error-compensating scan path was used, the machined surface could be predicted from the scan distribution, and it was thus important to create a scan path that fitted the intended distribution of the number of scans.

### **5.3.3. Scoring filter width**

To achieve an even distribution of laser irradiation, a score calculation for each scan line using a scoring filter and difference map was proposed. As the scoring filter width increased, the area covered by the calculation also increased, taking more points into consideration. However, as depicted in Fig. 5.24c, the change in width hardly affected the machining characteristics; nor did the scoring filter width affect the characteristics of the length distribution of scan paths, which could be identified from single-line scan-length histograms (Fig. 5.26c). Since each scan path was added after calculation, the scan-number distribution tended to remain uniform throughout the entire scan path generation process. As a result, the distance between the ridges and valleys of the scan-number distribution was close enough to allow a narrow scoring filter to identify a suitable area for scanning.

## 5.4. Degree of Precision in Complicated Structure Fabrication

To evaluate the performance of fabricating a 3D structure, a complicated 3D structure with a slope, a cross, and a narrow width was designed and fabricated. By designing a target map with a target depth profile, an appropriate random-line scan path could be generated, as depicted in Fig. 5.28. Although the number of scans was not evenly distributed throughout the target map, because peaks and valleys closer than the machine width ( $20\ \mu\text{m}$ ) could be ignored during the actual machining, an actual glass structure with a smooth surface was fabricated (Fig. 5.29).

As depicted in Fig. 5.30, machining results and simulation data were compared through two vertical lines ( $y = 500\ \mu\text{m}$  and  $x = 620\ \mu\text{m}$ ). For the  $y = 500\ \mu\text{m}$  line, an intended slope between circles was very noticeable in both the simulation and the machined data, with flat surfaces inside circles. The profiles of the simulation data and the actual machined structure were well matched by multiplying an appropriate constant to the simulation data ( $4/3$ ). This match was also observed for the  $x = 620\ \mu\text{m}$  line. Also, in both the simulation and actual data, two symmetric narrow curves had the same depth.

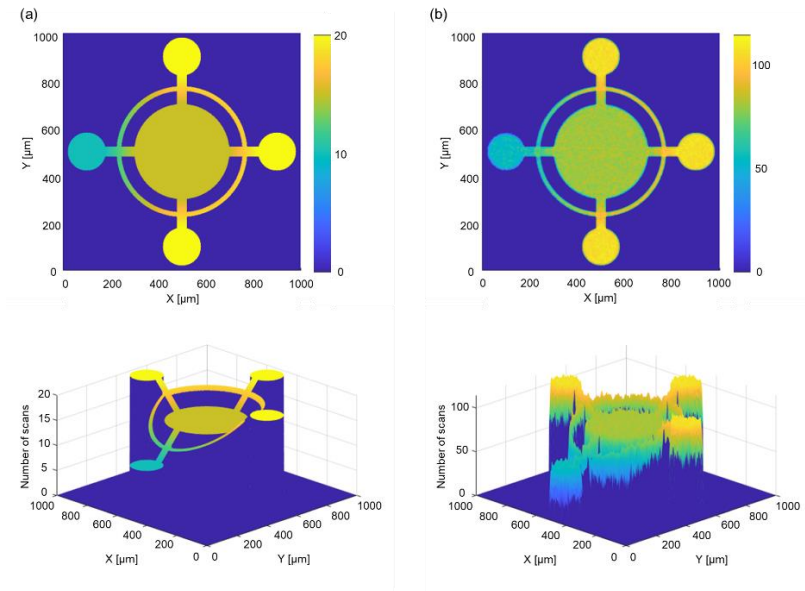


**Fig. 5.29 Reversed 3D data of (a) target structure and (b) simulated results in different perspectives**

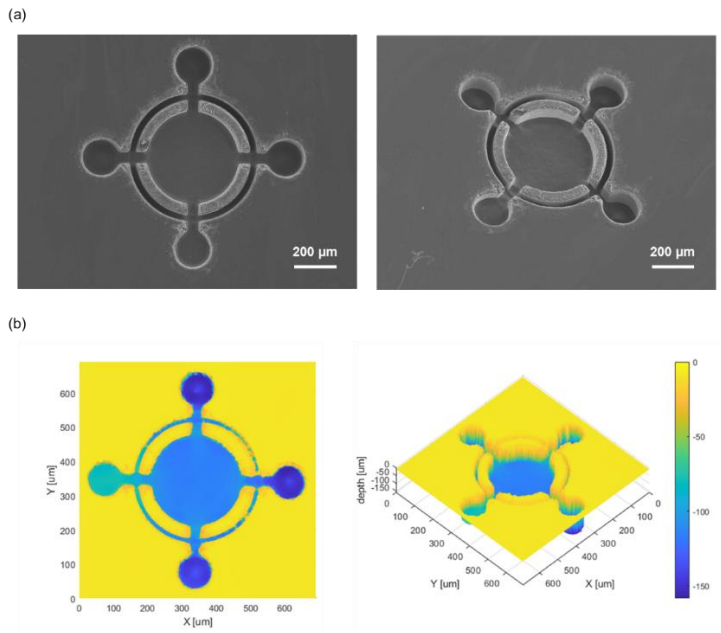


**Fig. 5.30 Fabricated glass structure with random line scan path (a) SEM image, (b) 3D surface profile**



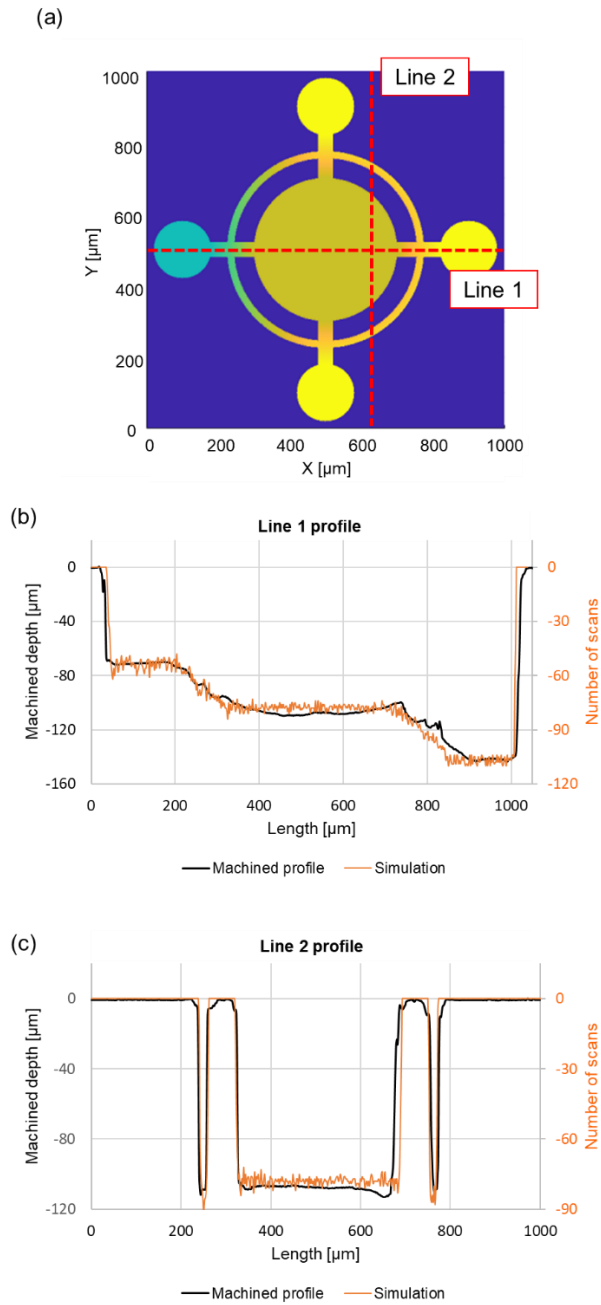


**Fig. 5.31 Comparison between simulation data and actual machined profile (a) position of comparison, (b) comparison results  $Y = 500 \mu\text{m}$ , (c) comparison results through  $X = 620 \mu\text{m}$ .**

# Chapter 6

## Feasible Applications

This chapter describes various fabricated glass structures and explains the investigation of their feasibility for certain applications. First, high-aspect-ratio glass microstructures for capillary-driven flow were fabricated. A 5-mm-length microchannel with a width of 20  $\mu\text{m}$  and depth of 200  $\mu\text{m}$  was fabricated as depicted in Fig. 6.1, and the fabricated channel is shown in Fig. 6.2. The glass substrate was covered with a PDMS plate.

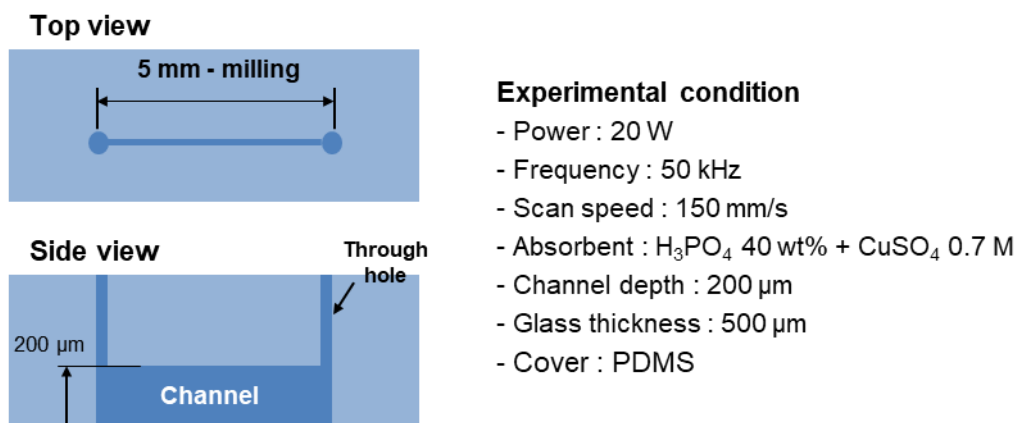


**Fig. 6.1** Diagram of fabricated channel and experimental condition.

Capillary-driven flow could be initiated by introducing a drop of dyed solution into a drilled hole, and the propagation of the capillary-driven flow was observed using an optical microscope. Based on the observation, the solution propagated at a speed of 2.8 mm/s.

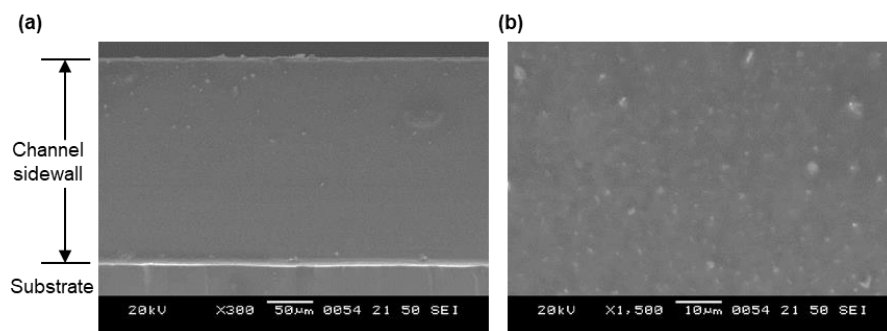


**Fig. 6.2 SEM images of sidewall of the fabricated channel (a) normal image (b) enlarged image.**

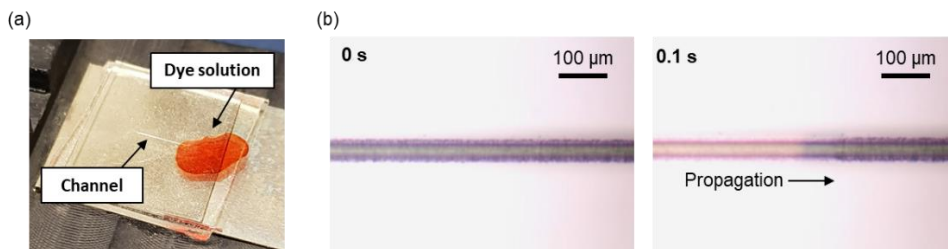


**Fig. 6.3 Experimental images of capillary driven flow (a) glass microchannel and dyed solution (b) propagation of the dyed solution inside the fabricated glass microchannel.**

Owing to the transparency and hardness of glass materials, glass micropatterns can be used as molds for UV imprints. In particular, by installing a glass mold on a surface and placing UV curing resin underneath the glass mold, it is possible to fabricate 3D microstructures in a comparatively short time. Due to these advantages, reverse contact UV imprints have been widely studied and used for various applications, especially for submicrometer scale microstructures [43,44]. With the LIBWE process, it was possible to fabricate glass structures with a scale of tens of micrometers on a glass substrate and investigate the feasibility of those fabricated structures for reverse UV contact imprints.

For the experiment, a UV curing system was established, as depicted in Fig. 6.4. A UV lamp with a 405 nm wavelength and 5,000 mW intensity was employed to cure a UV resin widely used in stereolithographic 3D printing. For ease of detachment, a circular cone glass mold was fabricated with experimental conditions based on the experimental results, as depicted in Fig. 6.5. With these conditions, it was possible to fabricate a three-by-three cone array on a glass substrate (Fig. 6.6) and a replicated polymer cone array of 200  $\mu\text{m}$  bottom diameter, 40  $\mu\text{m}$  top diameter, and 180  $\mu\text{m}$  height (Fig. 6.7). The curing process proceeded for 1 min, which was comparably faster than the machining process.

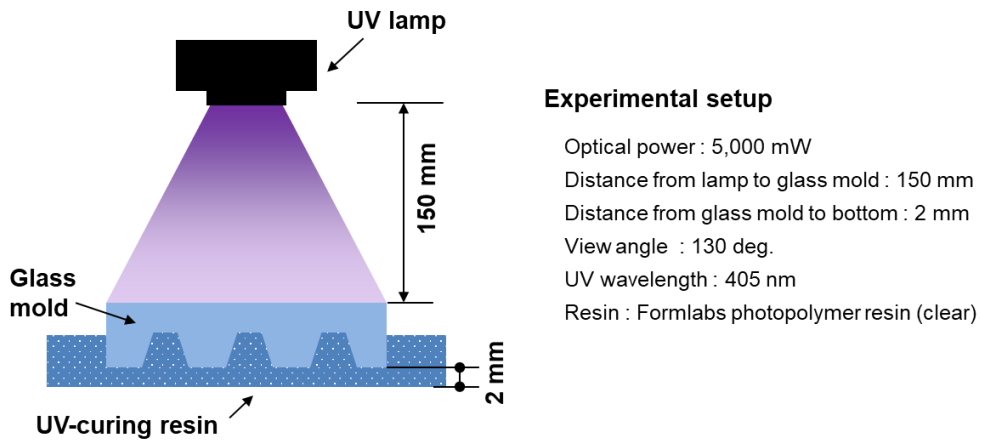


**Fig. 6.4 Diagram of UV curing system and experimental setup.**

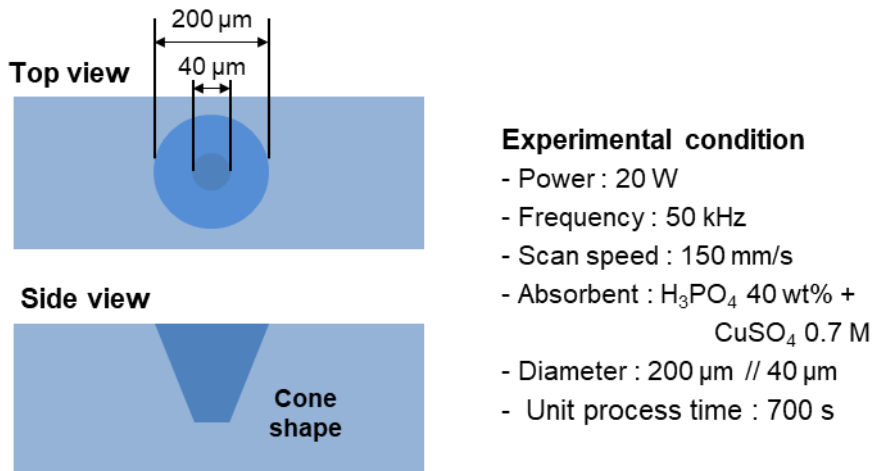


**Fig. 6.5 Diagram of fabricated glass mold and experimental condition.**

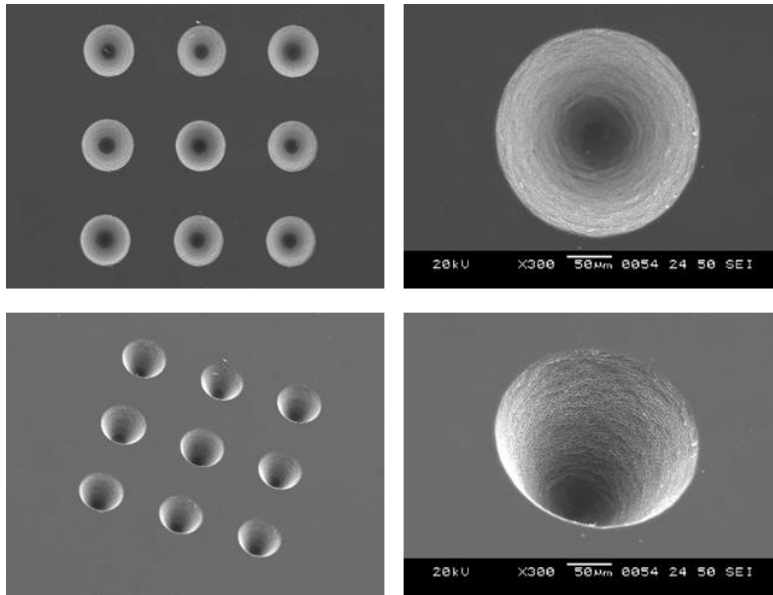


**Fig. 6.6 SEM images of glass molds.**

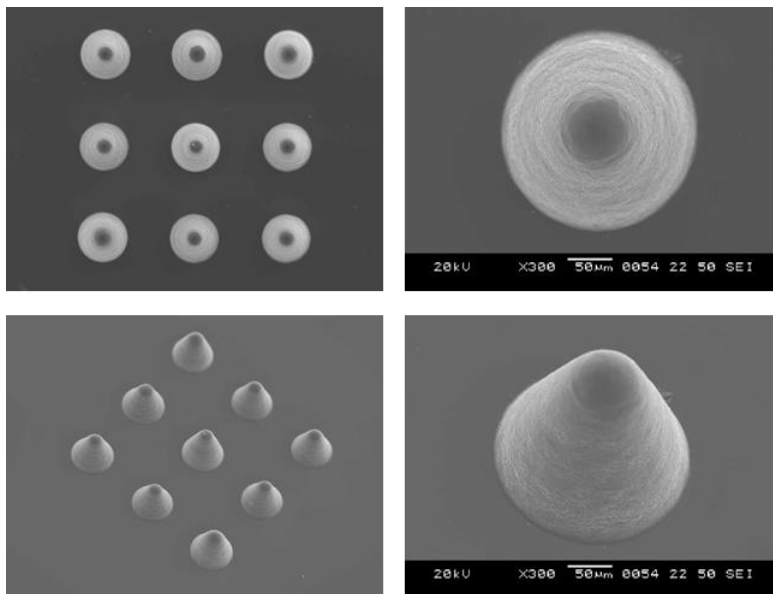


**Fig. 6.7 SEM images of replicated polymer structures.**

The feasibility of glass cutting to fabricate a standalone glass component was investigated by fabricating a high-aspect-ratio standalone glass structure with straight lines and curves with various curvatures. A tensile specimen resembling a glass microstructure with a maximum width of 200  $\mu\text{m}$  and length of 1,800  $\mu\text{m}$  was designed, as depicted in Fig. 6.8. This structure could be fabricated on a 500- $\mu\text{m}$ -thick glass substrate. The fabricated component had a minimum width of 80  $\mu\text{m}$  at the center and an aspect ratio of 6.25 (Fig. 6.9).

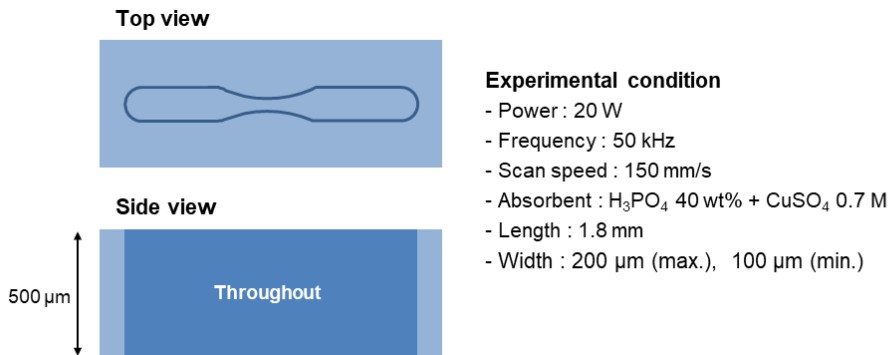


**Fig. 6.8 Diagram of a fabricated glass mold and experimental condition.**

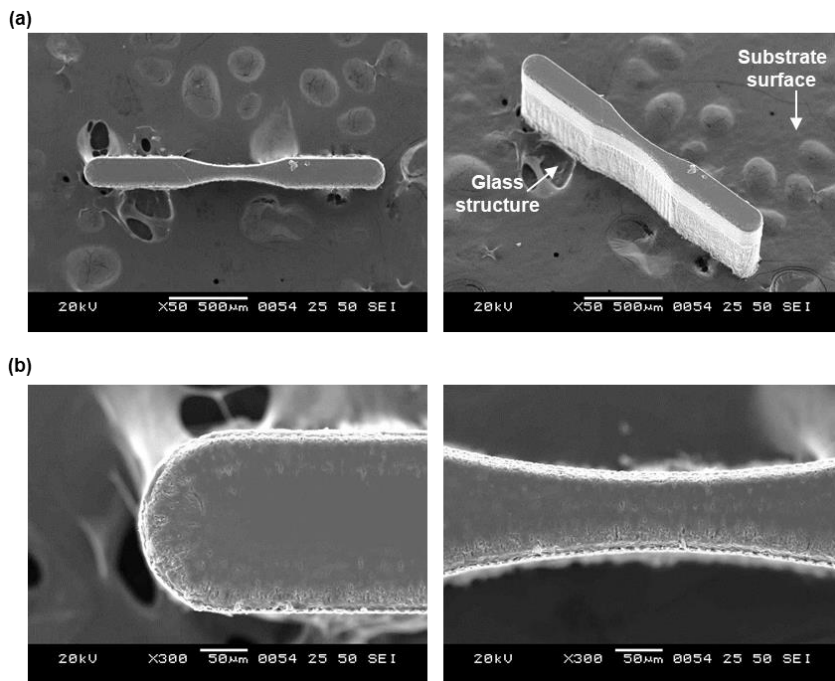


**Fig. 6.9 Fabricated glass standalone structure: (a) SEM image and (b) magnified image.**



# Chapter 7

## Conclusion

This study investigated the effect of phosphoric acid added to the absorbent in an NIR LIBWE process and proposed that structures of various shapes could be fabricated with an industry-friendly device, with proper MRR (Fig. 7.1). By adding phosphoric acid to the absorbent, the processable aspect ratio increased in the LIBWE process. The principle of processability expansion was supported by *in situ* process observations and elemental analysis. For a copper sulfate absorbent, positive feedback of the laser energy absorption, copper oxide and gas by-product generation, and the inhibition of liquid circulation resulted in heat accumulation. Cracks were generated due to the accumulated heat in the vapor and deposited copper oxide. The silicon phosphate generation process used an absorbent with added phosphoric acid. The silicon phosphate protective layer inhibited copper oxide adhesion, suppressing thermal cracks due to heat accumulation.

The effects of process parameters on maximum fabricable depth, sidewall roughness, fabrication speed, and machinability were investigated both theoretically and experimentally. The maximum fabricable depth of the

LIBWE milling process increased from 103  $\mu\text{m}$  to 530  $\mu\text{m}$ , and the sidewall roughness ( $R_a$ ) decreased from 0.55  $\mu\text{m}$  to 0.16  $\mu\text{m}$ , when the phosphoric acid concentration increased in increments from 0 *wt%* to 40 *wt%*. However, the fabrication speed decreased as the phosphoric acid concentration increased. The fabrication speed and machinability could be controlled by other energy-influencing parameters, such as copper sulfate concentration, laser power, and laser scanning speed. Average power density and single point energy density were the main indexes used to evaluate the machining characteristics.

The performance of LIBWE with phosphoric acid-added absorbent for fabricating 3D glass structures was also investigated and improved by applying a new scan path generation method. Random-line scan paths were generated by selecting random initial and final point sets from a predefined probability density function and finding the most appropriate scan path from a possible combination of given point sets. The performance of the new scan path generation method was evaluated by fabricating various types of structures, including square pockets, cross-shaped pockets, triangular pockets, pillars, structures with slopes, and a complicated structure. The effects of scan path generation parameters on machining characteristics were investigated. The number of sample points mainly affected surface quality, such as normalized depth deviation and average surface roughness. When using two

sample points, the surface quality deteriorated while the quality improved and became saturated when the number of sample points exceeded six. An increase in the minimum length increased the MRR. As the minimum length increased from 10% to 50% of the width, the MRR increased by 45%, while surface quality remained unchanged. However, when the minimum length was 70% of the width, the normalized depth deviation and surface roughness increased. The scoring filter width hardly affected the machining characteristics.

The performance of LIBWE with a phosphoric acid-added absorbent for certain applications was observed by fabricating structures which were previously used for actual applications. Capillary-driven flow was achieved by fabricating a high-aspect-ratio glass microchannel. Reverse UV contact imprints could be produced by using a UV curing system on a glass mold with UV curing resin. A complex standalone glass microcomponent was also fabricated.

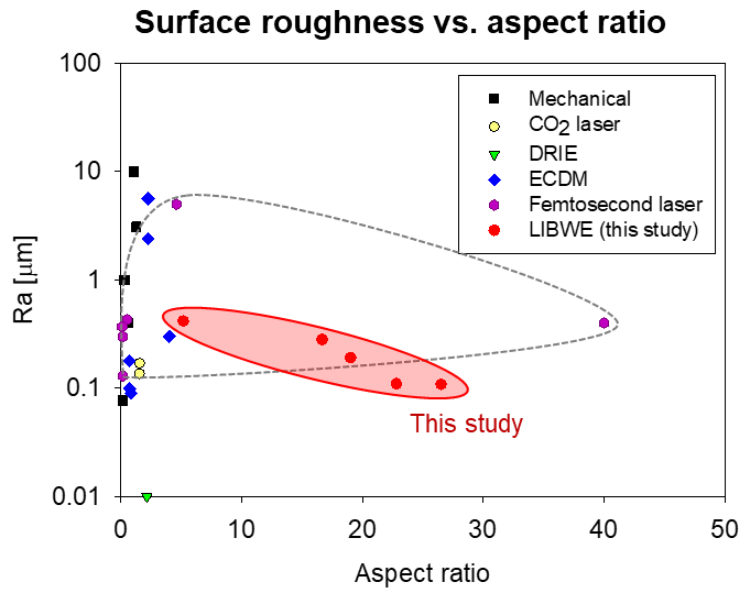
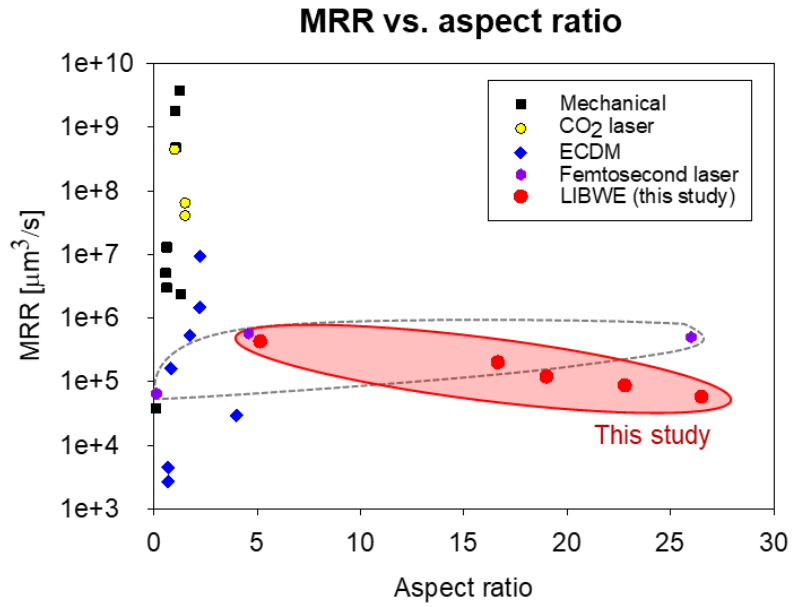


**Fig. 7.1 MRR and surface roughness versus aspect ratio for different glass processing technologies**

# Reference

- [1] Bahadorimehr AR, Jumril Y, Majlis BY, Low cost fabrication of microfluidic microchannels for Lab-On-a-Chip applications, 2010 International Conference on Electronic Devices, Systems and Applications, ICEDSA 2010 - Proceedings, 242–4. (2010)
- [2] Fu LM, Ju WJ, Yang RJ, Wang YN, Rapid prototyping of glass-based microfluidic chips utilizing two-pass defocused CO<sub>2</sub> laser beam method, *Microfluidics and Nanofluidics*, 14, 479–87. (2013)
- [3] Bhagat AAS, Hou HW, Li LD, Lim CT, Han J, Pinched flow coupled shear-modulated inertial microfluidics for high-throughput rare blood cell separation, *Lab on a Chip*, 11, 1870–8. (2011)
- [4] Aoyagi S, Izumi H, Isono Y, Fukuda M, Ogawa H, Laser fabrication of high aspect ratio thin holes on biodegradable polymer and its application to a microneedle, *Sensors and Actuators, A: Physical*, 139, 293–302. (2007)
- [5] Surdo S, Carpignano F, Strambini LM, Merlo S, Barillaro G, Capillarity-driven (self-powered) one-dimensional photonic crystals for refractometry and (bio)sensing applications, *RSC Advances*, 4, 51935–41. (2014)
- [6] Morgan CJ, Vallance RR, Marsh ER, Micro machining glass with poly crystalline diamond tools shaped by micro electro discharge machining, *Journal of Micromechanics and Microengineering*, 14, 1687–92. (2004)
- [7] Cheng J, Gong YD, Experimental study on ductile-regime micro-grinding character of soda-lime glass with diamond tool, *International Journal of Advanced Manufacturing Technology*, 69, 147–60. (2013)
- [8] Chen ST, Jiang ZH, A force controlled grinding-milling technique for quartz-glass micromachining, *Journal of Materials Processing Technology*, 216, 206–15. (2015)
- [9] Nagarah JM, Wagenaar DA, Ultradeep fused silica glass etching with an HF-resistant photosensitive resist for optical imaging applications,

- Journal of Micromechanics and Microengineering, 22, (2012)
- [10] Karásek P, Grym J, Roth M, Planeta J, Foret F, Etching of glass microchips with supercritical water, *Lab on a Chip*, 15, 311–8. (2015)
  - [11] Yen MH, Cheng JY, Wei CW, Chuang YC, Young TH, Rapid cell-patterning and microfluidic chip fabrication by crack-free CO<sub>2</sub> laser ablation on glass, *Journal of Micromechanics and Microengineering*, 16, 1143–53. (2006)
  - [12] Chung CK, Lin SL, Wang HY, Tan TK, Tu KZ, Lung HF, Fabrication and simulation of glass micromachining using CO<sub>2</sub> laser processing with PDMS protection, *Applied Physics A: Materials Science and Processing*, 113, 501–7. (2013)
  - [13] Cao XD, Kim BH, Chu CN, Micro-structuring of glass with features less than 100 µm by electrochemical discharge machining, *Precision Engineering*, 33, 459–65. (2009)
  - [14] Takahashi M, Murakoshi Y, Maeda R, Hasegawa K, Large area micro hot embossing of Pyrex glass with GC mold machined by dicing, *Microsystem Technologies*, 13, 379–84. (2007)
  - [15] Vitek DN, Adams DE, Johnson A, Tsai PS, Backus S, Durfee CG, et al., Temporally focused femtosecond laser pulses for low numerical aperture micromachining through optically transparent materials, *Optics Express*, 18, 18086. (2010)
  - [16] Sugioka K, Cheng Y, Midorikawa K, Three-dimensional micromachining of glass using femtosecond laser for lab-on-a-chip device manufacture, *Applied Physics A: Materials Science and Processing*, 81, 1–10. (2005)
  - [17] 17\_Three-dimensional femtosecond laser micromachining of photosensitive glass for biomicrochips.pdf, (n.d.)
  - [18] Ahamed MJ, Senkal D, Trusov AA, Shkel AM, Study of High Aspect Ratio NLD Plasma Etching and Postprocessing of Fused Silica and Borosilicate Glass, *Journal of Microelectromechanical Systems*, 24, 790–800. (2015)
  - [19] Tsvetkov MY, Minaev N V, Akovantseva AA, Timashev PS, Muslimov AE, Kanevskii VM, Thermoplasmonic laser-induced backside wet etching of sapphire, *Quantum Electronics*, 49, 133–40.

(2019)

- [20] Huang ZQ, Hong MH, Do TBM, Lin QY, Laser etching of glass substrates by 1064 nm laser irradiation, *Applied Physics A: Materials Science and Processing*, 93, 159–63. (2008)
- [21] Zimmer K, Böhme R, Precise etching of fused silica for micro-optical applications, *Applied Surface Science*, 243, 415–20. (2005)
- [22] Sato T, Kurosaki R, Narazaki A, Kawaguchi Y, Niino H, Flexible 3D deep microstructures of silica glass by laser-induced backside wet etching, *Applied Physics A: Materials Science and Processing*, 101, 319–23. (2010)
- [23] Lee DK, Choi SY, Park MS, Cho YH, Wetting properties of hybrid structure with hydrophilic ridges and hydrophobic channels, *Applied Physics A: Materials Science and Processing*, 124, 1–7. (2018)
- [24] Zhigalina OM, Khmelenin DN, Atanova A V., Minaev N V., Sviridov AP, Tsvetkov MY, A Nanoscale Modification of Materials at Thermoplasmonic Laser-Induced Backside Wet Etching of Sapphire, *Plasmonics*, 15, 599–608. (2020)
- [25] Seo JM, Kwon K-K, Song KY, Chu CN, Ahn S-H, Deposition of durable micro copper patterns into glass by combining laser-induced backside wet etching and laser-induced chemical liquid phase deposition methods, *Materials*, 13, (2020)
- [26] Kwon KK, Kim H, Kim T, Chu CN, High aspect ratio channel fabrication with near-infrared laser-induced backside wet etching, *Journal of Materials Processing Technology*, 278, 116505. (2020)
- [27] Vass C, Hopp B, Smausz T, Ignácz F, Experiments and numerical calculations for the interpretation of the backside wet etching of fused silica, *Thin Solid Films*, 453–454, 121–6. (2004)
- [28] Kawaguchi Y, Ding X, Narazaki A, Sato T, Niino H, Transient pressure induced by laser ablation of toluene, a highly laser-absorbing liquid, *Applied Physics A: Materials Science and Processing*, 80, 275–81. (2005)
- [29] Tagawa H, Thermal decomposition temperatures of metal sulfates, *Thermochimica Acta*, 80, 23–33. (1984)

- [30] Adáñez-Rubio I, Gayán P, Abad A, García-Labiano F, De Diego LF, Adáñez J, CO<sub>2</sub> capture in coal combustion by chemical-looping with oxygen uncoupling (CLOU) with a Cu-based oxygen-carrier, Proc 5th Int Conf on Clean Coal Technologies (CCT2011), (2011)
- [31] Xie X, Huang X, Jiang W, Wei X, Hu W, Ren Q, Three dimensional material removal model of laser-induced backside wet etching of sapphire substrate with CuSO<sub>4</sub> solutions, Optics and Laser Technology, 89, 59–68. (2017)
- [32] WALTERS H V., ChemInform Abstract: CORROSION OF A BOROSILICATE GLASS BY ORTHOPHOSPHORIC ACID, Chemischer Informationsdienst, 14, 572–4. (2016)
- [33] Pan C, Chen K, Liu B, Ren L, Wang J, Hu Q, et al., Fabrication of micro-texture channel on glass by laser-induced plasma-assisted ablation and chemical corrosion for microfluidic devices, Journal of Materials Processing Technology, 240, 314–23. (2017)
- [34] Kim BS, Park MS, Fabrication of Glass Microstructure Using Laser-Induced Backside Wet Etching, Transactions of the Korean Society of Mechanical Engineers A, 38, 967–72. (2014)
- [35] Xie XZ, Hu MF, Chen WF, Wei X, Hu W, Gao XY, et al., Cavitation bubble dynamics during laser wet etching of transparent sapphire substrates by 1064 nm laser irradiation, Journal of Laser Micro Nanoengineering, 8, 259–65. (2013)
- [36] Schwaller P, Zehnder S, Von Arx U, Neuenschwander B, A novel model for the mechanism of laser-induced back side wet etching in aqueous Cu solutions using ns pulses at 1064 nm, Physics Procedia, 12, 188–94. (2011)
- [37] Siow KS, Britcher L, Kumar S, Griesser HJ, XPS study of sulfur and phosphorus compounds with different oxidation states, Sains Malaysiana, 47, 1913–22. (2018)
- [38] Ghany KA, Newishy M, Cutting of 1.2 mm thick austenitic stainless steel sheet using pulsed and CW Nd:YAG laser, Journal of Materials Processing Technology, 168, 438–47. (2005)
- [39] Wang J, Niino H, Yabe A, One-step microfabrication of fused silica by laser ablation of an organic solution, Applied Physics A: Materials



Science and Processing, 68, 111–3. (1999)

- [40] Goswami A, Phani A, Umarji AM, Madras G, Polymer microfabrication by scanning based microstereolithography: Optical design and material functionality, Review of Scientific Instruments, 83, (2012)
- [41] Long J, Zhou C, Cao Z, Xie X, Hu W, Incubation effect during laser-induced backside wet etching of sapphire using high-repetition-rate near-infrared nanosecond lasers, Optics and Laser Technology, 109, 61–70. (2019)
- [42] Kwon K-K, Song KY, Seo JM, Chu CN, Ahn S-H, Precise glass microstructuring with laser induced backside wet etching using error-compensating scan path, Journal of Materials Processing Technology, 291, 117046. (2021)
- [43] Haisma J, Mold-assisted nanolithography: A process for reliable pattern replication, Journal of Vacuum Science & Technology B: Microelectronics and Nanometer Structures, 14, 4124. (1996)
- [44] Resnick DJ, Sreenivasan SV, Willson CG, Step & flash imprint lithography, Materials Today, 8, 34–42. (2005)

# 국문 초록

서울대학교

공과대학원

기계항공공학부

권귀감

본 논문에서는 인산이 첨가된 흡광용액을 사용한 레이저 후면 식각공정과 이를 활용한 다양한 형상의 유리 미세형상 가공 대해 연구하였다. 유리는 광학적으로 투명한 특성을 가지면서 다른 투명한 재료에는 없는 고강도, 내식성, 비전도성, 생물친화성 등의 특성을 가지고 있어 다양한 분야에서 활용되고 있으며, 미래에도 그 활용성이 높은 재료이다. 하지만 이러한 재료적 안정성이 가공 측면에서 유리를 난삭재로 만들어 다양한 미세 형상의 제작을 어렵게 하였다.

다양한 공정 연구를 통해 유리의 미세 가공 및 그 활용범위를 넓히는 시도가 진행 중이다. 전통적인 가공방식인 절삭가공부터 화학적 식각, 이산화탄소 레이저 미세가공 등 산업 친화적인 가공기술들을 통해 유리의 활용도를 높이고자 하는 다양한 시도들이 진행 중이지만 공정 자체의 한계로 인해 목표로 하는 형상이 제한되는 문제가 있다. 이러한 문제를 해결하기 위해 다양한 공정들이 새로이 개발되고 활용되고 있으며, 대표적으로 펨토초 펄스 레이저 가공, 전해방전가공, 건식 식각 등이 있다. 이러한 공정들의 높은 공정 자유도를 통해 다양한 유리 미세형상 제작이 가능하며, 다방면으로 공정의 최적화 및 활용방안이 연구되고 있다. 이렇게 다양한 공정을 통해 유리의 가공연구가 진행되고 있으나 산업적으로 적용 가능한 기술을 활용하면서도 목표로 하는 복잡한 형상이 가공 가능한 기술에 대해서는 연구가 부족한 상황이다.

본 논문에서는 산업적으로 다양하게 활용되고 있는 근적외선 레이저를 활용한 레이저 후면 식각공정을 통해 가공 가능한 유리의 형상을 확장하고, 그 원리를 탐구하였다. 일반적인 근적외선 레이저를 활용한 레이저 후면 식각 공정의 경우 흡광용액으로 활용하

는 황산구리 용액이 열분해에 의해 산화구리가 되고, 이러한 산화 구리의 과도한 증착으로 인해 파단이 발생하는 것을 밝혀져 있다. 본 논문에서 인산을 첨가하였을 때 산화구리의 증착이 방해되어 파단의 발생이 억제되는 것을 확인하였으며, 유리의 파단을 억제함으로써 레이저의 자유도를 활용한 다양한 형상의 가공이 가능하였다. 또한 임의의 점과 선 경로의 최적화 방안을 도입하여 일차원적인 채널 형상뿐만 아니라 기존의 레이저 후면 식각 공정이나 산업 친화적인 장비로 제작이 어려웠던 다양한 유리 미세 구조물의 가공을 진행하였고, 실제 연구나 산업에서 활용될 수 있는 형상을 가공하였다.

**주요어:** 레이저 후면 식각공정; 유리 미세가공; 레이저빔 가공; 레이저 조사 경로 최적화;

**학번:** 2015-20710